UNIVERSITY OF CALGARY

# The Differentiation Mapping of Oil Gravity Using Amplitude Variation with Offset, Hebron Ben Nevis Field, Offshore Newfoundland, Canada

By

Andrew John Royle

A THESIS

SUBMITTED TO THE FACULTY OF GRADUATE STUDIES

IN PARTIAL FULFILMENT OF THE REQUIREMENTS FOR THE

DEGREE OF MASTER OF SCIENCE

DEPARTMENT OF GEOLOGY AND GEOPHYSICS

CALGARY, ALBERTA

APRIL 2004

UNIVERSITY OF CALGARY

FACULTY OF GRADUATE STUDIES

The undersigned certify that they have read, and recommend to the Faculty of Graduate Studies for acceptance, a thesis entitled "The Differentiation Mapping of Oil Gravity Using Amplitude Variation with Offset, Hebron Ben Nevis Field, Offshore Newfoundland, Canada" submitted by Andrew John Royle in partial fulfillment of the requirements for the degree of Master of Science.

______________________________

Supervisor, Dr. Laurence R. Lines, Department of Geology and Geophysics

______________________________

Dr. John Bancroft, Department of Geology and Geophysics

______________________________

Dr. Mehran Pooladi-Darvish, Department of Chemical & Petroleum Engineering

______________________________

*Date*

## Abstract

This paper investigates the amplitude variation with offset (AVO) behaviour at the Ben Nevis reservoir zone in an attempt to predict API oil gravity variations. Intercept, gradient, fluid factor, and density reflectivity attribute volumes were extracted to observe the AVO effects at the reservoir zone. These attributes isolated the oil zones associated with the Ben Nevis reservoir and showed differences between the adjacent fault block reservoir zones. Detailed crossplotting at the oil bearing well locations isolated anomalous zones associated with the response at the top of the reservoir. Simultaneous inversion methods were applied to the dataset, which provided useful information on the nature of the lithology and pore fluids. The AVO and inversion attributes were then used as inputs in a neural network analysis for porosity and fluid density. The porosity volume correlated closely with the well data across the asset and the fluid density volume accurately portrayed the variations in oil density across the asset.

## Acknowledgements

My special thanks to Dr. Larry Lines and John Logel for their excellent guidance and support throughout my research. I would like to thank ExxonMobil, Petro-Canada, ChevronTexaco, and NorskHydro for their work on this field and the release of data to the public domain. I would like to acknowledge Brian Grant, John Evans, Craig Coulombe, Paul Gremell, Larry Sydora, Suzanne Verheyde, Mark MacLeod and Mike Donovan of ChevronTexaco Canada and Gerald Sullivan and Ed Stacey of Petro-Canada. John Pendrel of Fugro-Jason Geosystems for his assistance. I would like to thank Hampson-Russell for the use of their software, especially Brian Russell and Arthur Lee. I also would like to thank the CREWES sponsors and GEO-X Systems Ltd. for their support of this research.

## Dedication

To Becky

**Table of Contents**

## List of Tables

## List of Figures

## Glossary of Terms

**Acoustic impedance:** A rock property that is defined as the product of rock density and P-wave velocity.

**API gravity:** A standard adopted by the American Petroleum Institute for expressing the specific weight of oils. (API gravity = 141.5/specific gravity at 60ºF – 131.5).

**Amplitude variation with offset (AVO):** The variation in the amplitude of a seismic reflection with offset. Depends on velocity, density, and Poisson's ratio contrasts. Used as a hydrocarbon indicator for gas because a large change in Poisson's ratio tends to produce an increase in amplitude with offset (Sheriff, 1991).

**Bulk Modulus:** The stress-strain ratio under simple hydrostatic pressure (Sheriff, 1991).

**Fluid factor:** A numerical quantity that is designed to be low amplitude for all reflectors in a clastic sedimentary sequence except for rocks that lie off the "mudrock line". In the absence of carbonates and igneous rocks, high amplitude reflections on fluid factor traces would be expected to represent hydrocarbon-saturated sandstones.

**Gradient:** Rate of change of the amplitudes at each time sample as a function of incidence angle on a CDP gather. This value should contain entire AVO effect.

**Gas-oil-ratio (GOR):** This is the volume ratio of liberated gas to remaining oil at atmospheric pressure and 15.6°C (Batzle and Wang, 1992).

**Incompressibility:** The "incompressibility" modulus is related to the rocks ability to resist compression. This gives information about the pore fluid and lithology of a rock.

**Intercept:** Represents the theoretical zero-offset response. This response will show "bright spots" but does not show any AVO effect. This is also known as normal incidence reflectivity.

**Mudrock line:** The line fit on a crossplot of *P*-wave velocity against *S*-wave velocity on which water saturated sandstone, shale, and siltstones lie. Some of the rock types that lie off the "mudrock line" are gas-saturated sandstones, carbonates, and igneous rocks (Castagna et al., 1985).

**P-wave:** An elastic body (pressure) wave in which particle motion is in the direction of propagation.

**Poisson's ratio:** The ratio of the fractional transverse contraction to the fractional longitudinal extension when a rod is stretched (Sheriff, 1991). The Poisson's ratio for rocks ranges from near 0 for gas sands to 5.0 for shales.

**Ray tracing:** Determining the arrival time at detector locations by following raypaths, which obey Snell's law through a model for which the velocity distribution is known (Sheriff, 1991).

**Reflection coefficient:** is the ratio of the amplitude of displacement of a reflected wave to that of the incident wave (Sheriff, 1991).

**S-wave:** An elastic body (shear) wave in which particle motion is perpendicular to the direction of propagation.

## List of Symbols and Notations

| | |
|---|---|
| ***AVA*** | Amplitude variation with angle. |
| ***AVO*** | Amplitude variation with offset. |
| ***CMP*** | Common midpoint gather. |
| ***DHI*** | Direct hydrocarbon indicator. |
| ***GOR*** | Gas-oil-ratio. |
| $kg/m^3$ | A unit of density. |
| ***s*** | A time unit of seconds. |
| ***ms*** | A time unit of milliseconds. |
| $ms*kg/m^3$ | A unit of impedance. |
| $A$, $R_o$ | Intercept. |
| ***B, G*** | Gradient. |
| $R_P$ | P-wave reflectivity. |
| $R_S$ | S-wave reflectivity |
| $V_P$ | P-wave velocity. |
| $V_S$ | S-wave velocity. |
| $V_P/V_S$ | Ratio of P-wave velocity to S-wave velocity. |
| ***NI*** | Normal Incidence reflectivity |
| ***PR*** | Poisson reflectivity |
| $p$ | Raypath parameter. |
| $k$ | Bulk modulus. |
| $\lambda$ | Incompressibility. |
| $\mu$ | Rigidity. |
| $\phi$ | Porosity. |
| $\rho$ | Density. |
| $\rho_b$ | Bulk density. |
| $\rho_f$ | Fluid density. |
| $\rho_m$ | Matrix density. |
| $\sigma$ | Poisson's ratio. |
| $\theta$ | Angle of incidence. |

## 1.0 INTRODUCTION

In exploration seismology, the seismic reflection method is used to find structures that have potential to trap hydrocarbons. The risk lies in the possibility that the trap may contain no hydrocarbons. Exploration seismology would be more effective if the hydrocarbons could be distinguished directly on seismic sections. In the 1960's, geophysicists discovered that the presence of gas is sometimes associated with the presence of high amplitude reflections known as "*bright spots*" (Allen and Peddy, 1993). Most seismic interpreters make use of the fact that high-intensity seismic reflectors (*bright spots*) may be direct hydrocarbon indicators (*DHI*), which typically indicates the presence of gas. The use of bright spots for exploration greatly increased the success rate for wildcat gas wells; however, the bright spot method has limitations in that lithologic conditions other than gas can cause bright reflections. Dry holes drilled on bright spots have found wet sands, lignites, carbonate or hard streaks, and igneous intrusions (Allen and Peddy, 1993). A test more definitive than bright spots on a stacked section is sought for the direct detection of gas on seismic records. Ostrander (1982) demonstrated that gas sand reflection coefficients differ in an anomalous manner with increasing offset and explained how to make use of this anomalous behaviour as a direct hydrocarbon indicator on actual seismic data (Castagna and Backus, 1993). In this paper I will discuss this method, which is called the analysis of amplitude variation with offset (AVO).

### *1.1 AVO Rock Property Associations*

Seismic reflection data recorded in exploration are directly associated with the subsurface rock properties. The Lamé parameters $\lambda$, $\mu$, and $\rho$, which represent "incompressibility", rigidity, and density respectively, can allow for enhanced identification of reservoir zones. This is due in part to the fact that the compressibility (and hence the incompressibility) of a rock unit is very sensitive to pore fluid content, and also to the fact that lithologic variations tend to be better characterized by fundamental changes in rigidity, "incompressibility", and density as opposed to changes in $V_P$ and $V_S$. Figure 1-1a shows a rock matrix that is unstressed; here the rock will have the maximum amount of pore space between its grains. When compression (hydrostatic stress) is applied to a rock (figure 1-1b), the compression squeezes the grains causing a decrease in the pore space. If fluids such as oil or water are introduced to the pore space, they will resist the compression by increasing the pressure against the grains and produce a more incompressible rock. The introduction of gas into the pore space will give low incompressibility. This is because gas cannot resist the compression as effectively as the oil or water. Carbonates and igneous rocks have a harder framework and therefore they will have high incompressibility values regardless of pore fluid content. Figure 1-1c shows a sheared rock matrix, where shearing (shear stress) attempts to slide grains across each other. The pore space volume remains essentially unchanged during the process of shearing regardless of pore fluid type; therefore rigidity, which measures a rock resistance to shearing, should characterize lithology as opposed to pore fluid. Shales are

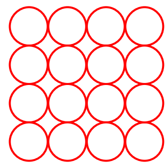

Figure 1-1a: Unstressed rock matrix.

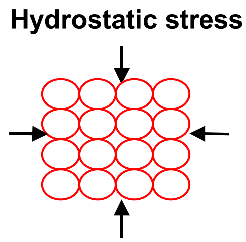


Figure 1-1b: Compressed rock matrix.

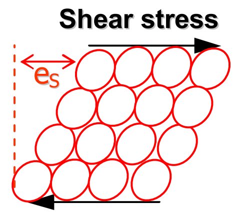


Figure 1-1c: Sheared rock matrix.

more susceptible to shearing than sands, because of the nature of their grain orientation; thus they tend to exhibit low rigidity values. Carbonates, due to their more rigid framework, resist shearing and therefore have high rigidity values. These elastic modulii are related to the seismic wave velocities by the following equations:

$$V_P^{\,2} = \frac{(k + (4/3)\mu)}{\rho} = \frac{(\lambda + 2\mu)}{\rho} \qquad 1.1$$

$$V_S^{\,2} = \frac{\mu}{\rho} \qquad 1.2$$

### *1.2 AVO as a Gas Indicator*

This investigation of the relative amplitudes of events within a CMP gather is known as amplitude variation with offset analysis. AVO is also referred to as amplitude versus offset. Alternatively, these relative amplitudes can also be examined with the variation in angle. Amplitude variation with angle (AVA) is the examination of traces sampling the same midpoint location at increasing angles of incidence. The reflectors associated with some reservoirs containing gas-bearing rocks increase in amplitude with offset relative to other reflectors. However, such an increase in amplitude is “rare” and the majority of reflections observed on a CMP gather decrease in amplitude with offset. Therefore, AVO analysis is a search for an anomalous seismic response (Allen and Peddy, 1993).

In AVO analysis, we examine reflections at a range of source-receiver offsets. A common midpoint gather (CMP) is the data input for AVO analysis. CMP gathers are the norm for modern seismic acquisition therefore the input for AVO analysis imposes minimal or no additional effort in acquisition for most exploration. During seismic processing these traces are formed into a CMP gather, the input to AVO analysis.

#### *1.2.1 $V_P/V_S$ relationships*

The use of AVO as a direct hydrocarbon indicator in clastic rocks is based on differences in the response of the *P*-wave velocity ($V_P$) and the *S*-wave velocity ($V_S$) of a reservoir rock to the introduction of gas into pore spaces (Allen and Peddy, 1993). The theory of AVO for clastic rocks is quite simple. When a *P*-wave strikes a rock interface at a particular angle, a fraction of the incident *P*-wave energy is converted to shear wave energy. Most importantly, *P*-wave and S-wave's have quite different sensitivities to pore fluids. The introduction of a small amount of gas into the pore spaces of a clastic sedimentary rock can reduce the *P*-wave velocity of the rock drastically but the *S*-wave velocity is relatively unaffected. Since *S*-waves cannot travel through liquids or gases, the pore space constituent does not affect the velocity of *S*-waves, whose velocity depends directly on the rock framework (matrix). Actually, the S-wave velocity may increase with the introduction of gas into the pore space because the density of gas is lower than the density of brine. The change in the ratio of *P*-wave velocity to *S*-wave velocity (and consequently Poisson's Ratio) causes the partitioning of an incident wave to differ for the case of a gas-sand/shale or gas-sand/wet-sand reflector from that of most other reflectors. Figure 1-2 shows the theoretical values for *S*-wave velocities and *P*-wave velocities at various gas saturations for a porous medium.

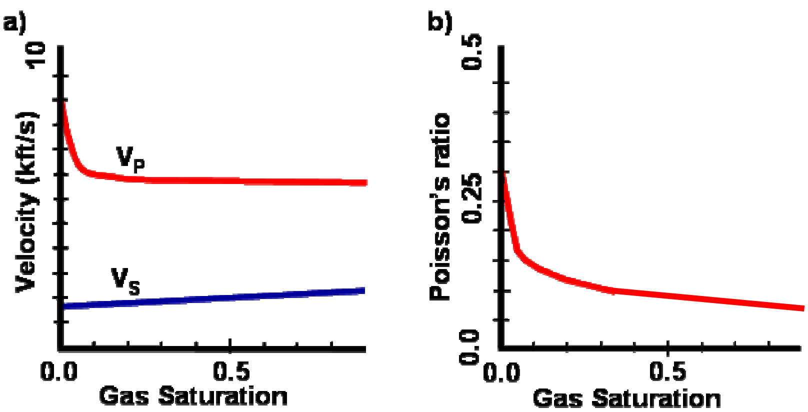


Figure 1-2. a) P-wave velocity of a porous solid rapidly decreases with the introduction of a small percentage of gas. The S-wave velocity increases linearly with gas saturation. b) The two effects show a decrease in the Poisson's ratio of the rock with increasing gas saturation (modified from Allen and Peddy, 1993).

The decrease in the $V_P/V_S$ ratio with the introduction of gas into the pore space of a rock changes the relative amplitudes of the reflections from the top and base of the reservoir as a function of the angle at which a wave strikes its boundaries (Allen and Peddy, 1993).

### *1.2.2 Poisson's ratio*

The ratio between $V_P$ and $V_S$ ($V_P/V_S$) can be expressed in terms of Poisson's ratio, $\sigma$, an important elastic constant. Poisson's ratio for an isotropic elastic material is simply related to the *P*-wave ($V_P$) and *S*-wave ($V_S$) velocities of the material by:

$$\sigma = \frac{(V_P / V_S)^2 - 2}{2\left[(V_P / V_S)^2 - 1\right]} \qquad 1.3$$

Poisson's ratio can be established using field or laboratory measurements of $V_P$ and $V_S$.

Poisson's ratio also has a physical definition. If one takes a cylindrical rod of an isotropic elastic material and applies a small axial compressional force to the ends, the rod will change shape. The length of the rod will decrease slightly (Ostrander, 1982). By definition, Poisson's ratio is the ratio of the relative change in radius (fractional transverse contraction) to the relative change in length (longitudinal extension) when a rod is stretched (Sheriff, 1994). Most isotropic materials have Poisson's ratio between 0.0 and 0.5. Materials such as fluids, which are incompressible, have a Poisson's ratio of 0.5, while material that are more compressible in nature (such as gas sands) have ratios which are closer to zero.

### *1.2.3 Clastic vs. carbonate reservoirs*

AVO has been widely used in clastic reservoirs as a direct hydrocarbon indicator. Carbonate reservoirs on the other hand are different due to their rigid framework. AVO has been used in carbonate reservoirs in an attempt to detect porosity. Chacko (1989) used AVO successfully in an attempt to detect porosity by comparing AVO synthetic seismograms to the corresponding CMP gathers of the seismic data.

Porosity has a major effect on the acoustic impedance of a limestone; seismic reflection coefficients from the top of limestone beds are sometimes lower where porosity exists (dimming). Depending on the magnitude of this effect and on the data quality, seismic amplitudes may indicate porous zones in limestones. These amplitude effects can be detected on stacked seismic data but cannot identify porosity from facies changes. Offset dependent effects, which are a function of additional physical properties of rocks, could possibly distinguish between tight limestone facies and porous limestone facies.

In carbonate reservoirs AVO has not been proven to distinguish pore fluid but can possibly identify porous facies. The first step in applying AVO would be to use finite offset numerical modelling seismic modelling, and then compare these synthetic traces to the actual seismic data for evaluation. The amplitude behavior of the synthetic traces is found to be quite sensitive to the $V_P/V_S$ specified used in the reservoir zone of the earth model. Chacko (1989) showed that gas-charged porous limestone facies might have lower $V_P/V_S$ values than the wet porous limestone facies. Therefore this is still not an intuitive process and the accuracy may depend on good well control and measured shear wave information in the area.

## 2.0 OFFSET DEPENDENT REFLECTIVITY

### *2.1 Compressional wave propagation*

A plane *P*-wave striking an interface at normal incidence experiences no conversion to *S*-wave at the interface. At any angle other than normal incidence, some fraction of the incident *P*-wave is converted to an S-wave at the reflector and the reflection coefficients become a function of $V_P$, $V_S$ and density of each layer (figure 2-1). As seen in figure 2-1, reflection at the interface involves energy partition from an incident P-wave to 1) a reflected *P*-wave ($R_P$), 2) a reflected *S*-wave ($R_S$), 3) a transmitted *P*-wave ($T_P$), and 4) a transmitted *S*-wave ($T_S$). The angles for incident, reflected, and transmitted rays synchronous at the boundary are related by Snell's law.

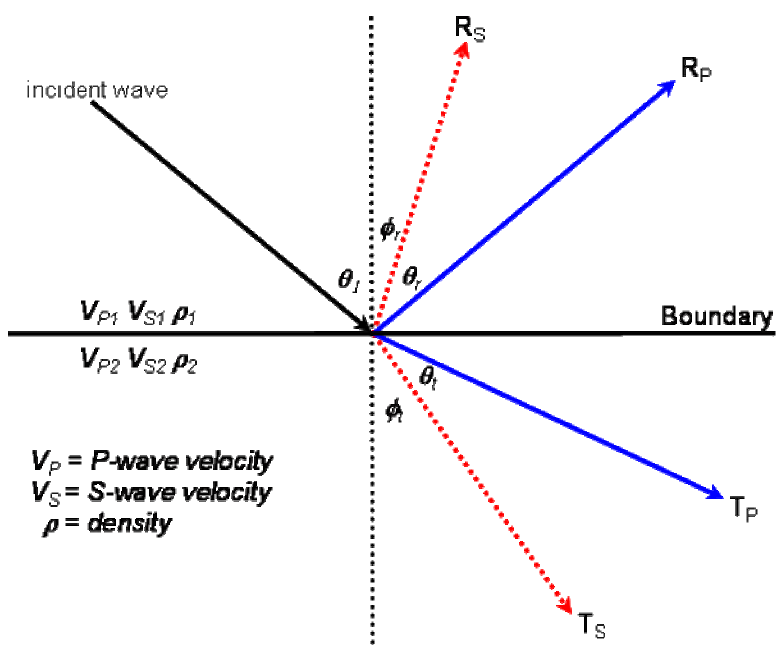


Figure 2-1: An incident *P*-wave is split into four components upon interacting with the boundary between two media.

### 2.2 Snell's Law

When a wave crosses a boundary between two isotropic media, the wave changes direction such that:

$$p = \frac{\sin\theta_i}{V_{P1}} = \frac{\sin\theta_t}{V_{P2}} = \frac{\sin\phi_r}{V_{S1}} = \frac{\sin\phi_t}{V_{S2}} \qquad 2.1$$

where $\theta_i$ is the angle of the incident wave with a velocity $V_i$=$V_{P1}$ if a *P*-wave or $V_i$=$V_{S1}$ *if a S-wave*: $\theta_r$ and $\phi_r$ are the angles of reflection of the *P*- and *S*-wave's in medium 1, which have velocities $V_{P1}$ and $V_{S1}$, respectively: $\theta_t$ and $\phi_t$ are the angles transmission of the *P*- and *S*-waves in medium 2, which have velocities $V_{P2}$ and $V_{S2}$, respectively; $p$ is the raypath parameter (Sheriff, 1991).

### 2.3 Reflection coefficients

The P-wave reflection coefficient as a function of incidence angle $R_{PP}(\theta_i)$ is defined as the ratio of the amplitude of the reflected *P*-wave to that of the incidence *P*-wave. Also, the *P*-wave transmission coefficient $T_{PP}(\theta_i)$ is the ratio of amplitude of the transmitted P-wave to that of the incident *P*-wave (Castagna and Backus, 1993). The partitioning of an incident wave at a reflecting interface can be expressed by any one of several sets of equations: as the ratio of incident to transmitted or to reflected displacement amplitudes, displacement potentials, or energy (Young and Braile, 1976). The reflection coefficient is the ratio of the amplitude of displacement of a reflected wave to that of the incident wave (Sheriff, 1991). From the acoustic impedance values we calculate the reflection coefficient between the boundaries of units.

For normal incidence on an interface that separates media of densities $\rho_1$ and $\rho_2$ and velocities $V_1$ and $V_2$, the reflection coefficient for a plane wave is:

$$R = \frac{(V_2\rho_2 - V_1\rho_1)}{(V_2\rho_2 + V_1\rho_1)} \qquad 2.2$$

The reflection coefficient gives the relative amplitudes of the reflected and incident waves. When the medium in which the incident wave travels has smaller acoustic impedance than the medium across from it, there is no phase change on reflection. When the incident wave is from the side of the interface having higher acoustic impedance, the reflected wave shows a phase shift of 180$^{o}$.

The P-wave transmission coefficient at normal incidence is given by the equation:

$$T_P = 1 - R_P \qquad 2.3$$

The variation of reflection and transmission coefficients with angle of incidence is referred to as offset-dependent reflectivity and is the fundamental basis for AVO analysis (Castagna and Backus, 1993).

### *2.4 Zoeppritz equations*

If we have an interface which separates two isotropic elastic mediums with values for $V_P$, $V_S$, and $\rho$. With a *P*-wave plane wave (in the plane of the page) impinging on the interface, the stress on these iso-elastic mediums can be worked out. There are boundary conditions that must be taken into account. Firstly, *continuity of displacement* ($u_{z1}=u_{z2}$, $u_{x1}=u_{x2}$) which states that there is no slipping along the interface or no ripping apart of the rocks at the interface. Secondly, *continuity of stress* ($\sigma_{xz1}=\sigma_{xz2}$, $\sigma_{zz1}=\sigma_{zz2}$), which states that any stress at the interface would result in infinite acceleration of the mass-less surface. From this a series of equations with 4 unknowns can be derived in terms of $R_P$, $T_P$, $R_S$, and $T_S$ known as the Zoeppritz equations.

The Zoeppritz equations give the reflection and transmission coefficients for plane waves as a function of angle of incidence and six independent elastic parameters, three on each side of the reflecting interface (Shuey, 1984). These equations are quite complex and are not straightforward to fit to actual seismic data. Since the solutions of the Zoeppritz equations are complex, an intuitive grasp of the result for different cases is difficult.

### *2.5 Zoeppritz assumptions*

The Zoeppritz equations are useful for extracting physical properties from seismic data but the assumptions must be understood for best application. As mentioned there must be continuity of stress and continuity of displacement. Seismic waves travel through the earth in a spherical nature. The Zoeppritz equations however describe the reflection coefficients for plane waves. The wavefield is also assumed to contain only primary wave energy. Amplitudes are measured of reflection coefficients only in the absence of extraneous effects such as transmission losses, attenuation divergence, geophone directivity, and a host of other factors (Allen and Peddy, 1993). The Zoeppritz equations describe an isotropic medium and do not take anisotropy or absorption into account. The solution of the Zoeppritz equations cannot be taken as the exact expected seismic response measured in an actual seismic survey (Allen and Peddy, 1993).

## 3.0 AVO METHODOLOGY

### *3.1 Zoeppritz Approximations*

Approximations to the Zoeppritz equations have been developed by many researchers. Aki and Richards (1980), Shuey (1985), Hilterman (1990), Smith and Gidlow (1987), and Fatti et al. (1994) have simplified the relationship between reflection coefficient and angle of incidence so that the major factors could be identified. I will briefly discuss the approximations of Aki and Richards, Shuey, Hilterman, Smith and Gidlow, and Fatti et al.: these approximations allow AVO analysis to be applied without difficulty. These approximated Zoeppritz equations can be fitted to the amplitudes of all the traces at each time sample of the gather and certain rock properties can be estimated.

#### *3.1.1 Aki-Richards approximation*

Aki and Richards (1980) give the Zoeppritz equations in an easily solved matrix form:

$$Q = P^{-1}R \qquad 3.1$$

This is discussed in more detail in *Appendix A*. Aki and Richards approximations to the Zoeppritz equations give simpler and more practical form of the Zoeppritz equations that can be readily applied to actual seismic data with more ease. The Aki and Richards (1980) linearized approximation of the Zoeppritz equations for the P-wave reflection coefficient is given by:

$$R(\theta) = \frac{1}{2}\left(1 - 4{V_S}^2 p^2\right)\frac{\Delta\rho}{\rho} + \frac{1}{2\cos^2\theta}\frac{\Delta V_P}{V_P} - 4{V_S}^2 p^2 \frac{\Delta V_S}{V_S} \qquad 3.2$$

where:

$R$ = offset dependent reflectivity

$\Delta V_P = (V_{P2} - V_{P1})$
$V_P$ = average *P*-wave velocity $(V_{P2} + V_{P1}) / 2$
$\Delta V_S = (V_{S2} - V_{S1})$
$V_S$ = average S-wave velocity $(V_{S2} + V_{S1}) / 2$
$\rho$ = average density $(\rho_2 + \rho_1) / 2$
$\Delta\rho = (\rho_2 - \rho_1)$
$p$ = ray path parameter

The Aki and Richards approximation has the following assumptions: the relative changes of property are sufficiently small (as discussed later on), second-order terms can be neglected, and the incident angle does not approach critical angle. The Aki-Richards approximation is sufficient for most acquired seismic data several approximations that are more geological and geometrical meaningful have been formed.

***3.1.2 Shuey's approximation***

Shuey's approximation of the Zoeppritz equations shows the relationship of reflection coefficient versus angle of incidence to changes in impedance and Poisson's ratio. Shuey (1985) approximates the Zoeppritz equations from Aki and Richards (1980) by eliminating the properties $V_S$ and $\Delta V_S$ in the favour of $\sigma$ and $\Delta\sigma$. Shuey's approximation is as follows:

$$R(\theta) = R_O + \left[ A_O R_O + \frac{\Delta\sigma}{(1-\sigma)^2} \right] \sin^2\theta + \frac{1}{2}\frac{\Delta V_P}{V_P}\left(\tan^2\theta - \sin^2\theta\right) \tag{3.3}$$

where $R_O$ is the normal incidence reflection coefficient, $A_O$ is the normal incidence amplitude, $\sigma$ is Poisson's ratio, $\Delta\sigma$ is the difference in Poisson's ratio *($\sigma_2$-$\sigma_1$)*, and $\theta$ is the average angle of incidence measured from the vertical *[($\theta_1$+$\theta_2$)/2]*. This approximation is commonly used in AVO as it contains three terms separating the normal incidence, small angle (to about 30 degrees), and large angle contributions to the total reflection coefficient at any given angle (Allen and Peddy, 1993). Shuey's approximation gives a relatively simple relationship between rock properties (Poisson's ratio) and the variation in reflection coefficients, and stresses the importance of Poisson's ratio as the primary determinant of the AVO response of a reflection. Shuey's approximation can be simplified even further by omitting the higher order contribution:

$$R(\theta) = R_0 + G\sin^2\theta \qquad 3.4$$

Where, $R_0$ is the normal incident P-wave reflectivity or "*intercept*" and $G$ is the "*gradient*" term. The *gradient* by definition is the rate of change of the amplitudes at each time sample as a function of incidence angle on a CDP gather. This value should contain entire AVO effect. The *intercept* represents the theoretical zero-offset response; this response will show "*bright spots*" but does not show any AVO effect. The *intercept* and *gradient* terms from this approximation can be easily obtained trough linear regression.

### *3.1.3 Hilterman's approximation*

Hilterman (1989) introduced an approximation of Shuey's (1984) equation:

$$R_0 = NI\left[1-4\left(\frac{V_S}{V_P}\right)^2\sin^2\theta\right]+\left[\frac{\Delta\sigma}{(1-\sigma)^2}\right]\sin^2\theta+\frac{1}{2}\frac{\Delta V_P}{V_P}\left[\tan^2\theta-4\left(\frac{V_S}{V_P}\right)^2\sin^2\theta\right] \qquad 3.5$$

Assuming $V_S/V_P = 0.5$ or $\sigma = 0.33$, equation (3.5) becomes:

$$R_0 = NI\left[1-\sin^2\theta\right]+\left[\frac{\Delta\sigma}{(1-\sigma)^2}\right]\sin^2\theta+\frac{1}{2}\frac{\Delta V_P}{V_P}\left[\tan^2\theta-\sin^2\theta\right] \qquad 3.6$$

Now, assuming that for $\theta < 30^o$ $tan^2\theta \cong sin^2\theta$, equation (3.6) changes to:

$$R_0 = NI\cos^2\theta + \left[\frac{\Delta\sigma}{(1-\sigma)^2}\right]\sin^2\theta \qquad 3.7$$

Hilterman refers to the *[$\Delta\sigma/(1-\sigma)^2$]* term as the Poisson reflectivity (*PR*) this is quite similar to the *gradient* term from the Shuey approximation. Furthermore, if the average Poisson's ratio is set to 0.33, equation (3.7) simplifies to:

$$R(\theta) = NI\cos^2\theta + 2.25\Delta\sigma\sin^2\theta \qquad 3.8$$

where:

$NI$ - normal incidence reflection coefficient
$\Delta\sigma$ - difference of Poisson's ratio between the lower and upper media
$\theta$ - angle of incidence

The *NI* term is the same as the normal incident *P*-wave reflectivity or "*intercept".* Now the interpreter must predict the lithologies from the rock properties, which are encoded in *NI* and $\Delta\sigma$ from the CMP gathers (Hilterman, 1990). The *normal incidence* and *Poisson reflectivity* terms from this approximation can be obtained through linear regression.

***3.1.4 Smith and Gidlow approximation***

The starting point for Smith and Gidlow's approach (1987) is a linearized approximate form of the Zoeppritz equation after Aki and Richards (1980). The Aki and Richards equation gives an approximate relationship between the P-wave reflection coefficient and the angle of incidence:

where:

$$R = \frac{1}{2}\left(\frac{\Delta V_P}{V_P} + \frac{\Delta\rho}{\rho}\right) - 2\left(\frac{V_S}{V_P}\right)^2\left(2\frac{\Delta V_S}{V_S} + \frac{\Delta\rho}{\rho}\right)\sin^2\theta + \frac{1}{2}\left(\frac{\Delta V_P}{V_P}\right)\tan^2\theta \qquad 3.9$$

$R$ = P-wave reflection coefficient
$V_P$ = average P-wave velocity
$V_S$ = average S-wave velocity

$\rho$ = average density
$\theta$ =average of $\theta_1$ and $\theta_2$

Equation (1) is accurate up to angles of incidence around 50 degrees for typical velocity and density contrasts. Smith and Gidlow assume $\Delta V_P / V_P$, $\Delta V_S / V_S$, and $\Delta\rho/\rho$ are sufficiently small that the second order terms may be ignored and $\theta$ does not approach critical angle or 90 degrees. They also used the Gardner equation ($\rho = kV^{1/4}$, where k is a constant) to remove the density reflectivity giving the equation:

$$R = \frac{\Delta V_P}{V_P}\left(\frac{5}{8}+\frac{1}{2}\tan^2\theta\right) - \left(\frac{V_S}{V_P}\right)^2\left(4\frac{\Delta V_s}{V_S}+\frac{1}{2}\frac{\Delta V_P}{V_P}\right)\sin^2\theta \qquad 3.10$$

Firstly, a relationship must be determined between offset distance ($x$) and angle of incidence ($\theta$), and a value for ($V_S/V_P$) must also be designated. Both the relationship and the ($V_S/V_P$) values can be estimated from the stacking velocities or borehole information. The interval velocity function is generally not known in detail and therefore is smooth. Velocity functions can be derived from stacking velocities or borehole information. A smooth P-wave velocity function against time for the area is obtained. The relationship between $x$ and $\theta$ can be determined by assuming the earth to be a stack of thin horizontal layers and performing iterative ray tracing. Ray tracing yields angle of incidence as a function of offset and zero offset two-way travel time (Smith and Gidlow, 1987).

Since absolute values of $V_S$ and $V_P$ are not expected from the seismic only reflectivities, it is necessary to make some assumption about the $V_S/V_P$ ratio. To determine ($V_S/V_P$), we use the empirically derived “mudrock line” relationship between $V_P$ and $V_S$ for water-saturated clastic rocks determined by Castagna et al., (1985):

$$V_P = 1369 + 1.6 V_S m/s \qquad 3.11$$

This relationship used with the P-wave velocity function, gives a value of $V_S/V_P$ for each time sample on the CMP gather. Equation (3.11) is a 'global' relationship and a more regional trend may be appropriate for specific areas if $V_S$ measured information is available. Such a relation may be derived from crossplots of borehole measurements or using dipole (shear) sonic log measurements. This 'global' trend is designed for clastic rocks and in the presence of carbonate rocks equation 3.11 will be inaccurate. In clastic regions containing interbedded sand, silt and shale, which characterize many hydrocarbon regions, the linear relationship in equation 3 will sufficiently predict $V_S$ and ultimately give $V_S/V_P$.

Least squares curve fitting is done to fit equation (3.10) to the P-wave reflection amplitudes from real data CMP gathers to estimate $\Delta V_P/V_P$ and $\Delta V_S/V_S$. The least squares curve fitting of equation (3.10) to reflection amplitudes on CMP gathers can be expressed as the weighted sum of the reflection amplitudes in a CMP gather. The weights are both offset- and time-variant and depend on the $V_P$ -model, the $V_S/V_P$ model, and the offset geometry of the CMP gather including the mute pattern. The NMO corrected traces in a CMP gather are multiplied by the weights and summed. The output of the weighted stacks will be traces representing $\Delta V_P/V_P$, or P-wave velocity reflectivity, and $\Delta V_S/V_S$, or S-wave velocity reflectivity, both with the normal time scale of the seismogram.

### *3.1.5 Fatti et al. approximation*

Fatti et al. use a method that they call the Geostack technique. They extend Smith and Gidlow (1987) method to include the density term. Their starting point is the linearized approximated form of the Zoeppritz equation from Aki and Richards (1980):

where:

$$R = \frac{1}{2}\left(\frac{\Delta V_P}{V_P} + \frac{\Delta\rho}{\rho}\right) - 2\left(\frac{V_S}{V_P}\right)^2\left(2\frac{\Delta V_S}{V_S} + \frac{\Delta\rho}{\rho}\right)\sin^2\theta + \frac{1}{2}\left(\frac{\Delta V_P}{V_P}\right)\tan^2\theta \qquad 3.12$$

$R$ = *P*-wave reflection coefficient
$V_P$ = average *P*-wave velocity
$V_S$ = average *S*-wave velocity
$\rho$ = average density
$\theta$ = average of $\theta_1$ and $\theta_2$

Equation (3.12) is typically accurate to angles of incidence around *35* degrees for typical velocity and density contrasts. Like Smith and Gidlow (1987), they assume $\Delta V_P / V_P$, $\Delta V_S / V_S$, and $\Delta\rho/\rho$ are sufficiently small that the second order terms may be ignored and $\theta$ does not approach critical angle or 90 degrees. They state that if Gardner's relationship does not hold, equation (3.12) can be written in terms of *P*-wave and *S*-wave acoustic impedances:

$$I_P = \rho V_P = P - wave\ \ acoustic\ \ impedance$$
$$I_S = \rho V_S = S - wave\ \ acoustic\ \ impedance$$
$$\frac{1}{2}\frac{\Delta I_P}{I_P} = \frac{1}{2}\left(\frac{\Delta V_P}{V_P} + \frac{\Delta\rho}{\rho}\right) = zero\ \ offset\ \ P - wave\ \ reflection\ \ coefficient$$
$$\frac{1}{2}\frac{\Delta I_S}{I_S} = \frac{1}{2}\left(\frac{\Delta V_S}{V_S} + \frac{\Delta\rho}{\rho}\right) = \ zero\ \ offset\ \ S - wave\ \ reflection\ \ coefficient$$

Equation (3.12) now becomes:

$$R=\frac{1}{2}\frac{\Delta I_P}{I_P}\left(1+\tan^2\theta\right)-4\left(\frac{V_S}{V_P}\right)^2\left(\frac{\Delta I_S}{I_S}\right)\sin^2\theta-\left[\frac{1}{2}\left(\frac{\Delta\rho}{\rho}\right)\tan^2\theta-2\left(\frac{V_S}{V_P}\right)^2\left(\frac{\Delta\rho}{\rho}\right)\sin^2\theta\right] \quad 3.13$$

The third term in (3.13) is small for angles of incidence less than 35 degrees and $V_S/V_P$ ratios between 0.1 and 2.0 (Poisson's Ratio between 0.1 and 0.33) (Fatti et al., 1994). Equation (3.13) now simplifies to:

$$R=\frac{1}{2}\frac{\Delta I_P}{I_P}\left(1+\tan^2\theta\right)-4\left(\frac{V_S}{V_P}\right)^2\left(\frac{\Delta I_S}{I_S}\right)\sin^2\theta \quad 3.14$$

Once a relationship between offset distance ($x$) and angle of incidence ($\theta$), and a value for ($V_S/V_P$) has been designated, ray tracing is performed. Then least squares curve fitting is done to fit equation (3.14) to the *P*-wave reflection amplitudes from real data CMP gathers to estimate $\Delta I_P/I_P$ and $\Delta I_S/I_S$. Now, the unknowns $\Delta I_P/I_P$ and $\Delta I_S/I_S$ can be solved at the boundary. The output of the weighted stacks will be traces representing $\Delta I_P/I_P$, or *P*-wave impedance reflectivity, and $\Delta I_S/I_S$, or *S*-wave impedance reflectivity, both with the normal time scale of the seismogram.

### *3.2 Zoeppritz approximation comparison*

A comparison of the Zoeppritz approximations to the exact Zoeppritz equations is carried out in order to test their accuracy. This will give a feeling of what angle ranges different approximations are accurate. The Ostrander (1984) gas sand model is used to make comparisons of the plane-wave reflection coefficients. The physical properties of this model are outlined on figure 3-1.

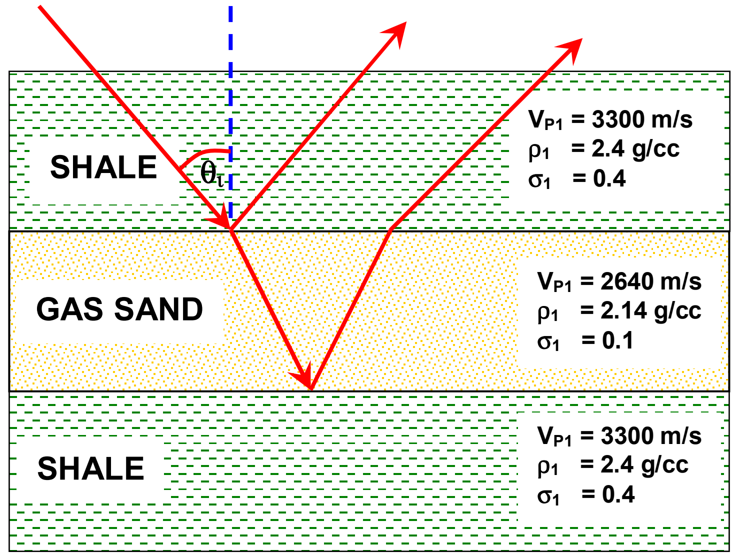


Figure 3-1: Ostrander's hypothetical three-layer gas sand model.

The reflection from the top of the gas sand is analyzed. Changes in the *P*-wave reflection coefficient as a function of incidence angle are shown in Figure 3-2. There is clearly an increase in the trough amplitude with offset, which we expected to see. The angle of incidence range is to 90 degrees. It can be seen that past 15 – 20 degrees the approximations tend to vary. The amplitude behaviour for the exact Zoeppritz equations is shown in black. The three-term Aki-Richards (purple line) and three-term Shuey (blue line) approximations seem to have the best fit. The three-term Aki-Richards, three-term Shuey, Smith and Gidlow, and Fatti approximations seem to trend the same as the exact Zoeppritz equations past 40 degrees. The Smith and Gidlow approximation fits well also but the near angles do not fit as well as the rest. Since recorded seismic data are not usually recorded past 45 degrees (critical angle) angle of incidence a zoomed range (Figure 3-3) is examined to get a closer comparison.

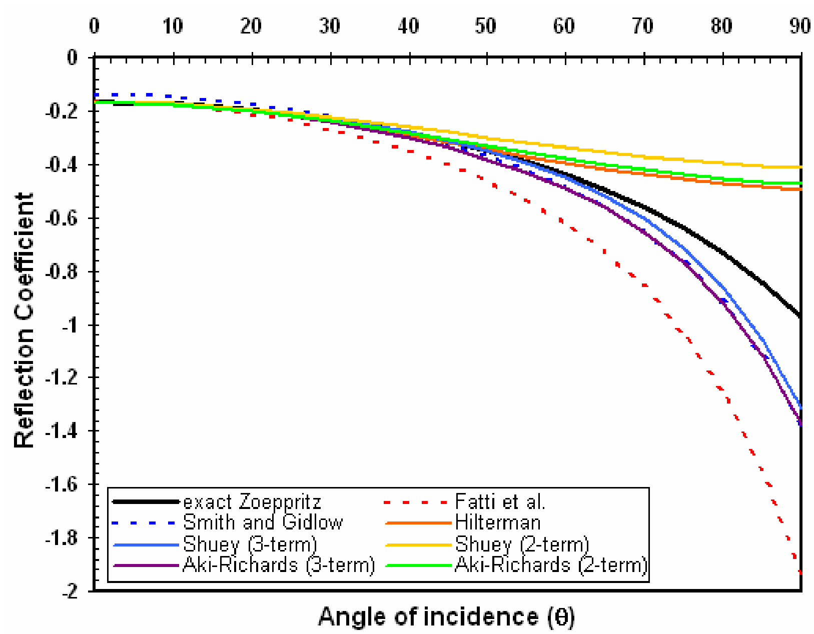


Figure 3-2: The exact and approximated reflection coefficients as a function of angle of incidence ($\theta_{max}$ = 90°).

Typically Shuey's approximation breaks down at about 30 degrees, for this model Shuey's approximation holds pretty well to about 55 degrees. The third term for Shuey's approximation contributes to about 65 degrees. Hilterman's and the two-term Aki-Richards approximations fit quite well to the exact Zoeppritz equations to about 50 degrees. The Smith and Gidlow approximation fits relatively well to about 50 degrees but at near angles the reflection coefficients is not approximated very well. This is probably because Smith and Gidlow use Gardner's relationship to estimate the density and the zero-offset reflection coefficient is not approximated accurately. The Fatti et al. approximation fits quite well to about 40 degrees.

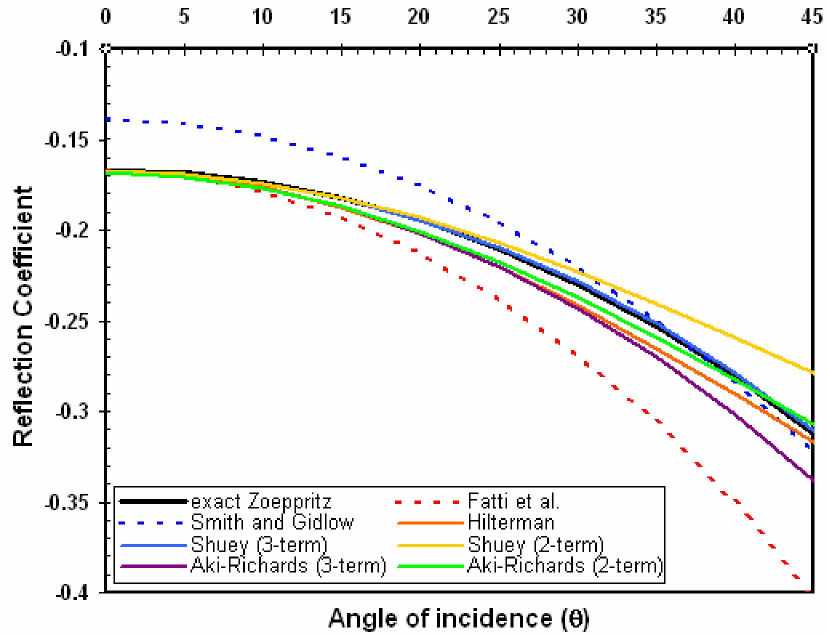


Figure 3-3: The exact and approximated reflection coefficients as a function of angle of incidence ($\theta_{max}$ = 45°).

### 3.3 Fluid Factor

The "*fluid factor*" concept introduced by Smith and Gidlow (1987) attempts to highlight gas-bearing sandstones. The Fluid Factor is a scalar quantity that is designed to be low amplitude for all reflectors in a clastic sedimentary sequence except for rocks that lie off the "mudrock line". In the absence of carbonates and igneous rocks, high amplitude reflections on fluid factor traces would be expected to represent gas-saturated sandstones. Water saturated sandstones, shales, and siltstones should fall approximately on the mudrock line. Gas saturated sandstones on the other hand have lower *P*-wave velocities and slightly higher *S*-wave velocities and therefore fall of the mudrock line. Taking the derivative of Castagna et al. (1985) mudrock relationship, gives:

$$\Delta V_P = 1.16 \Delta V_S \qquad 3.15$$

Multiplying equation (3.15) by *1/2$V_P$* and rearranging gives:

$$\left(\frac{\Delta V_P}{2V_P}\right) = 1.16\left(\frac{V_S}{V_P}\right)\left(\frac{\Delta V_S}{2V_S}\right) \qquad 3.16$$

$$i.e., R_P = 1.16\left(\frac{V_S}{V_P}\right)R_S \qquad 3.17$$

$R_P$ = zero-offset *P*-wave reflection coefficient
$R_S$ = zero-offset *S*-wave reflective coefficient

Then the "fluid factor", $\Delta F$, can be defined as:

$$\Delta F = R_P - 1.16\left(\frac{V_S}{V_P}\right)R_S \qquad 3.18$$

If the layers above and below the boundary that produce a reflection lie on the mudrock line, then $\Delta F = 0$. But if one of the layers lies on and the other off the mudrock line, then $\Delta F$ does not equal zero. Another approach to the "fluid factor" equation is that $\Delta F$ is the difference between the actual *P*-wave reflection coefficient $R_P$ and the calculated $R_P$ for the same sandstone in a water saturated state. The calculated $R_P$ is determined from the *S*-wave reflection coefficient ($R_S$) using the local mudrock line relationship giving the equation:

where:

$$\Delta F(t) = R_P(t) - g(t)R_S(t) \qquad 3.19$$

$t$ = two-way time
$\Delta F(t)$ = fluid factor trace
$R_P$ = *P*-wave reflectivity trace
$R_S$ = *S*-wave reflectivity trace
$g(t)$ = $M(V_S/V_P)$ = a slowly time-varying gain function (*geo-gain* term)
$M$ = Slope of the mudrock line, which can be an appropriate local value rather than that of the global mudrock line (Castagna et al., 1985)

### *3.5 Lambda-Mu-Rho Analysis*

Lambda-Mu-Rho Analysis (LMR) aims to extract lithology and pore fluid information from seismic and well log data. The conversion of velocity measurements to Lamé's modulii parameters of rigidity ($\mu$) and "incompressibility" ($\lambda$) offers new understanding into the original rock properties (Goodway et al., 1997). The Lamé parameters $\lambda, \mu,$ and $\rho,$ which represent "incompressibility", rigidity, and density respectively, allow for enhanced identification of reservoir zones. This is due in part to the fact that the compressibility (and hence the incompressibility) of a rock unit is very sensitive to pore fluid content, also to the fact that lithologic variations tend to be better characterized by changes in rigidity, "incompressibility", and density than changes in $V_P$ and $V_S$. In short, the strength of the method stems from the fact that these modulii relate directly to the pore fluid and lithology attributes of sedimentary and possibly carbonate rocks.

Standard analysis methods (*i.e.* Poisson's ratio) rely on $V_P$, $V_S$, and density differences. The elastic wave equation however, actually deals with the elastic modulii of the rocks, not the seismic velocity. *Castagna (1993)* mentions a link between velocity and rock properties for pore fluid detection, through the bulk modulus $k$ that is embedded in $V_P$. The bulk modulus is the stress-strain ratio under simple hydrostatic pressure, given by:

$$k = \frac{\Delta P}{\Delta V / V} = \frac{1}{C} \qquad 3.20$$

where,

| | | |
|---|---|---|
| $\Delta P$ | = | hydrostatic stress |
| $\Delta V/V$ | = | volumetric strain or dilatation |
| $C$ | = | compressibility |

Typical values of bulk modulus are (*dynes/cm*$^2$):

| | |
|---|---|
| Limestone (matrix) | 60 |
| Sandstone (matrix) | 40 |
| Sandstone pore volume | 0.9 |
| Water | 2.38 |
| Oil | 1.0 |
| Gas | ***0.021*** |

Both $k$ and $V_P$ have the sensitive pore fluid indicator $\lambda$ diluted by variable factors of $\mu$ ( rock matrix indicator). These relationships can be seen in the following equations:

$$V_P{}^2 = \frac{(k + (4/3)\mu)}{\rho} = \frac{(\lambda + 2\mu)}{\rho} \qquad V_S{}^2 = \frac{\mu}{\rho}$$

The recommendation underlying LMR analysis is to use modulii/density relationships to velocity $V$ or impedances $I$. This is given as:

$$I_P{}^2 = (V_P\rho)^2 = \frac{(\lambda + 2\mu)}{\rho} \qquad I_S{}^2 = (V_S\rho)^2 = \mu\rho$$

Solving for $\lambda$ and $\mu$, gives the following equations:

$$\lambda\rho = I_P{}^2 - 2I_S{}^2 \qquad \mu\rho = I_S{}^2$$

Incompressibility *($\lambda$)* is non-physical unlike rigidity, but the extraction method can be seen as a way to remove the $\mu$ sensitive rock matrix to give the receptive pore fluid indicator $\lambda$.

The lambda-mu-rho analysis works well for log data, however for seismic data without an independent measurement of density (density log), the extraction of $\lambda$ and $\mu$ is uncertain with any confidence.

The usual starting point for seismic in AVO analysis is the approximation of the Zoeppritz equations given by Aki and Richards (1979). Their equation can be rewritten in terms of the modulii and density, given by:

$$R(\theta)=\frac{1}{4}\left(1+\tan^2\theta\right)\frac{\Delta(\lambda+2\mu)}{(\lambda+2\mu)}-2\left(\frac{V_P}{V_S}\right)^2\sin^2\theta\frac{\Delta\mu}{\mu}+\frac{1}{4}\left(1-\tan^2\theta\right)\frac{\Delta\rho}{\rho} \qquad 3.21$$

This equation does exhibit AVO variation for the modulii but is impractical for AVO analysis. An approximated form of the Zoeppritz equations to extract $P$- and $S$- reflectivities (*Gidlow et al. 1987, Fatti et al. 1994*) is used:

$$R(\theta)=\left(1+\tan^2\theta\right)\frac{\Delta I_P}{2I_P}-8\left(\frac{V_S}{V_P}\right)^2\sin^2\theta\frac{\Delta I_S}{2I_S}-\left(\frac{1}{2}\tan^2\theta-2\left(\frac{V_S}{V_P}\right)^2\sin^2\theta\right)\frac{\Delta\rho}{\rho} \qquad 3.22$$

Now having the *P and S* reflectivity ($R_P=\Delta I_P/I_P$, $R_S=\Delta I_S/I_S$) sections, the next phase is to create *P and S* impedance sections through acoustic impedance inversion. Next, these impedance volumes are used to extract $\lambda\rho$ and $\mu\rho$ sections.

***3.6 Three-parameter Zoeppritz extraction methods***

AVO methods have proven to provide useful information about the pore fluid constituents and lithology but the lack of ability to detect uneconomic gas-reservoirs (low-saturation "*fizz-water*") is a common criticism of AVO. In two-term AVO approximations, the *P*-wave velocity is always tied to the slope and intercept terms. The intercept is a P-wave velocity and density term and the slope is a *P*-wave velocity and *S*-wave velocity term. The *P*-wave velocity is extremely sensitive even at low saturations of gas but the density and *S*-wave velocity are unaffected. In three-term AVO approximations the *P*-wave, *S*-wave, and density terms are independent and may provide insight on the gas saturations. This density contrast volume has been investigated by Kelly et al. (2001) and Downton (2001) and the results have been successful in differentiating between an economic successful producing gas well and an uneconomic “*fizz-water*” well.

### *3.6.1 Kelly et al. method*

Kelly et al. (2001) approach to three-parameter AVO inversion is to break down the seismic data into the elastic constants: $\Delta V_P/V_P$, $\Delta V_S/V_S$, and $\Delta\rho/\rho$. They use the Aki and Richards (1980) equation:

$$R(\theta) = A + B\sin^2(\theta) + C\sin^2\tan^2(\theta) \qquad 3.23$$

Where A, B, and C are defined in terms of the rock property contrasts:

$$A = \frac{1}{2}\frac{\Delta V_P}{V_P} + \frac{1}{2}\frac{\Delta\rho}{\rho};$$
$$B = \frac{1}{2}\frac{\Delta V_P}{V_P} - 2\left(\frac{V_S}{V_P}\right)^2\left(2\frac{\Delta V_S}{V_S} + \frac{\Delta\rho}{\rho}\right);$$
$$C = \frac{1}{2}\frac{\Delta V_P}{V_P}.$$

Since equation (3.23) relates the reflection amplitudes to angle of incidence and not offset to following equations were used:

$$Stack_{Norm} = \frac{\sum Amp_i(x_i)}{\sum i} \qquad 3.24$$

$$\cong \frac{\int_{x1}^{x2} Amp_i(x_i)dx_i}{\int_{x1}^{x2} dx_i} \qquad 3.25$$

$$\cong \frac{\int_{\theta 1}^{\theta 2} Amp_i(\theta_i)\left(\frac{dx}{d\theta}\right)d\theta}{\int_{\theta 1}^{\theta 2}\left(\frac{dx}{d\theta}\right)d\theta} \qquad 3.26$$

Equation (3.24) is the discrete sum related with a normalized stack and expects that the traces summed be uniformly sampled with offset. This discrete sum of the normalized stack can be approximated by the continuous case given in equation (3.25) (Kelly et al., 2001). Since equation (3.23) is in terms of angle equation (3.25) is rearranged to give the more appropriate equation (3.26). Equation (3.26) is a linearized approximation and a collection of a least three angle stacks (spanning from smallest to greatest offset) is needed to perform an inversion for the rock property contrasts.

Kelly et al. applied this method with good success in Gulf of Mexico in an attempt to differentiate between producing and depleted gas fields. All of these fields exhibited a strong AVO anomaly but the density contrast volume did not show anomalous values at the depleted gas field.

### *3.6.2 Downton method*

Downton (2001) uses Bayes' theorem to derive a three-parameter non-linear AVO inversion. Bayes' theorem is used because geologic constraints can be invoked on the inversion from the available well control and petrophysical relationships. These constraints provide a more stable solution.

Downton begins with the Aki and Richards (1980) linearized approximation of the Zoeppritz equations:

$$R(\theta)=\frac{1}{2}\left(1-4\gamma^2\sin^2\theta\right)\frac{\Delta\rho}{\rho}+\frac{\Delta\alpha}{\alpha}\frac{1}{\cos^2\theta}-4\gamma^2\left(\frac{\Delta\beta}{\beta}\right)\sin^2\theta \qquad 3.27$$

where:

$R$ – offset dependent reflectivity
$\alpha$ – P-wave velocity
$\beta$ – S-wave velocity
$\rho$ – density
$\gamma$ – ratio of S-wave to P-wave velocity

Equation (3.27) is then rewritten in the matrix form:

$$\mathbf{Gm=d} \qquad 3.28$$

where:

**G** - linear operator
**m** - unknown parameter vector containing the velocity and reflectivity $[\Delta\alpha/\alpha, \Delta\beta/\beta, \alpha\nu\delta\, \Delta\rho/\rho]^T$
**d** - input data vector (offset-dependent reflectivity)

Bayes's theorem provides a theoretical framework to make probabilistic estimates of the unknown parameters ***m*** from uncertain data *a priori* information (Downton, 2001). By combining the likelihood function and the a priori probability function, a non-linear inversion algorithm is derived.

### *3.7 AVO Classification*

Seismic reflections from gas-charged sands exhibit a wide range of amplitude versus offset characteristics (Rutherford and Williams, 1989). The zero-offset reflection coefficient ($R_0$) and the Poisson's ratio ($\sigma$) contrast strongly determine the AVO response at a reflector. In many areas like the Gulf of Mexico, most gas reservoirs do not appear as *bright spots* but as *dim spots* and therefore a small zero-offset reflection coefficient. Rutherford and Williams (1989) developed an AVO classification scheme to explain several AVO effects. They described three AVO class types: 1) high-impedance sands, 2) near-zero impedance contrast sands, and 3) low-impedance sands. Castagna et al. (1998) introduced a fourth class, which is a variation of low-impedance sands.

The range of AVO effects for gas saturated sandstone reservoirs is analyzed with approximations to the Zoeppritz equations to determine the P-wave reflection coefficient as a function of angle of incidence. The model used by Rutherford and Williams (1989) was a gas sand reservoir ($\sigma$ = 0.15, $\rho$ = 2.0 g/cc) encased in shale ($\sigma$ = 0.38, $\rho$ = 2.4 g/cc). The class *I, II, III, and IV* curves on figure 3-4, show the Rutherford and Williams (1989) classification of gas sands with the addition of Castagna's (1998) class *IV* sand. This classification is based only on the normal-incidence reflection coefficient ($R_p$ = A) and the gradient *(B)* using Shuey's (1984) approximation.

Reasonable petrophysical assumptions for sandstone-shale intervals result in linear background trends for limited depth ranges on AVO intercept (*A*) and Gradient (*B*) crossplots. The background trend *B/A* becomes more positive with increasing background $V_P/V_S$. If a large depth range is selected for *A vs. B* crossplotting, and background $V_P/V_S$ varies significantly, a variety of background trends may be superimposed. This creates a less well-defined background relationship (Castagna et al., 1998).

Deviations from the background trend may be indicative of hydrocarbons. This is the basis of Smith and Gidlow's (1987) fluid factor and related indicators. Inspection of the *A*-*B* plane reveals that gas sands may exhibit variable AVO behavior. It is suggested that hydrocarbon-bearing sands should be classified according to their location in the *A*-*B* plane, rather than by their normal-incidence reflection coefficient alone (Castagna et al., 1998).

The top of a gas sand should plot below the background trend (more negative *A and B*), on the other hand the bottom of the gas sand should plot above the background trend (more positive *A and B*), assuming the medium directly below the gas sand has the same properties as the medium overlying the gas sand. Top of gas-sand amplitude increases with offset only for gas whose tops plot in the third quadrant of figure 3-5, here *A* and *B* are negative and amplitude becomes more negative (and greater in magnitude) with increasing offset.

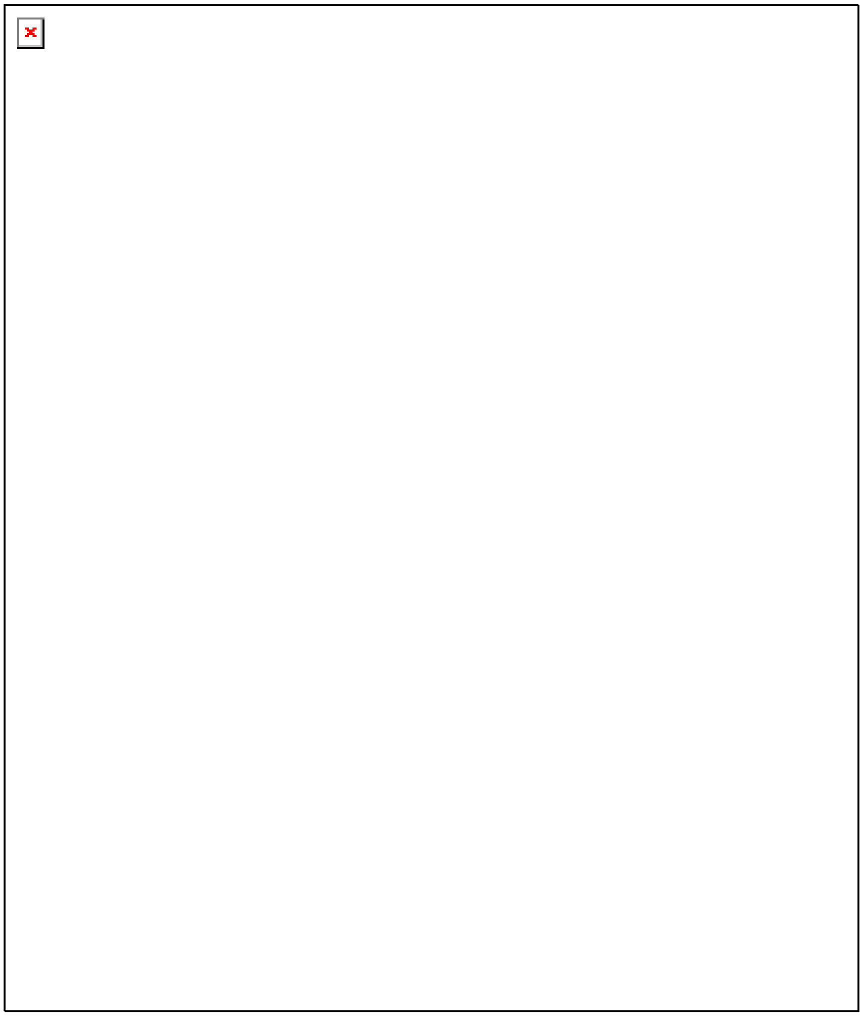

Figure 3-4: Plane-wave reflection coefficients at the top of each Rutherford and Williams classification of gas sand (Castagna et al., 1998).

Figure 3-5: Intercept (A) versus gradient (B) crossplot showing location of AVO class types. For a limited time window, brine-saturated sandstones and shales tend to fall along a well-defined background trend. Top of sand reflectors tend to fall below the background trend, whereas bottom of gas-sand reflections tend to fall above the trend. (Castagna et al., 1998)

***Class I Sands*** *(high impedance contrast sands)*

Class *I* sands have a positive normal-incidence reflection coefficient at the top of the sand and a negative normal-incidence reflection coefficient at the base of the sand. These sands lie in quadrant *IV*, and decrease in amplitude magnitude (dimming effect) with increasing offset faster than the background trend zone is definitely a class 1, high impedance sand.

***Class II Sands*** *(near-zone impedance contrast sands)*

Class *II* sands have a low normal-incidence coefficient (less than 0.02 in magnitude) at both top and bottom of gas sand, but achieve greater amplitude magnitude than the background at sufficiently high offsets. This type of sand is usually moderately compacted and consolidated. Polarity reversals are common with this type of reflector, which can lie in the *II, III,* and *IV* quadrants. Class 2 sands may or may not correspond to amplitude anomalies on stacked data.

***Class III Sands*** *(low impedance contrast sands)*

Class *III* sands have a strongly negative normal-incidence reflection coefficient, which becomes even more negative with increasing offset. Class *III* sands are lower impedance than overlying shales (classical bright spots), and exhibit increasing reflection magnitude with offset. Class 3 sands are usually undercompacted and unconsolidated. The top of this zone is always a trough and the base is a peak on seismic data.

***Class IV Sands*** *(low impedance contrast sands)*

Class *IV* sands, which fall in quadrant *II*, also have a large negative *A* but positive *B*. These are true bright spots, but reflection magnitude decreases with increasing offset. Since the AVO gradient from a class *IV* brine sand may be almost identical to the gradient from a class *IV* gas sand, these gas sands may be difficult to detect by the conventional approach of comparing partial offset stacks. Class *IV* gas sands frequently occur when porous sand is overlain by a high velocity unit, such as hard shale, siltstone, tightly cemented sand, or a carbonate.

It is important to note that whereas class *IV* gas sands exhibit unexpected absolute AVO behavior according to established rules of thumb and are difficult to interpret on partial offset stacks or using product (A*B) indicators, they do not confound A vs. B crossplot indicators such as Smith and Gidlow's (1987) fluid factor.

## 4.0 FLUID REPLACEMENT MODELLING

Fluid replacement or substitution modelling is an important aspect of seismic attribute work, because it may provide a useful tool for modelling and qualifying the various fluid scenarios that may produce an observed seismic amplitude response (Smith et al. 2003). This provides the interpreter a basis for interpreting the modeled AVO responses associated with the various substituted fluid scenarios. An understanding of the rock physics is essential for the interpretation of AVO anomalies. Several mathematical models have been developed that describe the effects of pore fluids on rock density and seismic velocity (Gassmann, 1951; Biot, 1956 and 1962; Kuster and Toksöz, 1974; O'Connell and Budiansky, 1974; Mavko and Jizba, 1991); (Batzle and Wang, 1992). The most common and practical method of fluid substitution is the low-frequency Gassmann theory (1951).

### *4.1 Gassmann fluid substitution method*

The Gassmann equations (1951) have been used for the calculation of the effects of fluid substitution on seismic properties using rock frame properties (Wang, 2001). These equations relate the bulk modulus of the rock to its frame, pore, and fluid properties. This method requires that the effect of the starting fluid first be removed prior to modelling the new fluid (Smith et al. 2003). The first step is to drain the rock of its initial pore fluid, and then the bulk modulus, shear modulus, and bulk density is calculated. Once the porous frame properties are accurately calculated, the rock is saturated with the new pore fluid, and then the new effective bulk modulus and density are calculated (Smith et al. 2003).

The equations for *P*-wave and *S*-wave velocity derived in their most fundamental form using the Lamé coefficients are given by:

$$V_P = \sqrt{\frac{\lambda + 2\mu}{\rho}} = \sqrt{\frac{k + 4/3\mu}{\rho}} \qquad 4.1$$

$$V_s = \sqrt{\frac{\mu}{\rho}} \qquad 4.2$$

Where, $\lambda$ is the Lamé parameter lambda (incompressibility), $\mu$ is the Lamé parameter mu (shear modulus), $k$ is the bulk modulus and $\rho$ is the density. These velocity equations however, do not take the water saturation into account. These equations are designed to derive velocity of a solid rock (i.e. no porosity). The AVO response is dependent on the properties of P-wave velocity ($V_P$), S-wave velocity ($V_S$), and density (ρ) in a porous reservoir rock. This involves the matrix material, the porosity, and the fluids filling the pores. Density effects can be modeled using Wyllie's formula (Wyllie et al., 1958):

$$\rho_{sat} = \rho_m(1-\phi) + \rho_w S_w \phi + \rho_{hc}(1 - S_w)\phi \qquad 4.3$$

Where, $\rho_{sat}$ is the density of the saturated rock volume, $\rho_m$ is the density of the rock matrix, $\rho_w$ is the density of water, $\rho_{hc}$ is the density of the hydrocarbon, $\phi$ is the porosity, and $S_w$ is the water saturation. Independently, Gassmann (1951) and Biot (1956) developed the theory of wave propagation in fluid saturated rocks, by deriving expressions for the saturated bulk and shear modulus, and substituting into the regular equations for P- and S-wave velocity:

$$V_P = \sqrt{\frac{K_{sat} + \frac{4}{3}\mu_{sat}}{\rho_{sat}}} \tag{4.4}$$

$$V_s = \sqrt{\frac{\mu_{sat}}{\rho_{sat}}} \tag{4.5}$$

Where $K_{sat}$ is the saturated bulk modulus, $\mu_{sat}$ is the saturated shear modulus, and $\rho_{sat}$ is the saturated density. The $\rho_{sat}$ is derived using the Wyllie's formula that was discussed earlier. In the Biot-Gassmann equations, the shear modulus does not change for varying saturation at constant porosity. Therefore, the shear modulus of the saturated rock ($\mu_{sat}$) equals the shear modulus of the dry rock ($\mu_{dry}$). This is assumed because shear waves should not be affected by pore fluid since they cannot travel through fluids. The bulk modulus equation is given by:

$$K_{sat} = K_{dry} + \frac{(1 - \frac{K_{dry}}{K_m})^2}{\frac{\phi}{K_{fl}} + \frac{1-\phi}{K_m} - \frac{K_{dry}}{K_m^2}} \tag{4.6}$$

where, $K_{sat}$ is the bulk modulus of the saturated rock, $K_{dry}$ is the bulk modulus of the dry rock, $K_m$ is the bulk modulus of the matrix drained of any pore filling fluid, $K_{fl}$ is the bulk modulus of the fluid, $\rho$ is the bulk density. The bulk modulus of the solid rock matrix ($K_m$) is usually taken from published data that were derived by measurements on core samples if no core data is readily available. The fluid bulk modulus ($K_{fl}$) can be modeled using the following equation:

$$\frac{1}{K_{fl}} = \frac{S_w}{K_w} + \frac{1 - S_w}{K_{hc}} \tag{4.7}$$

where, $K_w$ is the bulk modulus of water and $K_{hc}$ is the bulk modulus of the hydrocarbon. If the fluid modulus of the hydrocarbon is not known it is also taken from published data. The initial bulk modulus of the dry rock ($K_{dry}$) can be found by using the following equation:

$$K_{dry} = (1 - y)K_m \qquad 4.8$$

Porosity also affects the dry bulk modulus, and this effect can be estimated by using the following equation:

$$\frac{\phi}{K_P} = \frac{1}{K_{dry}} - \frac{1}{K_m} \qquad 4.9$$

where $K_P$ is the pore bulk modulus. Once the new effective bulk modulus and density are calculated they can used in equations 4.5 and 4.6 to calculate the P-wave and S-wave velocities for the new pore fluid.

### *4.1.1 Gassmann model assumptions*

The application of Gassmann's equations is based on several assumptions (Smith et al. 2003). The first assumption is the rock must be homogeneous and isotropic and the pore spaces are entirely connected. The pore space connectivity assumption may be violated for low porosity rock and carbonates. The second assumption is that the Gassmann equations are valid only at low enough frequencies such that pore pressures are equalized over length scale much greater than the pore dimension and much less than the wavelength of the of the passing seismic wave (Smith et al., 2003).

## *4.2 Batzle and Wang Fluid Modelling*

One of the shortfalls of the Gassmann method (1951) is that the densities, bulk modulii, velocities, and viscosities of common pore fluids are oversimplified. Batzle and Wang (1992) defined empirical relationships that estimate hydrocarbon bulk modulus (compressibility) and density based on reservoir temperature and pressure, oil and gas gravity, gas to oil ratio (GOR), and salinity. They used a combination of thermodynamic relationships, empirical trends, and data (new and published) to examine the effects of pressure, temperature, and composition on these important properties of hydrocarbon gases, hydrocarbon oils, and brines (Batzle and Wang, 1992).

Fluid properties can vary significantly from anticipated values which may cause costly interpretive errors. The bulk modulus and density of hydrocarbon oils increase with molecular weight and temperature but decrease with pressure (Wang, 2001). Large amounts of gas can go into solution in lighter oils and substantially lower the modulus and viscosity (Batzle and Wang, 1992).

#### *4.2.1 Gas*

Gas is the simplest phase to differentiate, when a reasonable guess of the gas gravity is known, a good estimate can be acquired at a specific temperature and pressure. Batzle and Wang derive gas densities using the equation:

$$\rho \cong \frac{28.8GP}{ZRT_a} \qquad 4.10$$

where,

$$Z = [0.03 + 0.00527(3.5 - T_{pr})^3]P_{pr} + (0.642T_{pr} - 0.007T_{pr}^4 - 0.52) + E \qquad 4.11$$

and

$$E = 0.109(3.85 - T_{pr})^2 \exp\{-0.45 + 8(0.56 - 1/T_{pr})^2 P_{pr}^{1.2} / T_{pr}\} \qquad 4.12$$

where $P$ is the pressure, $R$ is the gas constant, $T_a$ is the absolute temperature, $G$ is the specific gravity, $\rho$ is the density, $Z$ is the compressibility factor, $T_{pr}$ is the pseudocritical temperature, and $P_{pr}$ is the pseudocritical pressure. The gas densities increase with pressure and decrease with temperature as seen in Figure 4-1.

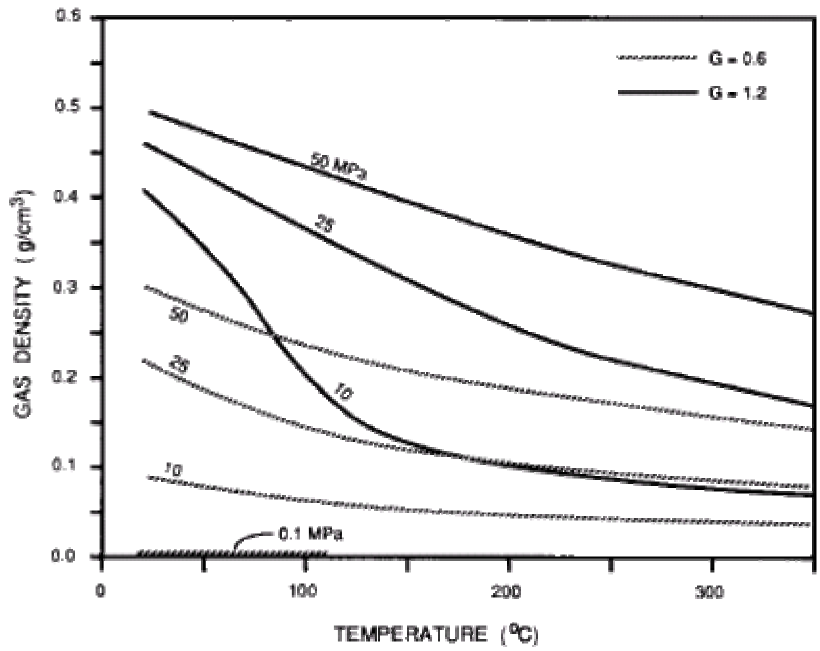


Figure 4-1: Hydrocarbon gas densities as a function of temperature, pressure, and composition (Batzle and Wang, 1992).

The velocities calculated from Thomas et al., (1970) from the equation of state show slight error when compared to direct measurements. These equations are still used to calculate velocities for various gas compositions because of their applicability (Batzle and Wang, 1992).

***4.2.2 Oil***

The oil phase is more difficult to characterize than the gas phase. Oils range from light liquids to very heavy tars. Light oils under pressure can absorb large quantities of hydrocarbon gases, which drastically decrease the density and velocity (Batzle and Wang, 1992). The variable compositions and ability to absorb gases produce wide variations in seismic properties of oils (Batzle and

Wang, 1992). Crude oils are typically classified using the American Petroleum Institute oil gravity (API) number defined by:

$$API = \frac{141.5}{\rho_o} - 131.5 \qquad 4.13$$

where $\rho_o$ is the oil density.

Wang (1988) and Wang et al. (1988) studied the effects of pressure, temperature, and compositions on oil with respect to velocity. They developed the following relationship:

$$V = 15450\,(77.1 + API)^{-1/2} - 3.7T + 4.64P + 0.0115(0.36API^{1/2}) - 1)TP \qquad 4.14$$

where $V$ is the velocity in m/s. Figure 4-2 shows that the oil densities increase with pressure and decrease with temperature. Also the density decrease with increasing API values.

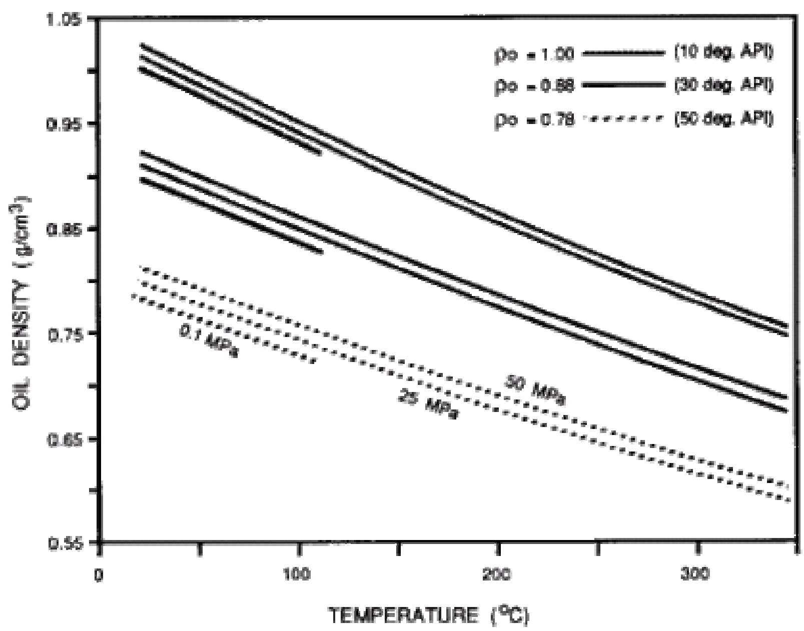


Figure 4-2: Oil densities as a function of temperature, pressure, composition (Batzle and Wang, 1992).

Saturated (live oils) should have different properties from gas-free-oils (dead oil). The original fluid in-situ is usually characterized by $R_G$, the gas-oil-ratio (GOR). This is the volume ratio of liberated gas to remaining oil at atmospheric pressure and 15.6°C (Batzle and Wang, 1992). The maximum amount of gas that can be dissolved in oil is a function of pressure, temperature, and composition of both the gas and oil (Batzle and Wang, 1992). This can be described by the following equation:

$$R_G = 2.03G[P \exp (0.02878\, API - 0.00377\, T)]^{1.205} \qquad 4.15$$

where $R_G$ is in Litres/Litre and G is the gas gravity. Equation 4.15 shows that the higher the API oil values the more gas can be absorbed into solution. Figure 4-3 shows a comparison of live and dead oil velocities.

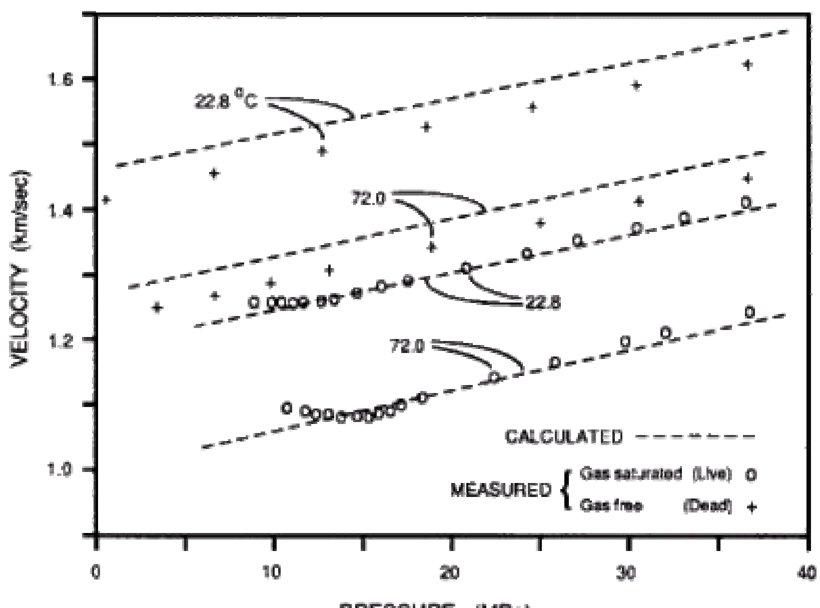


Figure 4-3: Acoustic velocities of both live and dead oils (Wang et al., 1988).

It can be seen on this figure that the effect of the gas drastically decreases the velocity of the live oils. The bubble point or saturation pressure can be seen at approximately 18 MPa, free gas exsolves and calculated velocities depart from measured values (Batzle and Wang, 1992).

Densities of live oils can be obtained from the following equation:

$$\rho_G = (\rho_0 + 0.0012GR_G)/B_0 \qquad 4.16$$

where $\rho_G$ is the density at saturation. Due to the gas effect the density values will decrease with increasing pressure or depth as more gas goes into solution (Batzle and Wang, 1992).

### *4.2.3 Brine*

Brines are the most common pore fluids and can range from near pure water to saturated saline solution (Batzle and Wang, 1992). The thermodynamic properties of brines have been studied in detail. Helgeson and Kirkham (1974) calculated a variety of properties for pure water over a broad temperature and pressure range. From their calculated values for density, thermal expansion, isothermal compressibility, and constant pressure heat capacity, the heat capacity ratio for pure water can be derived using the following equation:

$$\frac{1}{\gamma} = 1 - \frac{T_a \overline{V} \alpha^2}{C_P \beta_T} \qquad 4.17$$

where $\gamma$ is the ratio of heat capacity at constant pressure to heat capacity at constant volume, $T_a$ is the absolute temperature, $V$ is the molar volume, $C_P$ is the heat capacity, a is thermal expansion, $\beta_T$ is the isothermal compressibility. Using the heat capacity ratio with the tabulated density and compressibility Helgeson and Kirkham (1974) plotted the acoustic velocities in figure 4-4.

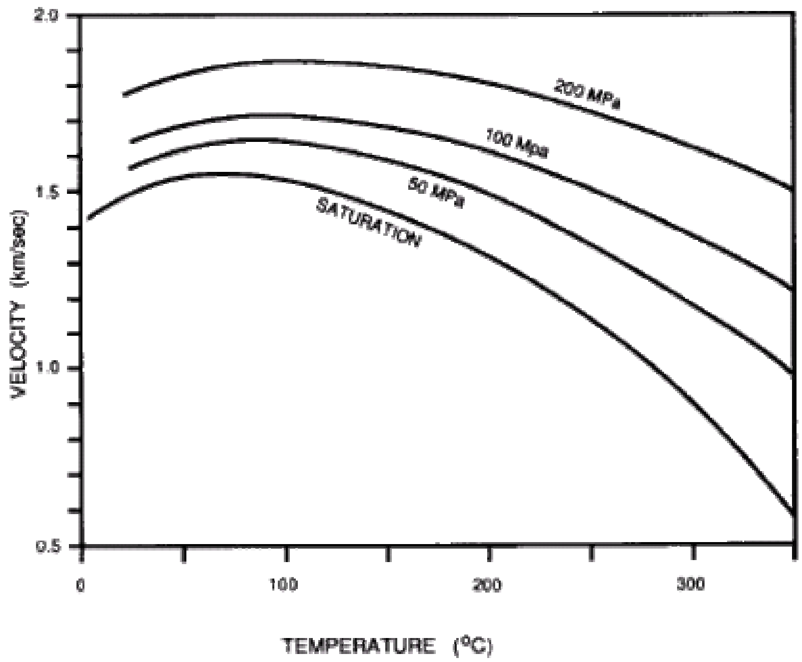


Figure 4-4: Sonic velocity of pure water as a function of temperature and pressure (Helgeson and Kirkham, 1974).

It can be seen on this figure that the velocity decreases with decreasing pressure and increasing temperature. The saturation curve is where liquid and vapour are at equilibrium.

Using relations from Rowe and Chow (1970), Zarembo and Fedorov (1975), and Potter and Brown (1977), Batzle and Wang (1992) formulated the following brine density relations:

$$\rho_W = 1 + 1 \times 10^{-6}(-80T - 3.3T^2 + 0.00175T^3 + 489P - 2TP + 0.016T^2P - 1.3 \times 10^{-5}T^3P - 0.333P^2 - 0.002TP^2) \quad 4.17$$

$$\rho_B = \rho_W + S\{0.668 + 0.44S + 1 \times 10^{-6}[300P - 2400 PS + T(80 + 3T - 3300S - 13P + 47PS)]\} \quad 4.18$$

where $\rho_W$ and $\rho_B$ are the densities of water and brine in g/cm$^3$ and $S$ is the weight fraction of sodium chloride. Figure 4-5 shows brine density as a function of pressure temperature and salinity. It can be seen that increasing salinity increases the density of brine, increasing pressure increases density and increasing temperature decreases density of brine.

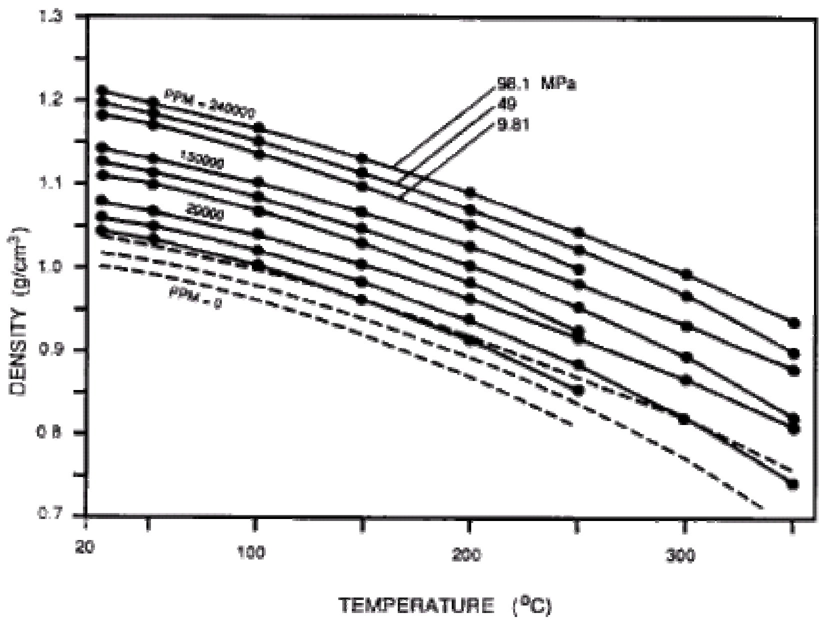


Figure 4-5: Brine density as a function of pressure, temperature, and salinity (Batzle and Wang, 1992).

#### *4.2.4 Fluid replacement considerations*

To use the Batzle-Wang fluid modelling effectively, knowledge of the assumptions is crucial. Batzle and Wang (1992) state in their paper several of the key assumptions they use in their methodology.

Firstly, rocks are not inert and passive skeletons usually assumed in composite media theory. Typically rocks contain bound water at a mineral scale that may influence the properties on the rock. This effect will increase with decreasing grain or pore size where mineral surfaces will increase.

As the pore space decreases in a rock the boundary conditions change. Batzle and Wang (1992) assume that when a wave passes through a rock the heat could not be conducted and that the process was adiabatic. As a wave passes through a rock space it travels though a mixture of liquid and gas phases. . If the particle size of the mixture is small enough, the process is isothermal – not adiabatic. These effects however, are quite small.

Surface tension is another neglected factor. If a fluid develops a surface tension at an interface, then a phase in a bubble within this fluid will have a slightly higher pressure (Batzle and Wang, 1992).

Lastly, no matter how well we think we understand the behaviour of the fluids, in natural systems the fluid behaviour is very complex. These methods provide a means of estimating approximate values through approximations and relationships. More detailed methods are very extensive and are typically very time consuming.

## 5.0 SIMULTANEOUS INVERSION

### *5.1 Introduction*

The *Jason RockTrace* inversion program is used in this analysis. This program simultaneously inverts for P-impedance, S-impedance or $V_P/V_S$, and density using angle limited stacks of the seismic data. Calculating the acoustic impedance, shear impedance, and density volumes provides a quantitative measure of the rock properties that generate AVO anomalies on reflectivity data (Jason users manual).

### *5.2 Method*

The simultaneous inversion algorithm works by initially estimating the angle dependent PP reflectivities from the input angle limited stacks. These are then used with the Zoeppritz equations to find bandlimited reflectivities (Pendrel and Dickson, 2003). The relation between the AVA reflection coefficients $R_{PP}$ and the elastic parameters can be given by the Knott-Zoeppritz relation (Aki and Richards, 1980):

$$\begin{bmatrix} \sin\theta_1 & \cos\phi_1 & -\sin\theta_2 & \cos\phi_2 \\ -\cos\theta_1 & \sin\phi_1 & -\cos\theta_2 & -\sin\phi_2 \\ \sin 2\theta_1 & \frac{V_{P1}}{V_{S1}}\cos 2\phi_1 & \frac{\rho_2 V_{S2}^2 V_{P1}}{\rho_1 V_{S1}^2 V_{P2}}\sin 2\theta_2 & \frac{\rho_2 V_{S2} V_{P1}}{\rho_1 V_{S1}^2}\cos 2\theta_2 \\ \cos 2\phi_1 & \frac{-V_{S1}}{V_{P1}}\sin 2\phi_1 & \frac{-\rho_2 V_{P2}}{\rho_1 V_{P1}}\cos 2\phi_2 & \frac{-\rho_2 V_{S2}}{\rho_1 V_{P1}}\sin 2\phi_2 \end{bmatrix} \begin{bmatrix} r_{pp} \\ r_{ps} \\ r_{sp} \\ r_{ss} \end{bmatrix} = \begin{bmatrix} -\sin\theta_1 \\ -\cos\theta_1 \\ \sin 2\theta_1 \\ -\cos 2\phi_1 \end{bmatrix} \qquad 5.1$$

The subscripts 1 and 2 the layers above and below the reflection interface. The angles $\theta$ and $\phi$ refer to the angles of P- and S-waves, respectively. The relation between the AVA reflection coefficients $R_{PP}$ and elastic parameters can also be approximated using the Aki-Richards approximation:

$$R_{PP} = \left(1+\tan^2\theta\right)\frac{V_{P2}-V_{P1}}{V_{P2}+V_{P1}} + \left(-8K\sin^2\theta\right)\frac{V_{S2}-V_{S1}}{V_{S2}+V_{S1}} + (1-4K\sin^2\theta)\frac{\rho_2-\rho_1}{\rho_2+\rho_1} \qquad 5.2$$

where:

$$K = \frac{\overline{V}_S^2}{\overline{V}_P^2} \qquad 5.3$$

where θ is the down going p-wave (Jason users manual).

The bandlimited elastic reflectivities are then merged with their low frequency counterparts from the input model derived from the well control. These approximate results are then improved in a final inversion for P-impedance, S-impedance, and density (Pendrel and Dickson, 2003). These are subject to various hard and soft constraints on the inversion. The inversion algorithm used is the *Jason constrained sparse spike inversion (CSSI).* The AVA constrained sparse spike algorithm is based on an algorithm that, for each trace, solves the following optimization problem:

$$\mathrm{F} = \mathrm{F}_{\mathrm{reflectivity}} + \mathrm{F}_{\mathrm{contrast}} + \mathrm{F}_{\mathrm{seismic}} + \mathrm{F}_{\mathrm{trend}} + \mathrm{F}_{\mathrm{spatial}} + \mathrm{F}_{\mathrm{Gardner}} + \mathrm{F}_{\mathrm{mudrock}} \qquad 5.4$$

given constraints:

$v_{Pi}$ (lower) < $v_{Pi}$ < $v_{Pi}$ (upper)
$v_{Si}$ (lower) < $v_{Si}$ < $v_{Si}$ (upper)
$\rho_i$ (lower) < $\rho_i$ < $\rho_i$ (upper)

where $F_X$ are the respective measures of (misfit norms). The synthetic data is modeled by convolving the reflection coefficients with the wavelet (w):

$$s = w * r \qquad 5.5$$

The terms in the objective function are:

$L_p$ – norm of the reflectivity;
$L_p$ – norm of elastic constants misfit;
$L_p$ – norm of Gardner misfit;

$L_p$ – norm of mudrock relation;
$L_q$ – norm of seismic data misfit for all partial stacks (synthetic data – seismic data);
$L_1$ - norm of elastic parameters misfit to their respective trends (elastic parameter – elastic parameter trend);
$L_1$ – norm of spatial misfit of elastic parameters (soft spatial constraint)

The coefficient p is the reflectivity norm and q represents the seismic mismatch norm. The misfit norms are normalized using standard deviations (or variances, or uncertainties); the standard deviation of the seismic data mismatch is set in the form of a lambda factor ($\lambda$). This factor is used to control the balancing of the misfit norms. A low lambda factor will emphasize the $L_p$ reflection coefficients resulting in an acoustic impedance trace which has few sharp contrasts and little detail. High lambda value emphasize the $L_q$ seismic data mismatch term resulting in detailed acoustic impedance trace values (Jason users manual).

Trend models for P-impedance, S-impedance or $V_P/V_S$, and density are defined from the horizons, faults, and well control. *Hard trend constraints* can be defined by imposing $z_i$ (lower) and $z_i$ (upper) bounds on the trend models. The inversion results will then be constrained to fall within these bounds reducing the non-uniqueness of the results.

Soft constraints can also be used to stabilize the inversion results. Gardner and Mudrock relationships can be used to stabilize the contrast optimization and elastic parameters optimization. The soft Gardner constraint stabilizes the result by using the Gardner relationship (Gardner et al., 1974) to link the P-wave velocity to the density. The soft Mudrock constraint stabilizes the inversion result by using the Castagna et al. (1984) mudrock relationship to link the P-wave velocity to the S-wave velocity. However, there are drawbacks to using these soft constraints. By increasing the weight of the soft constraints the inversion result will be more stable but at the loss of seismic fit. Setting high values for the soft trends conforms the values to the relationship and therefore moving towards modeled values. Accurate density inversion results require input data with far offsets (>40 degrees). In the absence of far offset data the soft Gardner constraint, which will give density character that will follow the P-impedance values (Pendrel and Dickson, 2003).

## 6.0 NEURAL NETWORKS

The artificial neural network is a set of electronic components or a computer program that is designed to represent the way in which the brain processes information. The brain is a highly complex, non-linear, and parallel information processing system (Todorov, 2000). The use of neural networks to predict reservoir properties from seismic attribute volumes and well log data has become popular in recent years. Neural networks are an exploitation tool and therefore good well control is necessary for a meaningful prediction. The technology is used when the data relationships between the data are complex and non-linear in nature. Typically porosity, volume shale, water saturation, and seismic facies volumes are extracted using neural networks.

Two of the neural network architectures used by the Hampson-Russell Emerge program will be discussed: the multi-layer feedforward neural network (MLFN) and probabilistic neural network (PNN).

### *6.1 Multi-layer Feedforward Neural Network*

The multi-layer feedforward neural network consists of an input layer, an output layer, and one or more hidden layers (Hampson et al., 2001). The MLFN network basic architecture is shown in figure 6-1. It consists of a set of neurons, also called processing units or nodes, which are arranged into two or more layers (Todorov, 2000). The neurons are connected in the following fashion: inputs to neurons in each layer come from the outputs from the previous layer, and outputs from these neurons are passed to neurons in the next layer. In figure 6-1, there are four inputs in the input layer, three neurons in the hidden layer, and one output neuron, which would represent the predicted reservoir property. There are 12 connections between the inputs and the hidden layers neurons and three connections between the hidden layers neurons output neuron, which means that there are 15 weights.

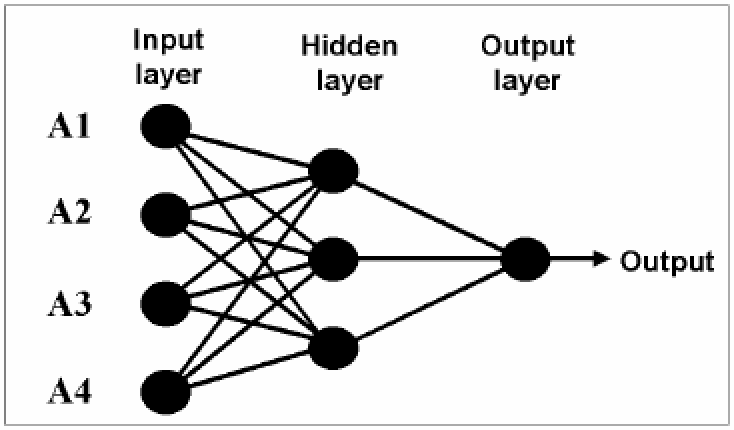


Figure 6-1: MLFN network architecture (Hampson et al., 2001).

The input layer has as many input neurons as input attributes. If a convolutional operator is used, the number of attributes is increased by the operator length (Hampson et al., 2001). The amount of neurons in the hidden layer is set by experimentation.

### *6.1.1 Training*

The major undertaking for the neural network is to learn a model by presenting it with examples, this is called *training*. Each example consists of an input – output pair: an input symbol and the corresponding desired response for the neural network (Todorov, 2000). The training process consists of finding the optimum weight between the neurons. The problem of estimating the weights can be considered a non-linear optimization problem, where the objective is to minimize the mean squared error between the actual target log values and the predicted target log values (Hampson et al., 2001).

***6.1.2 Overtraining and validation***

In theory, given sufficient neurons and iterations, the error based on the training set approaches zero (Todorov, 2000). For noisy data, this is generally undesired since the neural network will be fitting noise and some small details of the individual cases (Todorov, 2000). This overfitting of the data is called *overtraining* and is a pitfall of this method. Figure 6-2 shows a set of known and unknown points being fit to find a relationship. It can be seen if a high enough polynomial is used, the known points are fit precisely. When a smoothed function is used the unknown points are better fit. The number of neurons in a neural network is analogous to the polynomial degree and therefore a large number of neurons can lead to overfitting (Todorov, 2000).

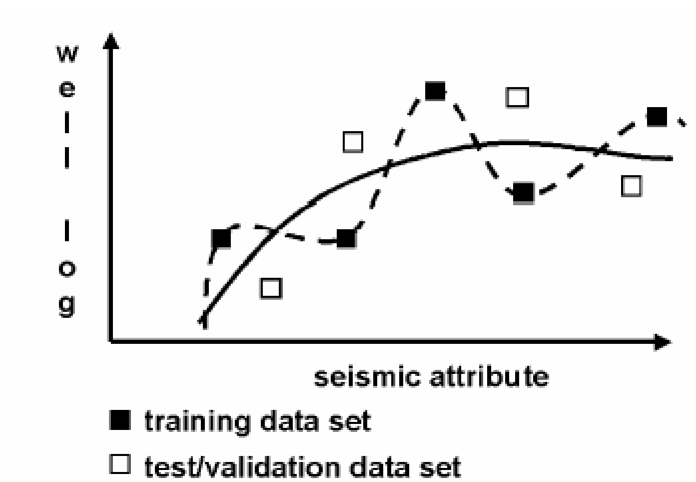


Figure 6-2: Overfitting versus generalization (Todorov, 2000).

The problem is how many neurons do we use to prevent overtraining? This can be solved by dividing the data into two data sets: training and validation

(Todorov, 2000). The training data set is used to train the neural network. When trained the network is applied to the validation data set for verification.

### *6.2 Probabilistic Neural Network*

The basic idea behind the general regression probabilistic neural network is to use a set of one or more measured values, called *independent variables*, to predict the value of a single *dependent variable* (Todorov, 2000). The PNN is a mathematical interpolation scheme, which utilizes neural network architecture for its implementation (Hampson et al., 2001).

The training data for the PNN is similar to that of the MLFN, as it contains a series of training "examples", one for each seismic sample in the analysis windows from all the wells (Hampson et al., 2001). Each example consists of data for a single time sample:

$$\begin{gathered}\{A_{11}, A_{21}, A_{31}, L_1\}\\ \{A_{12}, A_{22}, A_{32}, L_2\}\\ \{A_{13}, A_{23}, A_{33}, L_3\}\\ .\\ .\\ .\\ \{A_{1n}, A_{2n}, A_{3n}, L_n\}\end{gathered} \qquad 6.1$$

where $A_i$ are the attributes and $L_i$ is the measured target log values for each of the examples.

Given the training data, the PNN assumes that each new output log value can be written as a linear combination of the log values in the training data (Hampson et al., 2001):

$$x = \{A_{1j}, A_{2j}, A_{3j}\} \qquad 6.2$$

The goal is to estimate the unknown dependent variable, y', at the location where the independent parameters are known (Todorov, 2000). This equation is based on the fundamental equation of the general regression probabilistic neural network (Todorov, 2000):

$$y'(x) = \frac{\sum_{i=1}^{n} y_i \exp(-D(x, x_i))}{\sum_{i=1}^{n} \exp(-D(x, x_i))} \qquad 6.3$$

where $n$ is the number of samples and $D(x, x_i)$ is given by:

$$D(x, x_i) = \sum_{j=1}^{p} \left( \frac{x_j - x_{ij}}{\sigma_j} \right)^2 \qquad 6.4$$

The term $D(x, x_i)$ represents the *'distance'* between the input point and each of the training points $x_i$ (Hampson et al., 2001). The *'distance'* is scaled by the quantity $\sigma_j$, called the *smoothing parameter*, which may be different for each independent variable (Todorov, 2000).

The training of this network consists of obtaining the best possible set of smoothing parameters, $\sigma_j$. The criterion for optimization is minimization of the validation error (Todorov, 2000). The validation result for the $m^{th}$ sample is defined as:

$$y'_m(x_m) = \frac{\sum_{i \neq m}^{n} y_i \exp(-D(x_m, x_i))}{\sum_{i \neq m}^{n} \exp(-D(x_m, x_i))} \qquad 6.5$$

This is the predicted value of the $m^{th}$ target sample when the sample is left out of the training data (Hampson et al., 2001). Since the actual value $y_m$ is known, the prediction error for that sample can be calculated. Repeating this process for each of the training samples, the total prediction error for the training data can be defined as:

$$E_V(\sigma_1, \sigma_2, \sigma_3) = \sum_{i=1}^{n} (L_i - \hat{L}_i)^2 \qquad 6.7$$

The prediction error depends on the chosen parameters for $\sigma_j$. The validation error is then minimized with respect to the smoothing parameters using the conjugate gradient method (Todorov, 2000). The resulting network has the property that the validation error is minimized (Hampson et al., 2001).

## 7.0 Hebron / Ben Nevis analysis

### 7.1 Introduction

The Hebron asset is comprised of Hebron, West Ben Nevis, and the Ben Nevis fields. This prospect is located in the southern portion of the Jeanne d'Arc Basin, approximately 350 kilometres from St. John's, Newfoundland (Figure 7-1). Significant discovery licenses covering this asset were awarded in the mid 1980's based on four exploratory wells over an area of approximately 36 square kilometres (Provais, 2000).


Figure 7-1: Hebron / Ben Nevis location map

Oil in place potential for the asset including un-drilled fault blocks is estimated to exceed 2 billion barrels. The CNOPB[1] states that there are 600 million barrels of recoverable oil, based on what has been already drilled (second largest after Hibernia). The upper Ben Nevis horizon encountered significant volumes of "heavy" gravity crude in the range of 19 to 21 degree API. Oil is usually classified as heavy if it has API gravities less than 10 degrees (1.0 specific gravity). Therefore, the oil encountered in the Ben Nevis is still not as dense as water.

[1] Canada-Newfoundland Offshore Petroleum Board

The density of this oil however still presents production challenges. The thicker oil would require special processing equipment and more than 100 wells might be needed for this development. The Hibernia and Jeanne d'Arc horizons encountered marginal volumes of lighter gravity crude. The Hibernia formation encountered 29-degree gravity oil and the Jeanne d'Arc encountered 30 to 36 degree gravity oil, values similar to that of the Hibernia oil field (Figure 7-2).

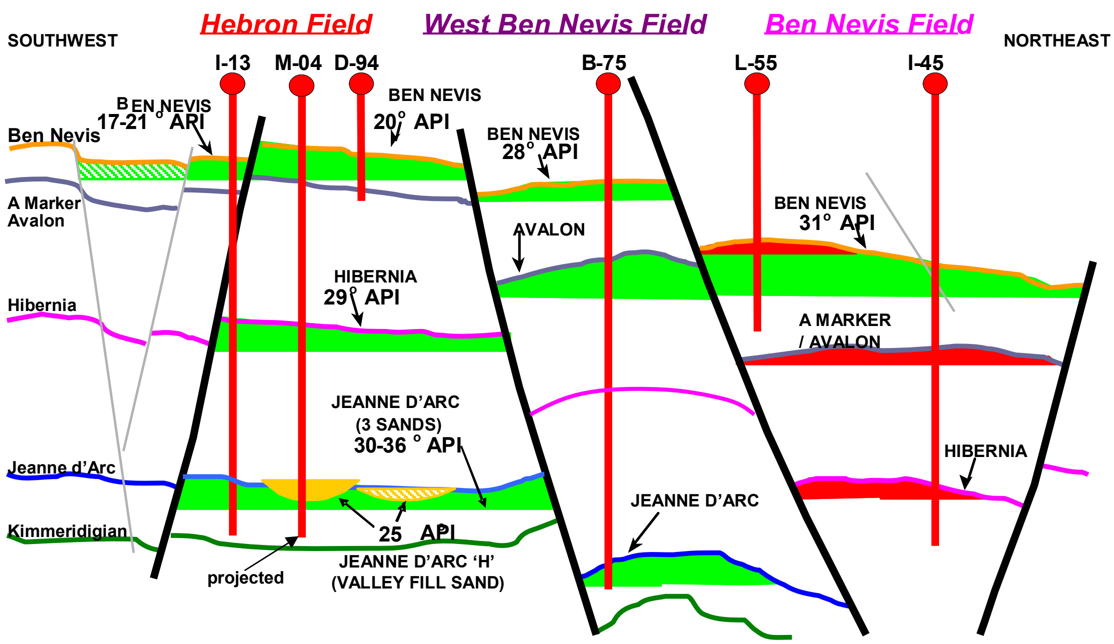


Figure 7-2: Schematic cross section of Hebron /Ben Nevis asset (ChevronTexaco).

AVO methods have been used to predict hydrocarbons in clastic reservoirs of offshore eastern Canada. AVO is quite useful due to the fact that it reduces the drilling risk, which is valuable for costly offshore drilling. This method proves to be an excellent exploration tool but traditionally it cannot distinguish between commercial and non-commercial (low hydrocarbon saturation) reservoir zones. This is because the P-wave velocity is very sensitive to the presence of a hydrocarbon in the pore space of a rock even at very low saturation of hydrocarbons. The S-wave velocity and density, however, are not as sensitive to low hydrocarbon saturations in the pore spaces. Using two-parameter AVO equations the P-wave velocity is always linked to the shear wave velocity or density and therefore there is no bias at lower hydrocarbon saturations. Lines (1999), Kelly et al. (2001), Downton (2001) and others have explored a three-parameter AVO extraction in order to get more information from P-wave seismic data in an attempt to isolate rock property contrasts. This method may prove to be an interesting approach at the Hebron / Ben Nevis prospect in an attempt to differentiate between the varying oil gravities.

## 7.2 Geology

### *7.2.1 Regional Geology*

The tectonostratigraphic evolution of the Grand Banks (Figure 7-3) during the Mesozoic and Cenozoic eras has been discussed in numerous papers (e.g. Enachescu, 1987; Grant et al., 1988; Tankard and Welsink, 1988; McAlpine, 1990; Keen and Dehler, 1993; Rees, 2001). Rees (2001) states all are similar in description but all share several main points: (1) the Jeanne d'Arc and adjacent basins were formed during a complex series of Mesozoic rift episodes, (2) the extensional deformation is thick-skinned, (3) sedimentary infill of the Jeanne d'Arc basin was varied in rate and type of sediment and was linked to fluctuations in sediment supply, structural movement and eustatic sea level change.


Figure 7-3: Distribution of Mesozoic Basins on the Grand Banks offshore Newfoundland (CNOPB)

### *7.2.2 Field Geology*

For this study the main focus is the uppermost Ben Nevis Formation reservoir. The Ben Nevis reservoir unconformibly overlays the A-Marker. The A-Marker is a laterally extensive Hauterivian to Barremian calcareous sandstone and is an excellent regional seismic marker. The Aptian unconformity between the Ben Nevis and the A-Marker represents a hiatus of several million years (Sinclair, 1988; Sinclair, 1995; Sinclair, 1993; Driscoll and Hogg, 1995). The Aptian / Albian Ben Nevis Formation is an extensive basin wide fining upward sequence of medium to very fine grained sandstone with a variable shale content (Rees, 2001). In the northeast portion of the field, the base of the Ben Nevis Formation has a laterally extensive thick shale that separates the Ben Nevis from the underlying A-Marker reservoir. The Ben Nevis was deposited during a marine transgression and reservoir quality degrades to the north, mainly as a function of decreasing grain size. The Ben Nevis is overlain by the Nautilus shale and provides a regional top seal for the Ben Nevis reservoirs.

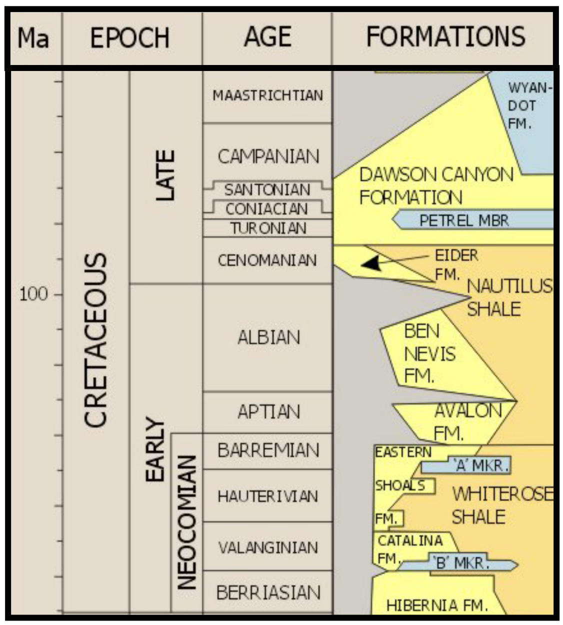


Figure 7-4: Jeanne d'Arc basin stratigraphic column (CNOPB)

The structure of the field is dominated by normal faults that cut the field into four major fault block zones: South graben, Hebron horst, West Ben Nevis, and Ben Nevis zones. The faulting is a part of a northwest-southeast trans-basin fault trend. These faults are thought to have played a major role in trapping hydrocarbons in terms of both sealing capacity and providing structural closure by the way of fault block rotation.

## 7.3 DATA

### *7.3.1 Well data*

Seven wells have been drilled to this point defining the Hebron asset shown in Figure 7-5. The discovery well drilled into the prospect was the Mobil et al. I-45 well in 1980. Two phases of drilling to further delineate the prospect followed the I-45 well. The first phase occurred in the mid 1980's and the second phase occurred from 1999 to 2000. In 1981 the first of the delineation wells was drilled, the Mobil et al. I-13 which also encountered hydrocarbon accumulations. In 1985, the Petro-Canada et al. B-75 well was drilled to test the structurally high point between the I-45 and I-13 wells. The Petro-Canada et al. H-71 well drilled in 1985 stepped out from the other wells to test lateral extent but encountered no significant hydrocarbon accumulations. After the first phase of drilling was completed the prospect was deemed uneconomic. After a progression of technology, establishment of infrastructure, and development of fields in the Jeanne d'Arc Basin, the consideration for the second phase of began. In early 1999, the Petro-Canada et al. D-94 well was drilled and encountered significant quantities of oil (~1 Billion STOOIP) in the Ben Nevis reservoir. The Chevron et al. L-55 well was drilled in 1999 to further evaluate the Ben Nevis reservoir adjacent to the I-45 discovery well. The last well was drilled in 2000; the Chevron et al. M-04 further tested the Hebron horst block.

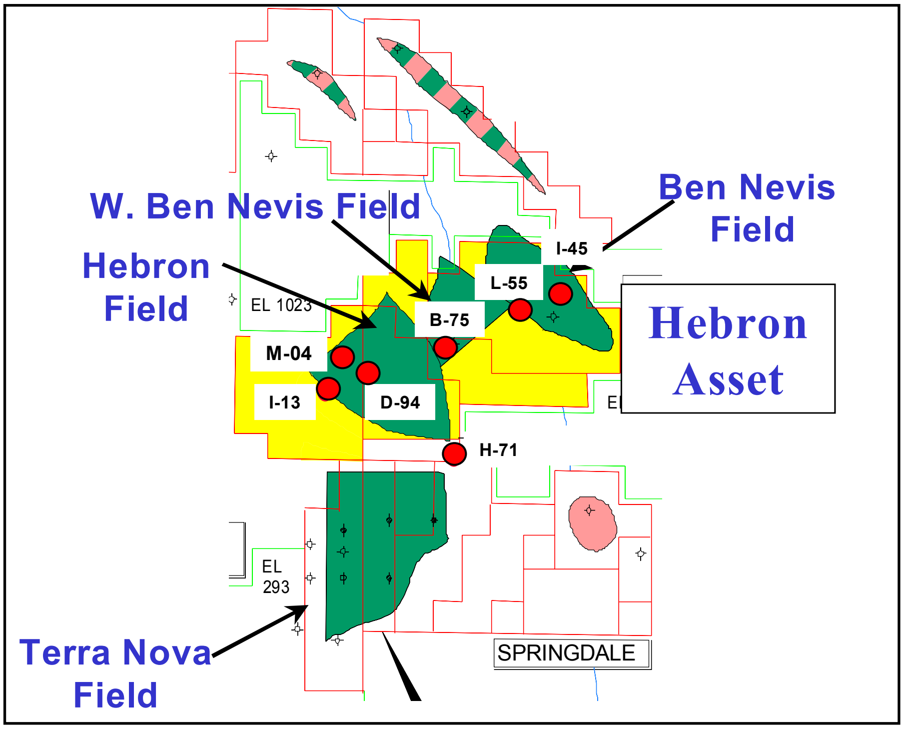


Figure 7-5: Hebron Asset map showing well locations (ChevronTexaco).

All the wells on the Hebron prospect contain a full suite of well-log data. The quality of the log data varied from fair for the 1980's wells to good for the more recent wells. The M-04, D-94, and L-55 log suites include dipole sonic logs. Thorough petrophysical analysis of these logs has been done in house at ChevronTexaco providing key geologic tops and a comprehensive *Multimin* analysis.

### *7.3.2 Seismic Data*

Initial exploration over the Hebron asset used the 2D GSI reconnaissance survey acquired in 1985. After significant discoveries were found using these 2D lines a need for better mapping for the area was necessary.

A 3D survey was acquired over the Cape Race, Hebron Ben Nevis, and Terra Nova licenses in the summer of 1997. This survey was acquired by PGS Exploration AS using the vessel *R/V Ramform Explorer*.

The survey consists of 93 lines each spaced 400 m with lengths from 11 km to almost 29 km. A total of 2332 sail km were acquired and the survey covers over 700 $km^2$. The Hebron/Ben Nevis portion of the survey consists of 28 shot lines with lengths varying from 27 to 29 km. A total of about 800 sail km were acquired for Hebron/Ben Nevis. This portion of the survey covers about 316 $km^2$.

All of the lines were shot in an east-west orientation (88.16 degrees, NAD-83). A two airgun array was used with the airguns separated by 50 m and a shot point interval of 25 m. A total of eight streamers, each with a cable length of 4050 m at a depth of 8m (+/- 1 m), were employed. Streamer separation was 100m. There were 162 groups with an interval of 25 m. The resulting nominal fold is 4100%.

The processing for this survey was done by CGG Canada Ltd. The processing sequence was designed to preserve relative amplitudes for AVO analysis. The detailed processing flow is described in Figure 7-6.

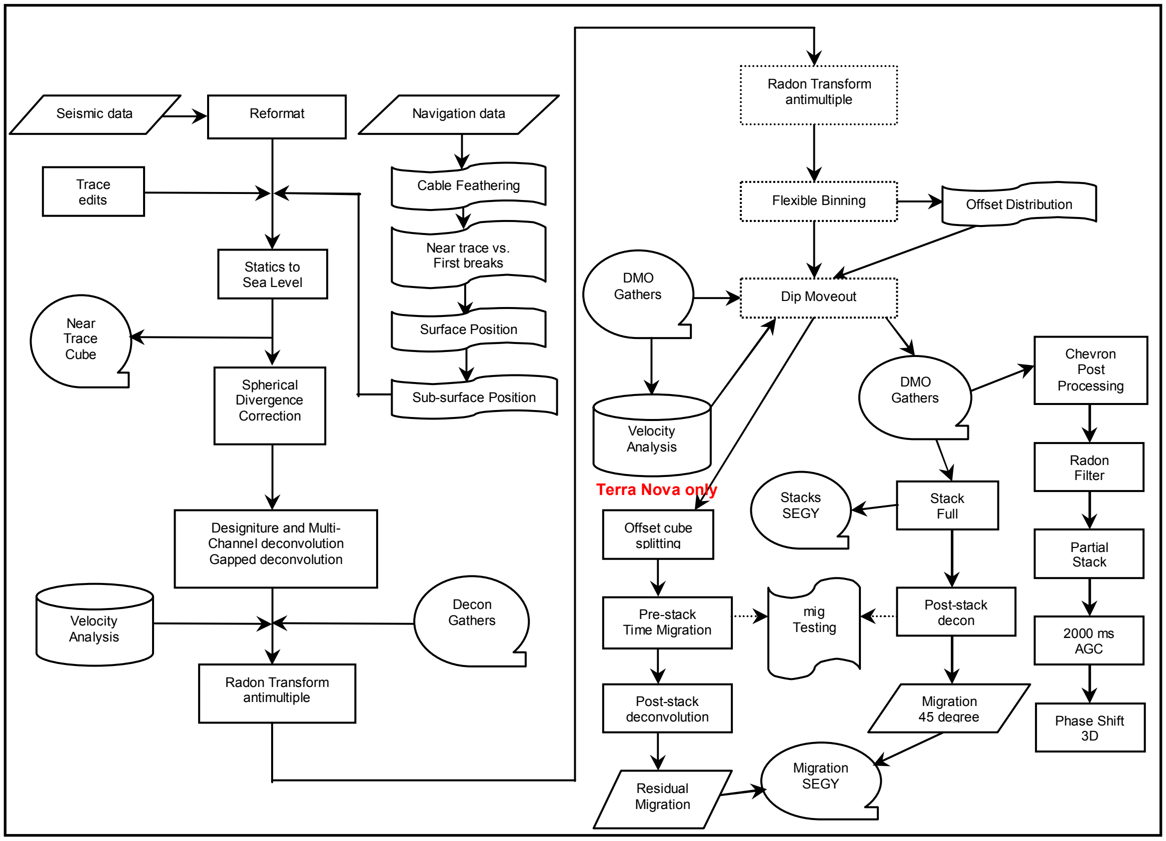


Figure 7-6: Processing flow.

### *7.3.3 VSP data*

Vertical seismic profiles (VSP) were acquired at the M-04, D-94, I-30, and L-55 well locations after drilling was completed. These were used to help in the correlation of the well data to the seismic. Also, wavelets were extracted and compared to those extracted from the seismic data.

## 7.4 Well log analysis and modelling study

In this analysis wells M-04 and L-55 are used all of which encountered pay. There are four key zones of interest: the Ben Nevis formation, Hibernia formation, Jeanne d'Arc "H" sand and Jeanne d'Arc "B" sand reservoirs. The Ben Nevis reservoir is of key interest for this thesis work due to its varying oil gravity across the Hebron/Ben Nevis oilfields. The goal of this analysis is to detect density differences using AVO methods in an attempt obtain density contrast volumes.

In order to get an understanding of the rock properties associated with the Ben Nevis zone Fluid Replacement Modelling (FRM) was performed on the two wells. These wells were used because they contained full waveform sonic (*P*-wave and *S*-wave), density, gamma ray, porosity, and other pertinent logs for modelling. The input logs for the M-04 well are shown in Figure 7-7, D-94 in figure 7-8, and L-55 in Figure 7-9.

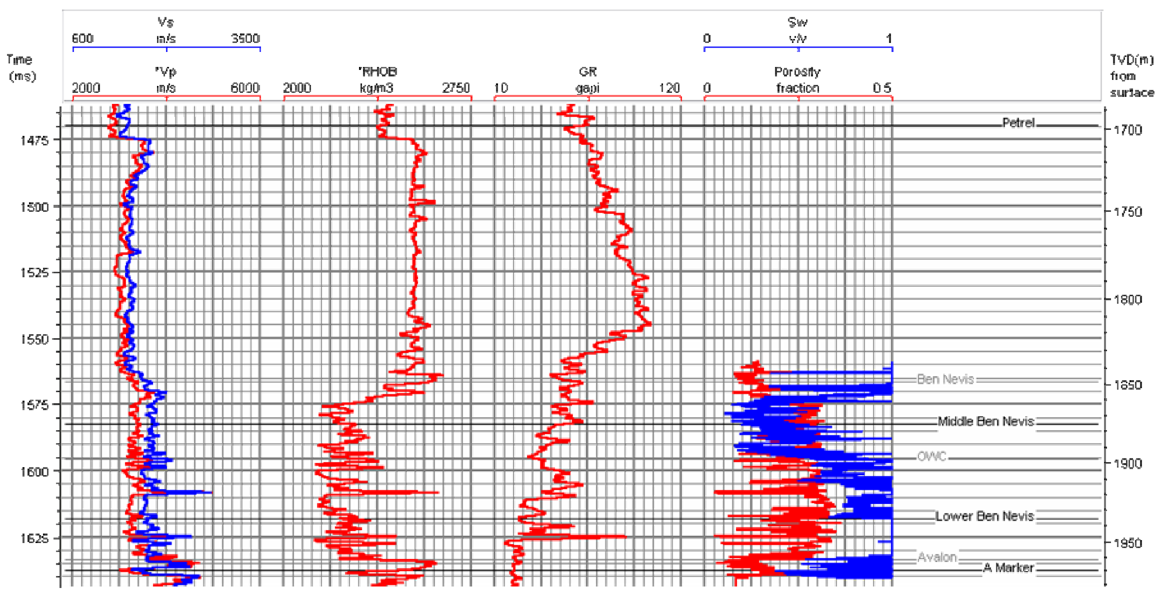


Figure 7-7: Original logs at M-04 well location.

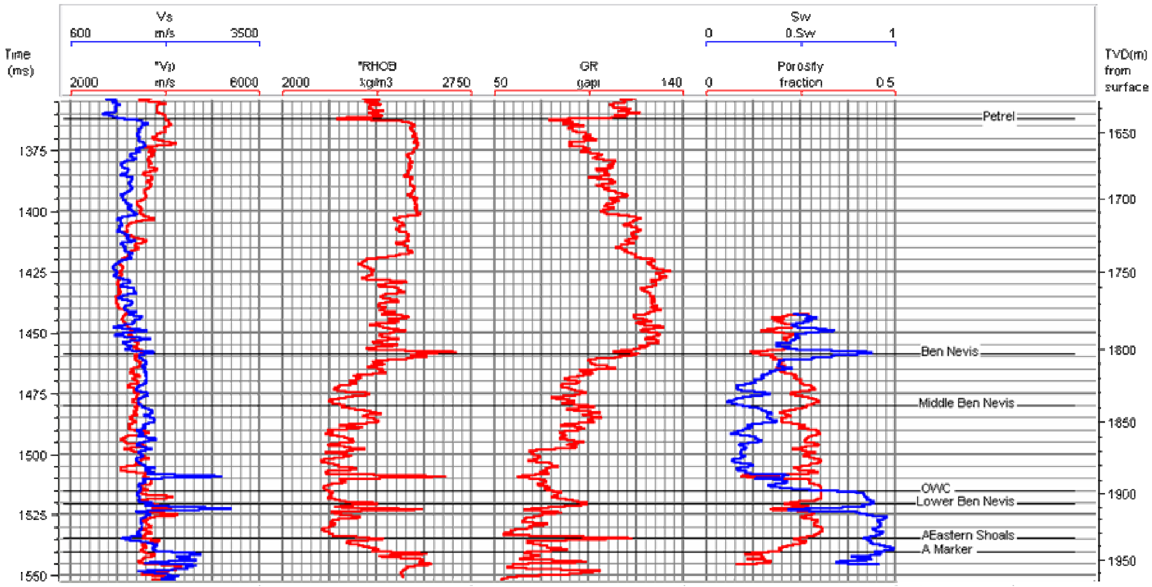


Figure 7-8: Original logs at D-94 well location.

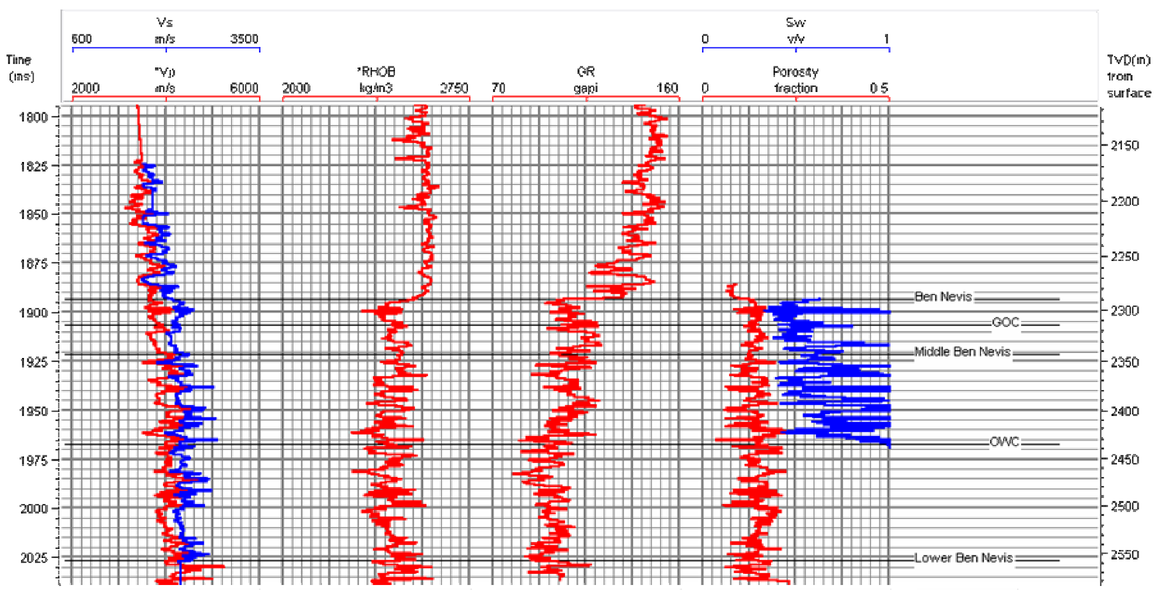


Figure 7-9: Original logs at L-55 well location

It can be seen on the well log plots that the reservoir quality in the M04 and D94 wells are superior compared to that of the L55 well. The water saturation is also much lower for the D94 and M04 wells.

### *7.4.1 Rock Property Relationships*

All of the wells on the Hebron asset are used to observe different rock property relationships. These may aid in distinguishing varying oil density values. Figure 7-10 is a crossplot of the Ben Nevis reservoir values versus depth across to asset. This figure shows that reservoir quality decreases with depth, as expected. In order for a good fluid density prediction the porosity, density, and P-wave velocity behaviour must be well understood.

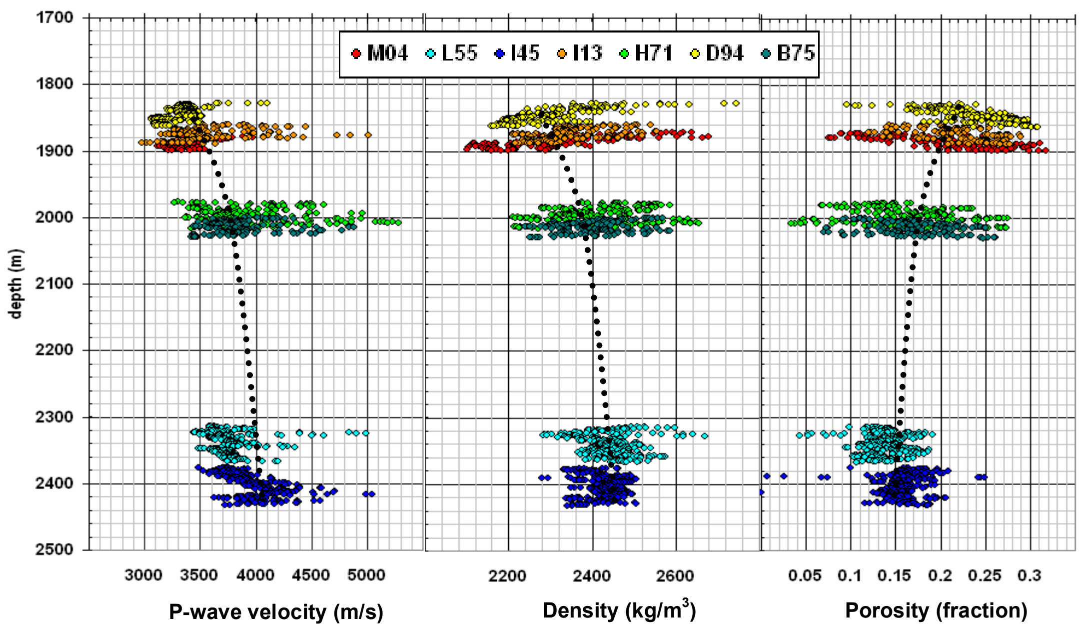


Figure 7-10: Porosity, density, and P-wave velocity plotted versus depth for all wells in the Ben Nevis zone on the Hebron asset.

Figures 7-11 to 7-13 show the relationships between P-wave velocity, porosity, density and P-impedance in the Ben Nevis zone. These indicate that the shallower Ben Nevis pay zones are easier to isolate because the deeper zones overlap the background trend. The variable oil density values are not detectible due to the different reservoir rock properties.

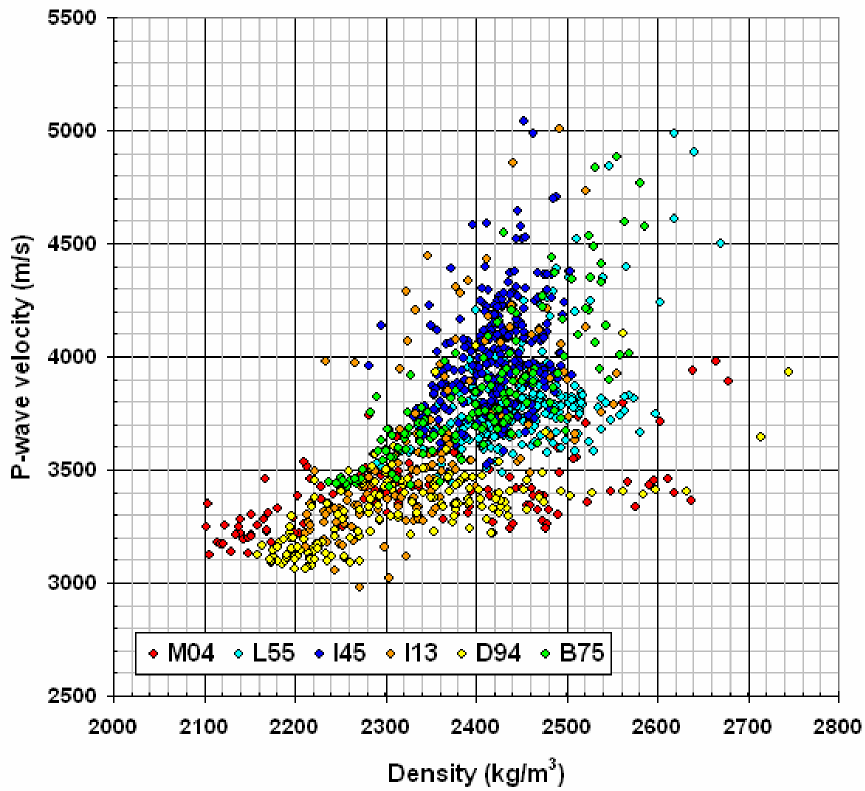

Figure 7-11: P-wave velocity versus density crossplot.

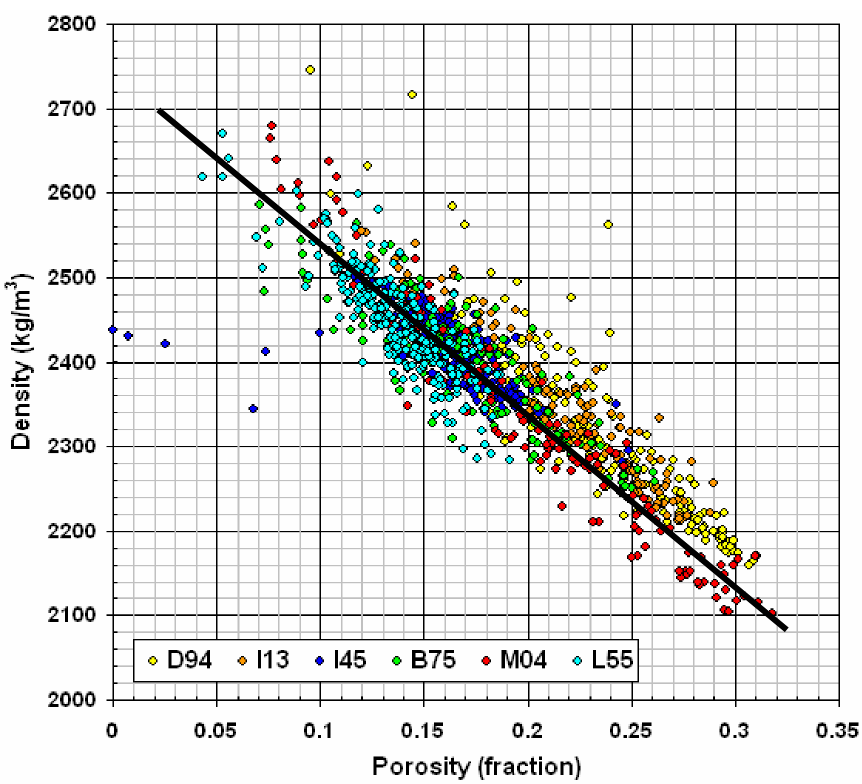

Figure 7-12: Density versus porosity crossplot.

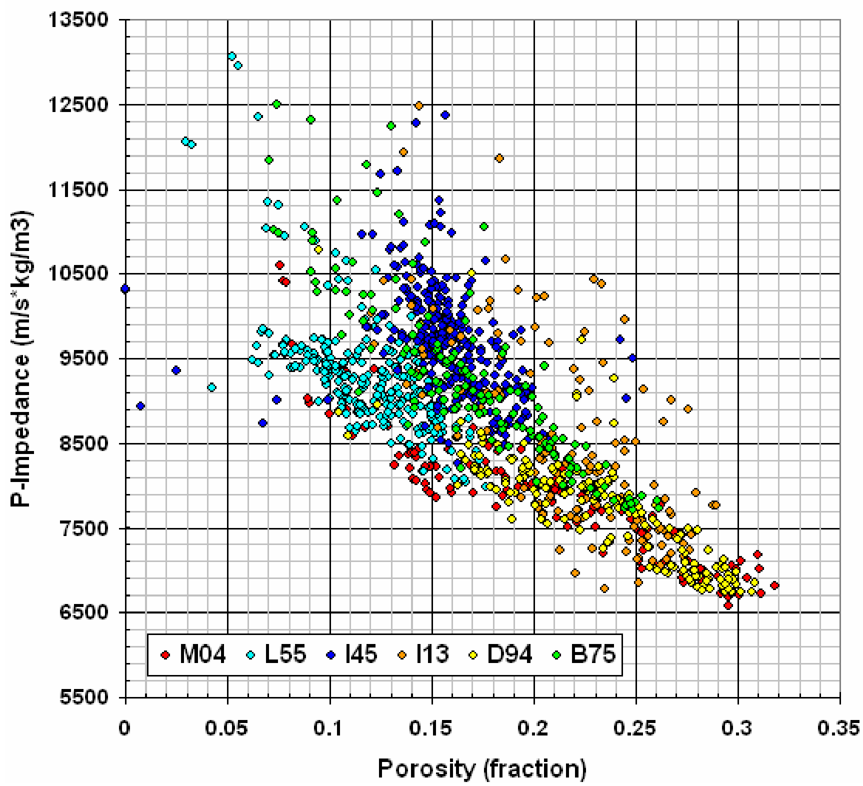


Figure 7-13: P-impedance versus porosity crossplot.

As mentioned the D-94, M-04, and L-55 wells are used in this analysis because of the presence of full waveform sonic data. These wells are crossplotted to observe if the shear wave data may assist in isolating the variable oil density values. The P-wave versus S-wave crossplot (Figure 7-14) shows a fairly constant trend ($V_S = 0.70V_P - 558.2$) through the Hebron asset. The $V_P/V_S$ ratio crossplot (Figure 7-15) shows a good separation between the wells in the D94 block (~20 API oil) compared the L-55 well (~31 API oil). The L-55 well also contains a gas cap, which accounts for the lowest $V_P/V_S$ values. The M-04 well has the cleanest sand whereas the L-55 sand is not as clean. The Lambda-Mu-Rho crossplot (Figure7-16) shows two clusters: one for the M-04 and D-94 wells and one for the L-55 well. This is because the deeper L55 Ben Nevis zone has increased mu*rho values due to the increased shear wave values. The L55 zones also has low lambda*rho values indicating the presence of a gas zone.

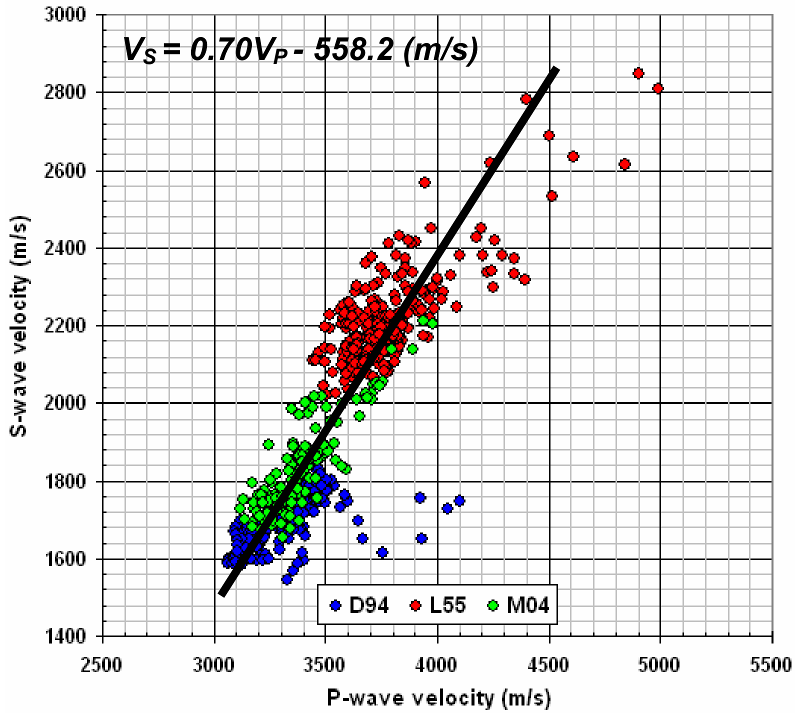


Figure 7-14: P-wave velocity versus S-wave crossplot.

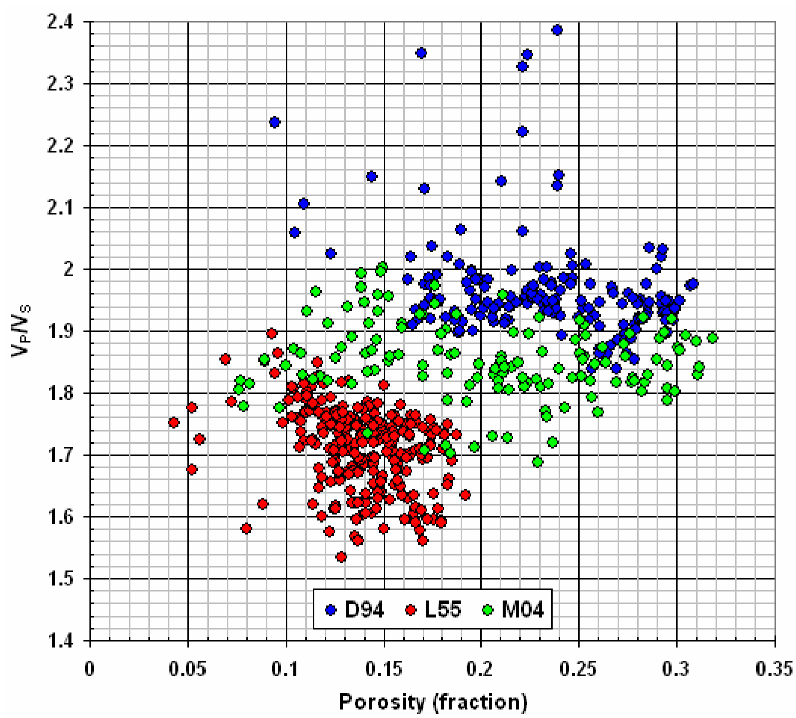


Figure 7-15: $V_P/V_S$ ratio versus porosity crossplot.

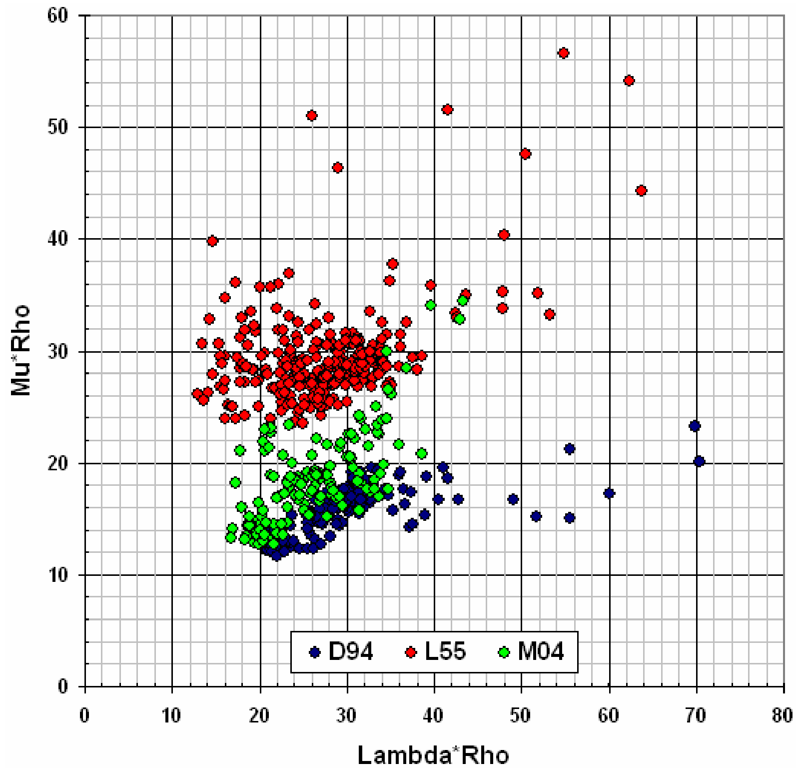

Figure 7-16: Lambda*Rho versus Mu*Rho crossplot.

### *7.4.2 Fluid Replacement Modelling*

In order to get an understanding of the rock property variations associated with the Ben Nevis zone, Fluid Replacement Modelling (FRM) was performed on the M-04 and L-55 wells. Fluid replacement or substitution modelling is an important aspect of seismic attribute work because it provides a useful tool for modelling and qualifying various fluid scenarios, which may produce an observed seismic amplitude response (Smith et al. 2003). The most common and practical method of fluid substitution is the low-frequency Gassmann theory (1951). The Gassmann equations calculate the effects of fluid substitution on seismic properties using rock frame properties. Batzle and Wang (1992) defined empirical relationships which estimate hydrocarbon bulk modulus (compressibility) and density based on reservoir temperature and pressure, oil and gas gravity, gas to oil ratio (GOR), and salinity. Table 7-1 shows the input reservoir parameters for the Batzle-Wang fluid modelling, and the input rock mineralogy is shown in Figure 7-17. New P-wave, S-wave, and density logs were output from the Fluid Replacement modelling for forward modelling.

| Ben Nevis Reservoir Parameters | Hebron | West Ben Nevis | Ben Nevis |
|---|---|---|---|
| Pressure (kPa) | 19,000 | 20,000 | 24,100 |
| Temperature (Celsius) | 62 | 70 | 82 |
| Salinity (Kppm) | 60 | 60 | 60 |
| Oil Gravity (API) | ***19 - 21*** | ***28*** | ***31*** |
| Gas/Oil Ratio ($m^3/m^3$) | ***50*** | ***90*** | ***117*** |
| Porosity (%) | ***23*** | ***18*** | ***15*** |
| Permeability (md) | 400 | 100 | 15 |
| Water Saturation (frac) | 0.24 | 0.35 | 0.45 |
| Oil / Water Contact (m) | -1900.7m | -1992m | -2442m |
| BOI | 1.1 | 1.3 | 1.3 |
| Oil Viscosity (cp) | 8.0 | 1.0 | 1.0 |

Table 7-1: Ben Nevis reservoir parameters.

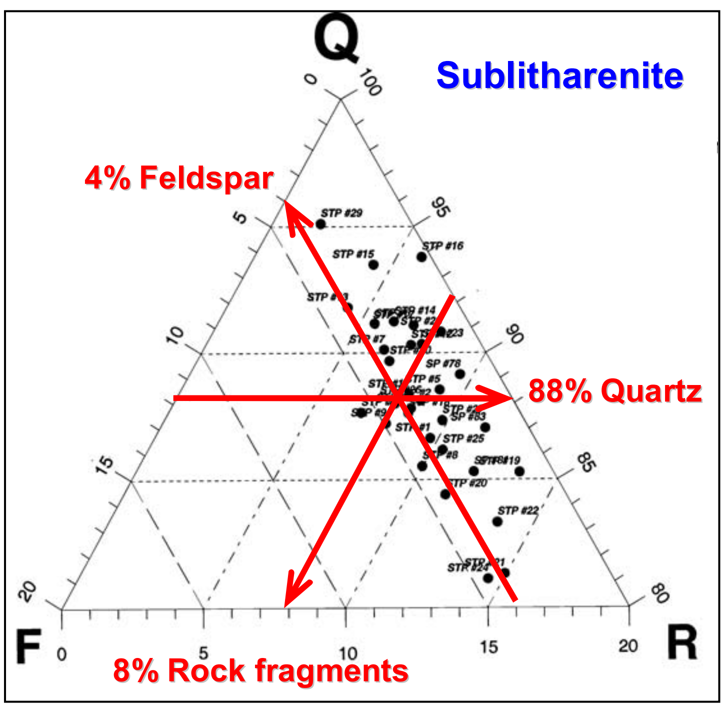


Figure 7-17. Ternary diagram for D-94 well location.

Batzle-Wang fluid modelling was done using the parameters for the D-94 Ben Nevis reservoir to observe the effects of temperature, pressure, and gas-oil-ratio (GOR) on density for various oil density values (Figures 7-18 to 7-20).

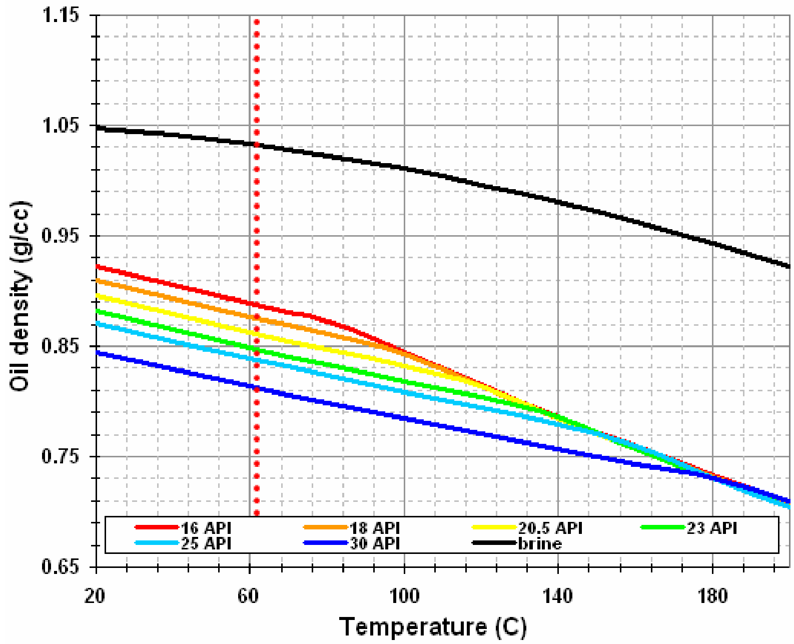


Figure 7-18: Density versus temperature plot.

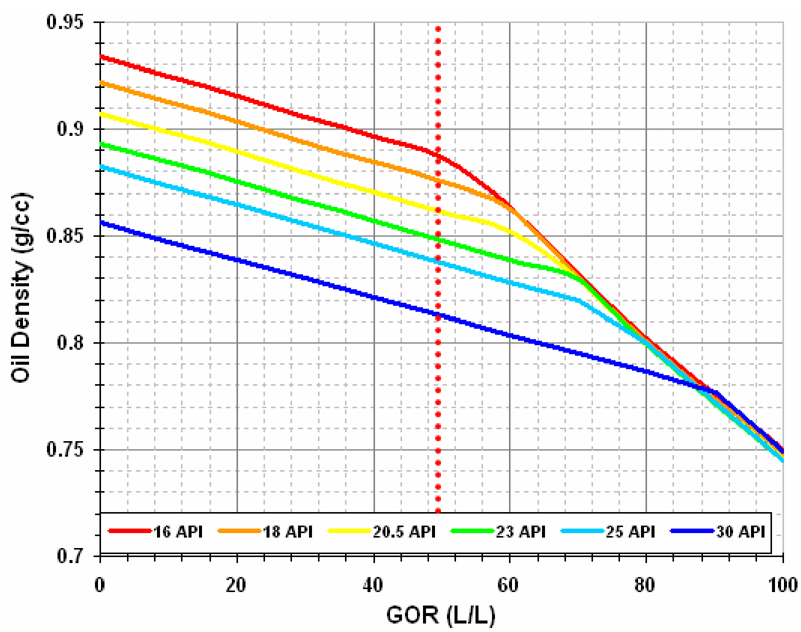


Figure 7-19: Density versus GOR plot.

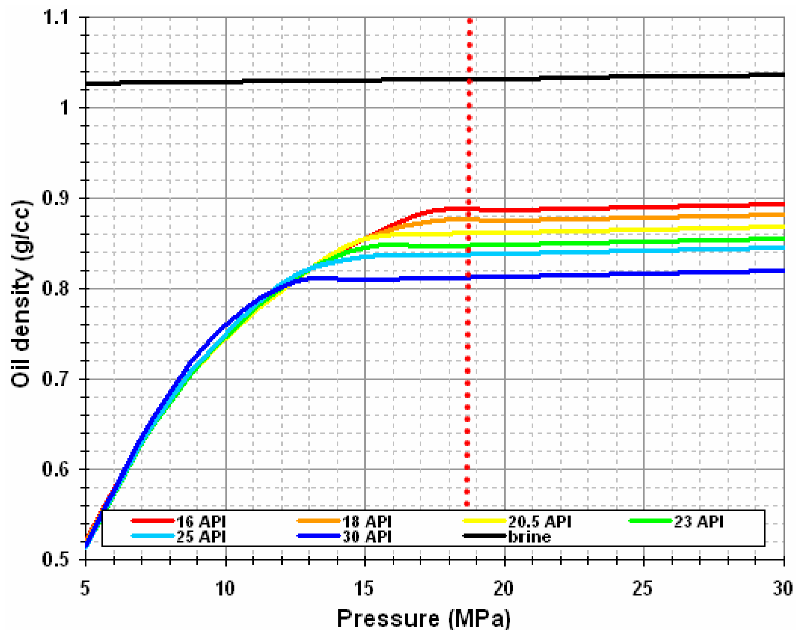


Figure 7-20: Density versus Pressure plot.

The dashed red line on each plot represents the values for the Ben Nevis reservoir. The constants are used from table 7-1. The various densities are showing separation at the reservoir values showing a dead oil scenario.

### *7.4.3 Synthetic modelling analysis*

AVO modelling volume approach was used to model the AVO response at the M04 and L55 well locations. Porosity and pore fluid were varied in the Ben Nevis zone using fluid replacement modelling. The porosity for the M04 well location is varied from 10 to 30 percent and the L55 well location is varied between 10 to 25 percent. The pore fluid constituent for both wells is varied between water, 20 API oil, 30 API oil, and gas. Once these volumes were attained, regular AVO analysis can be applied to the models. Figure 7-21 shows the M04 well location at 25% porosity and the varied pore fluid models. Figure 7-22 shows the L55 well location at 15% porosity and the varied pore fluid models.

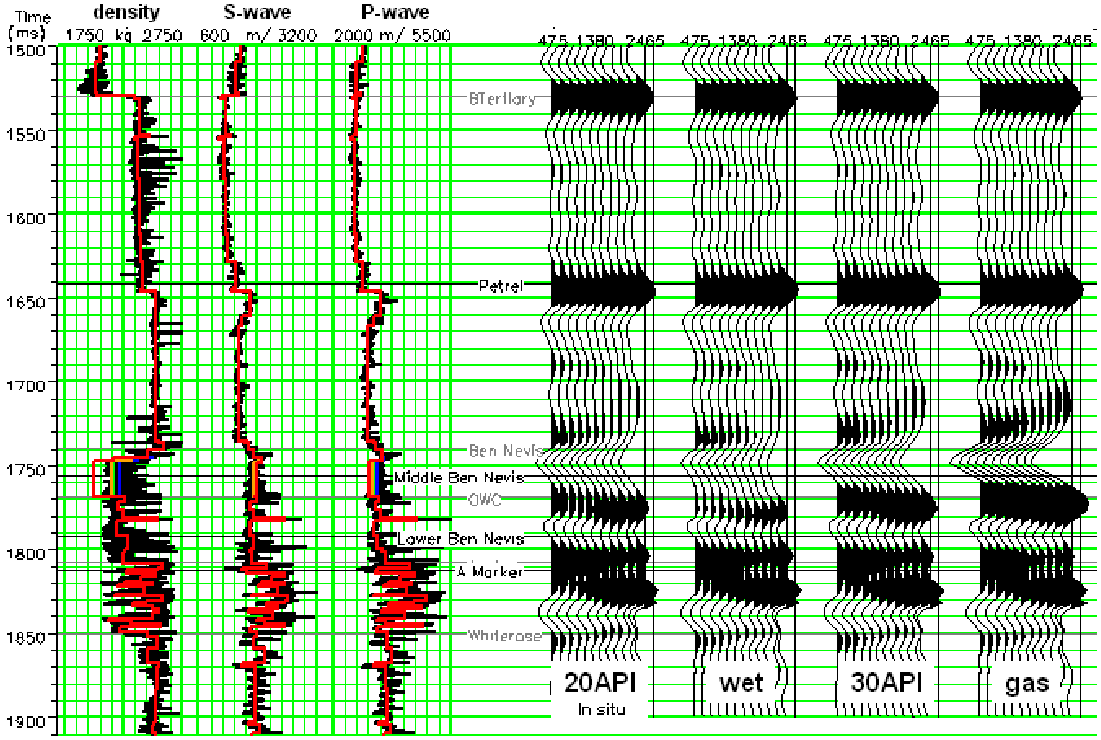


Figure 7-21: AVO modelling at M04 well location.

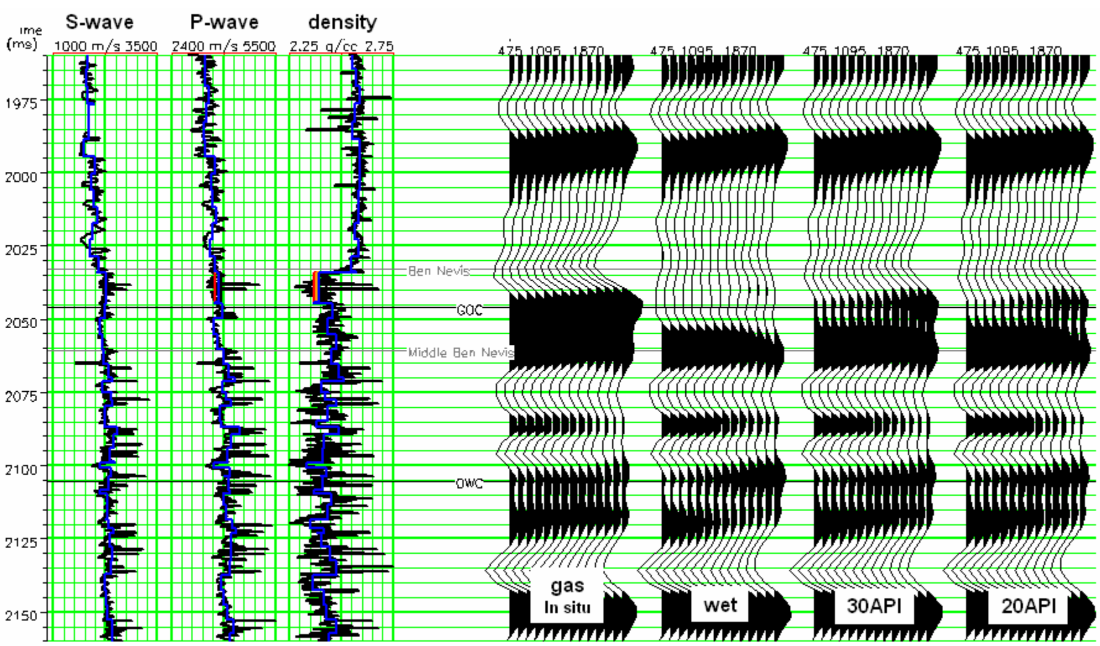


Figure 7-22: AVO modelling at L55 well location.

The top of the Ben Nevis zone of interest for the M04 well is at approximately 1750 ms and roughly 2030 ms for the L55 well. An AVO anomaly can be seen for the top and bottom of the zone of interest at both well locations. Pore fluid and porosity variations have a strong affect on the AVO response. The amplitudes for the top of the Ben Nevis zone are plotted versus offset showing the variations due to changes in porosity and pore fluid composition. This is shown in Figure 7-23 for the M04 well and Figure 7-24 for the L55 well location.

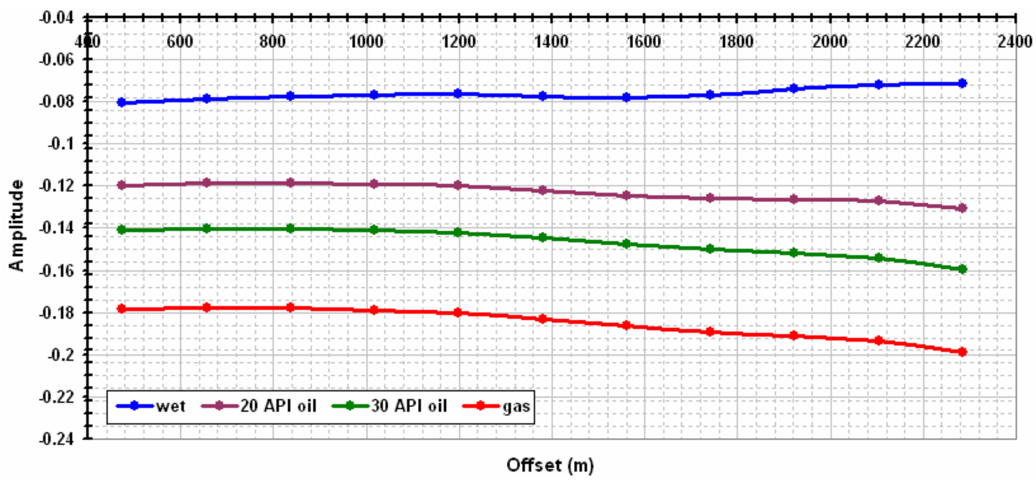


Figure 7-23: Amplitude versus offset plot at M04 location for 20% porosity.

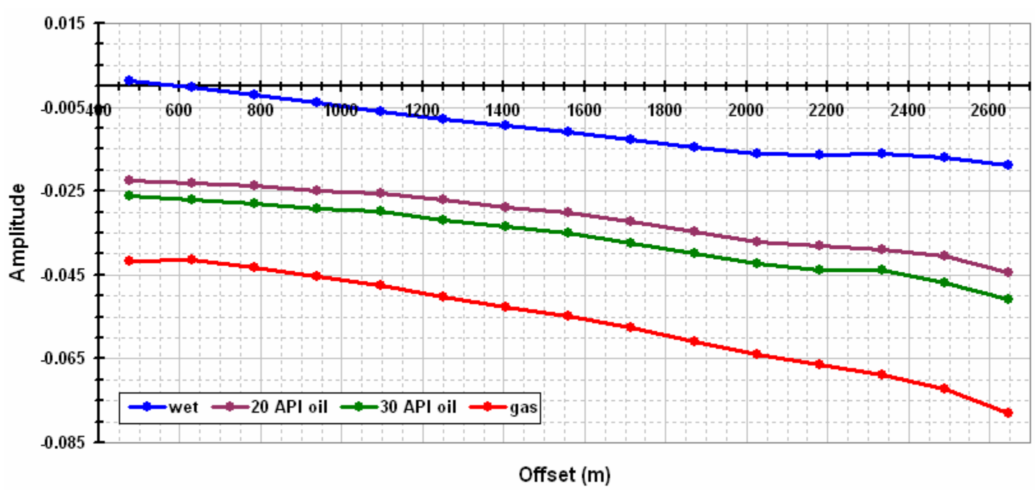


Figure 7-24: Amplitude versus offset plot at L55 location for 15% porosity.

The M04 amplitude versus offset plot (Figure 7-23) shows a class III type AVO anomaly for the oil and gas pore fluid cases, while the wet case does not show any AVO anomaly. The L55 amplitude versus offset plot (Figure 7-24) shows a class III type AVO anomaly for the wet, oil, and gas pore fluid cases. The separation between the 30 API and 20 API cases are fairly similar.

Crossplotting of intercept (A) and gradient (B) data provides useful insight on the nature of the pore fluid. In an intercept versus gradient crossplot brine filled sandstones and shales should fall on a well-defined "background-trend". The gradient and intercept volumes are crossplotted to compare the effects of the varying pore fluid and porosity, the crossplot for the M04 well is shown in Figure 7-25 and the L55 well in Figure 7-26.

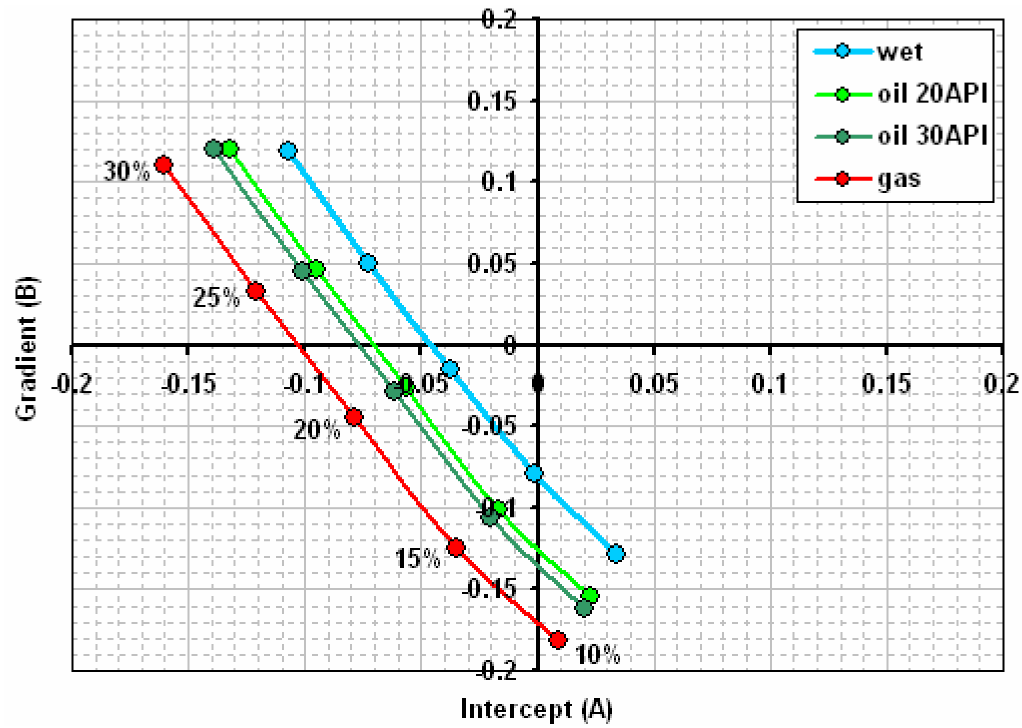


Figure 7-25: Intercept versus gradient crossplot showing trends for varying porosity and pore fluid for M04 well location.

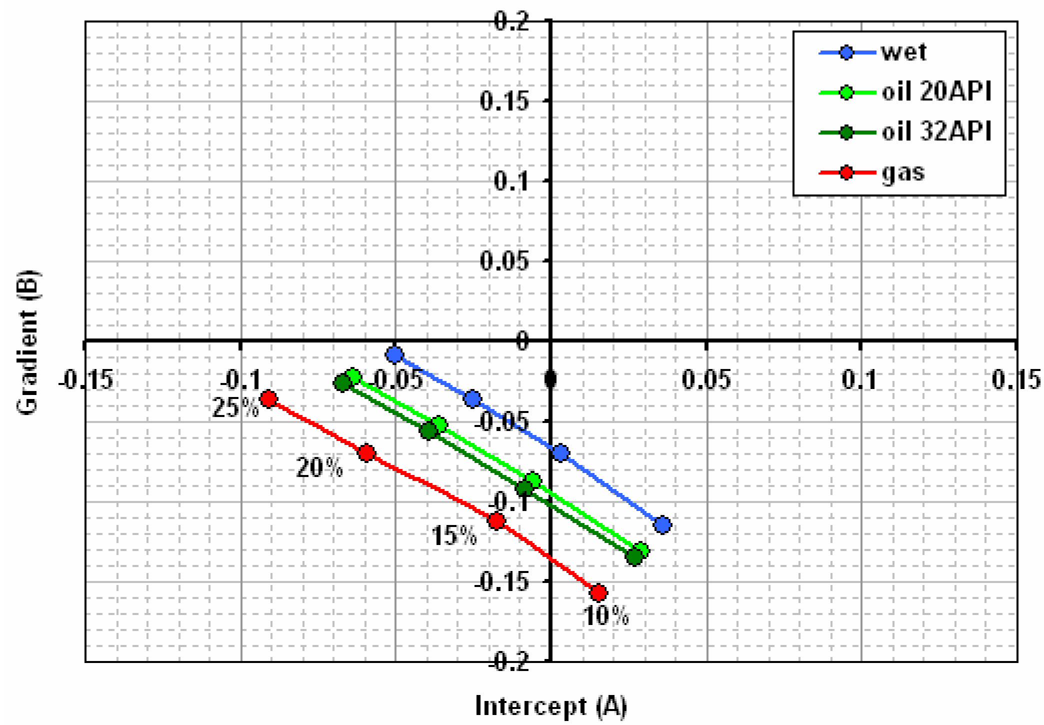


Figure 7-26: Intercept versus gradient crossplot showing trends for varying porosity and pore fluid for L55 well location.

On these crossplots, it can be observed that with increasing porosity the anomalous points for the top of the oil zone move from a class II type AVO anomaly towards a class IV type AVO anomaly. The pore fluid separates perpendicular to the background trend called the 'fluid vector'.

### *7.5 AVO ANALYSIS*

In this analysis a subset of the 3D volume covering the Hebron asset was pre-stack migrated in preparation for AVO analysis. The key horizon markers used for this analysis were provided by ChevronTexaco and Petro-Canada. The horizons used were the Petrel marker, top Ben Nevis, A-marker, and the B-marker. These horizons were used to constrain a velocity model for ray tracing, an initial low frequency model for post-stack inversion, and map generation of the extracted attribute volumes. The top Ben Nevis time structure map for the entire 3D survey is shown in Figure 7-27. This also shows the location of the cross section in Figure 7-2 and the dimensions of the pre-stack migrated volume.

Initially, all the wells on the 3D volume were correlated using extracted statistical wavelets. Each wavelet was extracted on a 20 by 20 trace region surrounding the well location and a time window encompassing the well length. As mentioned, these wells were then used to create a velocity model. This velocity model was used to ray trace the CDP gathers to achieve angle gathers for input into the AVO analysis.

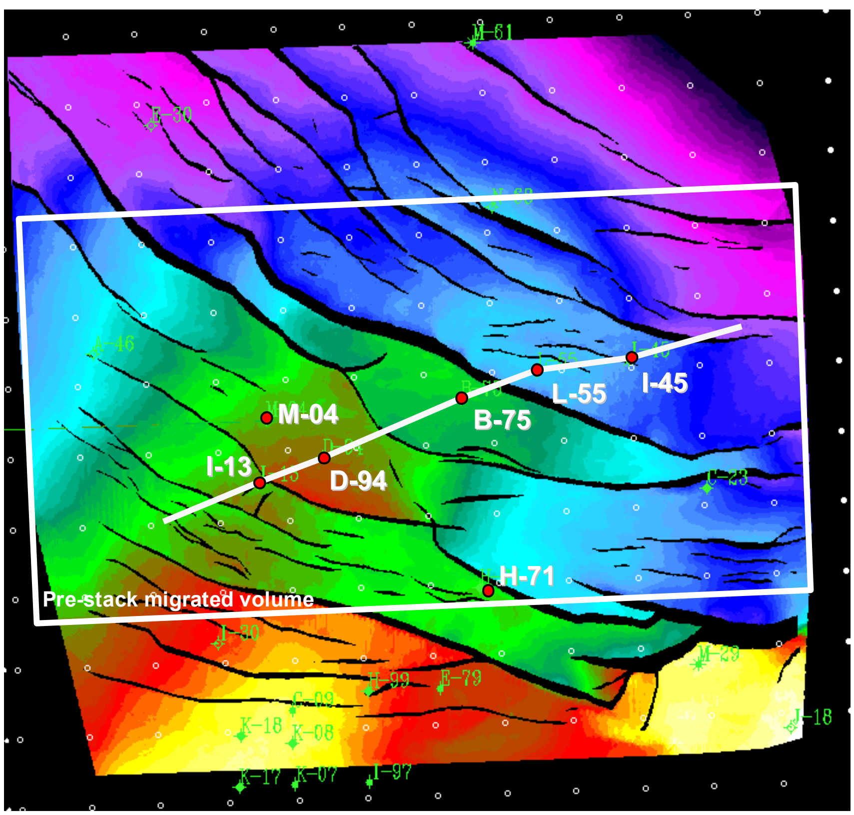


Figure 7-27: Top Ben Nevis time structure map.

The reservoir quality in the Ben Nevis degrades from the higher regions in the west to the deeper regions in the east. The porosity decreases with depth and the P-wave velocity and density increase with depth. This also may influence the AVO response at the Ben Nevis zone. Ultimately, a method to extract the pore fluid information with the varying reservoir conditions is desired.

Prior to the application of the two- and three-term AVO approximations the response of the reflection coefficients with varying offset at the top of the zone of interest was investigated. This is shown in Figure 7-28 comparing the approximations used in this study. The black line represents the response of the exact Zoeppritz equations; the approximations are compared to this result for accuracy. The Shuey approximation is accurate to about 32 – 35 degrees. The Aki-Richards two-term approximation is accurate to about the same as the Shuey. The Aki-Richards three-term approximation almost overlays the exact Zoeppritz to about 60 degrees. It can be said for this study that the Shuey (two-term) approximation is good from approximately 30 - 35 degrees and the Aki-Richards (three-term) approximation can be theoretically used to 60 degrees. The second term (B) of the Aki-Richards contributes to about 32 degrees and the third term (C) from 32 – 80 degrees. The two term Fatti et al. approximation contributes to about 36 degrees before it starts deviating from the Zoeppritz values. These values are taken into account when extracting the AVO attributes.

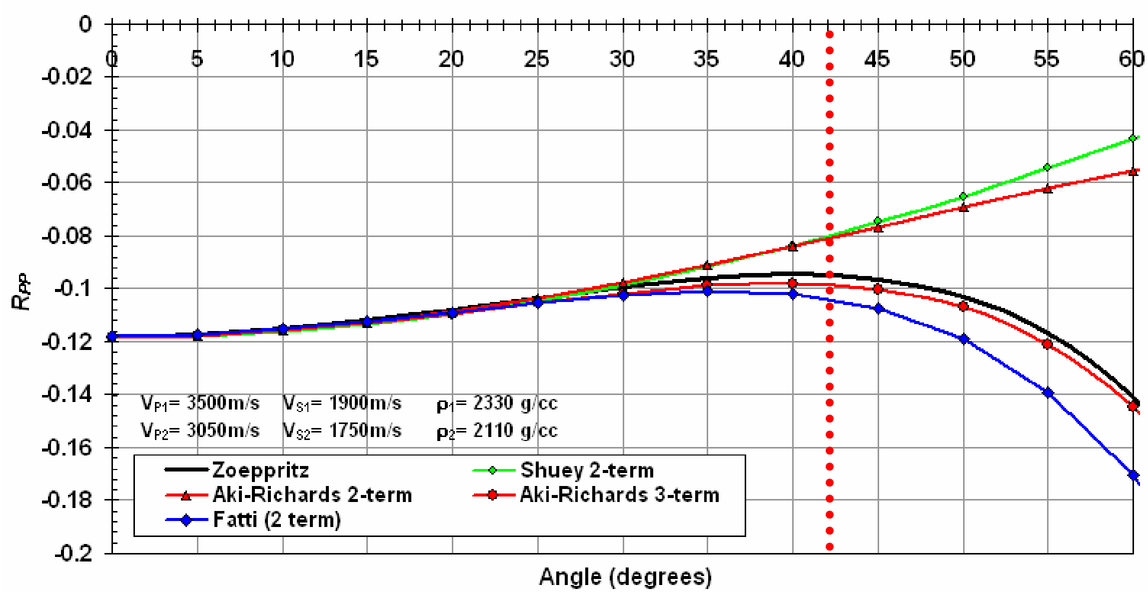


Figure 7-28: Comparison of approximations to the exact Zoeppritz at the top of the zone of interest.

### *7.5.1 Intercept and Gradient analysis*

Intercept *(A)* and gradient *(B)* volumes were created using Shuey's approximation of the Zoeppritz equations. The intercept attribute represents the theoretical zero-offset response. This will show amplitude effects such as "bright spots" but will not show any AVO effects. The gradient attribute shows the rate of change of the amplitudes on the CDP gather at each time sample as a function of angle incidence. This attribute should show the entire AVO effect.

A time slice taken through the top of the Ben Nevis zone was created and is shown in Figure 7-29. A distinct AVO anomaly can be seen across the whole asset. The anomaly is strongest in the B75 block followed by the D94 block. The L55 block shows a weak response, indicating the poorer reservoir quality compared to the others. The I13 well also shows a weak AVO response again degraded reservoir quality. These responses are expected - as mentioned the D94 block has the best reservoir quality but has 17 to 22 API oil. The B75 block has the second best quality and the oil is lighter (~28 API), whereas the L55 block has poor reservoir quality with 31 API oil and a gas cap. The Ben Nevis zone in the L55 block is also 500 meters deeper than the other Ben Nevis zones. The porosity and permeability values are also greatly reduced. The I13 well also has higher-density oil (~18-21 API) with a reduced porosity compared to the D94 block. A strong AVO anomaly up-dip in B75 block probably indicates the presence of a gas cap.

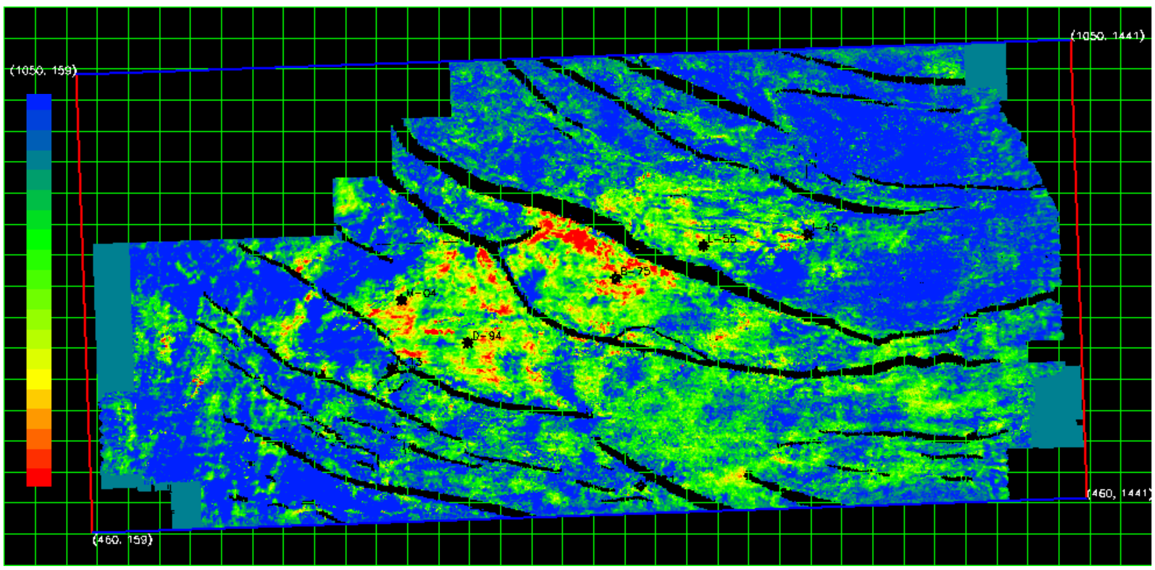

Figure 7-29: Gradient event slice at the top Ben Nevis horizon.

Crossplotting of intercept (A) and gradient (B) data provides useful insight on the nature of the pore fluid. In an intercept versus gradient crossplot, brine-filled sandstones and shales should fall on a well-defined "background-trend". Outliers from this background trend may possibly indicate accumulations of hydrocarbons or lithologies with anomalous rock properties.

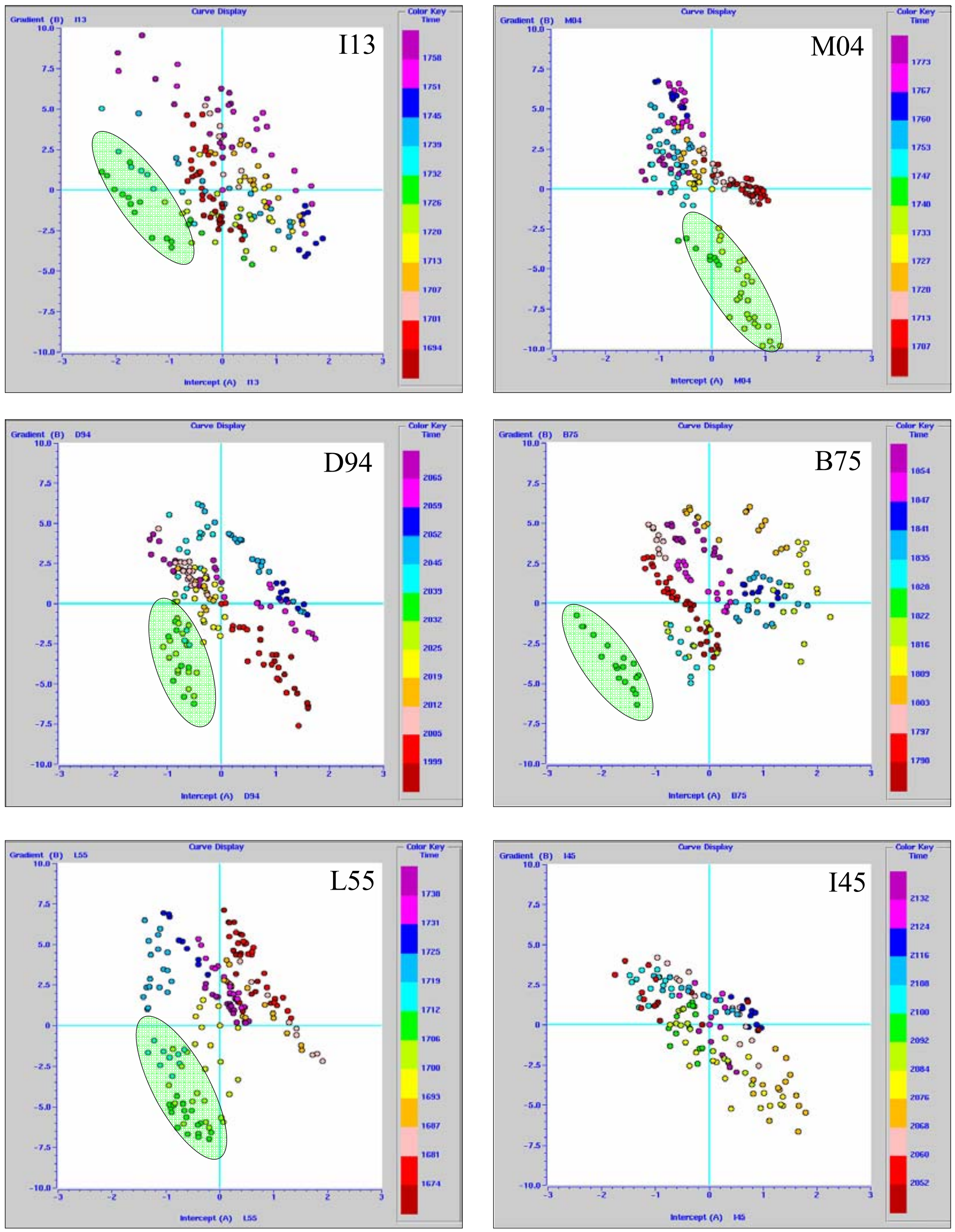


Figure 7-30: Intercept versus gradient crossplots at well locations on Hebron asset.

The gradient and intercept volumes are crossplotted at each well location to compare the effects of the varying oil density across the asset. A 3 by 3 trace volume around the well is crossplotted with an 80 ms window centered on the

Ben Nevis pick. These plots are shown in Figure 7-30. The top of the Ben Nevis zone is highlighted by the green ovals. All of the crossplots show deviations from the background trend with the exception of the I45 well. The I45 crossplot shows no anomalies and therefore represents a good background trend for comparison. A direct comparison of the anomalous zones is shown in Figure 7-31.

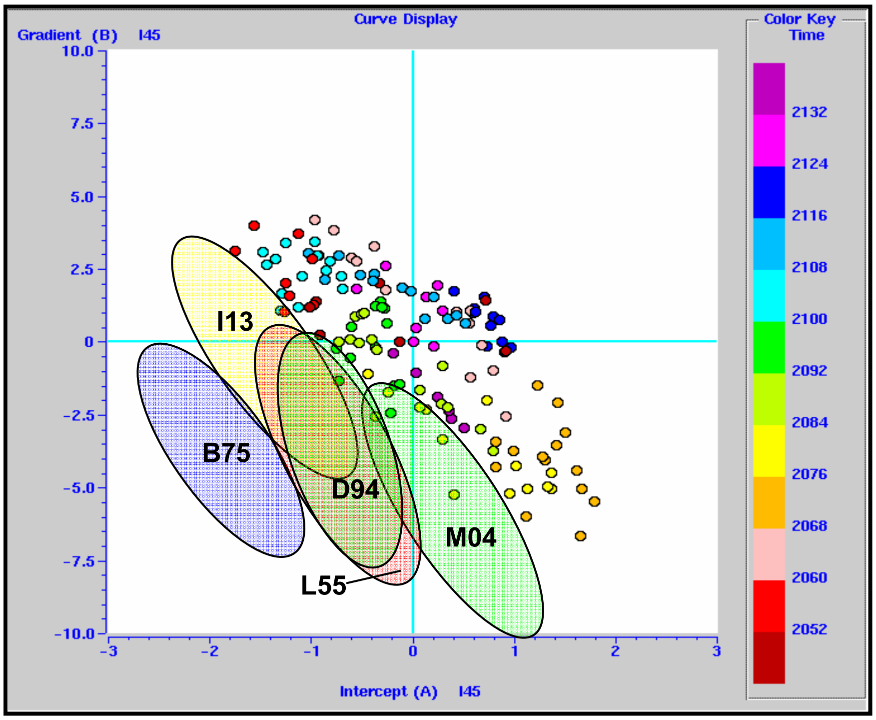


Figure 7-31: Intercept versus gradient crossplot showing anomalous zones.

The B75 well isolates the best; the I13, D94, and L55 wells overlap. This shows a distinct difference between the wells in the D94 block (17-21 API) to the B75 block (~28API). The L55 block may not be differentiable using Intercept and Gradient attributes. Since the quality of the L55 block reservoir is degraded the attributes may be only showing the gas cap. This is also supported by the fact that the I45 well does not have a gas cap and does not show a crossplot anomaly.

### *7.5.2 Fluid factor analysis*

Encouraged by the positive results obtained with the gradient and intercept volumes, P- and S-reflectivity volumes were extracted from the data in order to attain a fluid factor volume. The fluid factor volume is calculated to be low amplitude for all reflectors in a clastic sedimentary sequence except for rocks that lie off the "mudrock line". The "*mudrock line*" is the trend on a crossplot of $V_P$ vs. $V_S$ on which water-saturated sandstones, shales, and siltstones lie. If shear information is not available a global empirical relationship derived by Castagna et al. (1985), called the ARCO mudrock equation, provides $V_S$. For this data set P-wave and S-wave sonic logs were acquired at the well location. From this log information a local *mudrock* relationship was derived which was in turn used to create the fluid factor AVO attribute.

A time slice taken through the top of the Ben Nevis zone is shown in Figure 7-32. Again a distinct AVO anomaly can be seen across the whole asset. The fluid factor volume shows a better, more consistent anomaly across the asset. The bounds of the anomaly are somewhat consistent with, and may represent, the oil-water-contact. An AVO anomaly can be seen down dip in the D94 block.

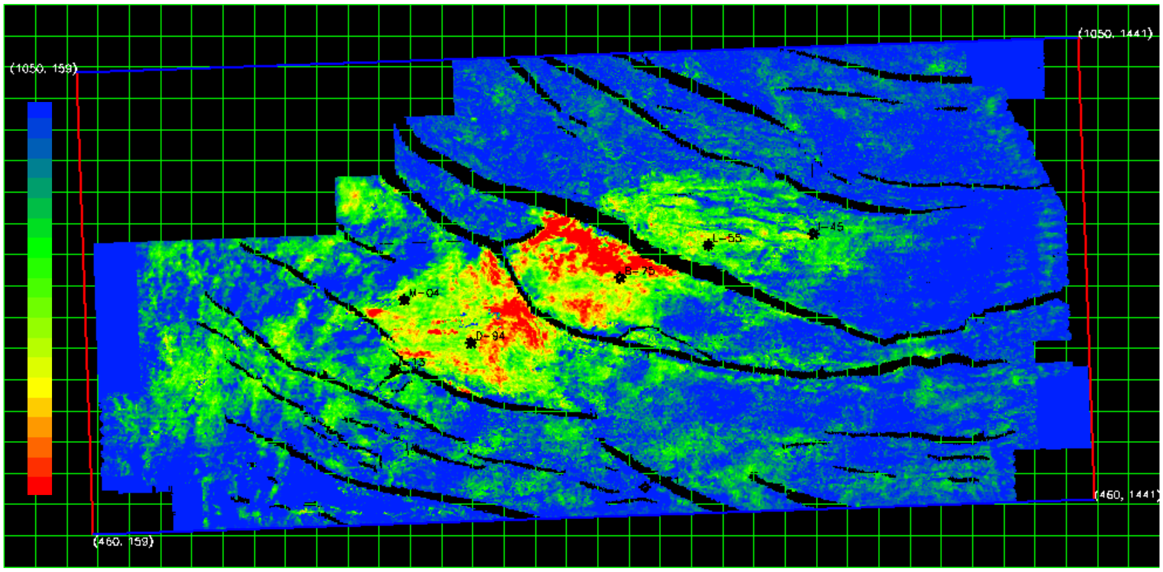

Figure 7-32: Fluid factor time slice at the top Ben Nevis horizon.

Crossplotting of P-reflectivity and S-reflectivity data is undertaken at each well location in an attempt to isolate the nature of the pore fluid. These crossplots are shown in Figure 7-33. Again, all the wells show isolated anomalous zones, with the exception of the I45 well. A direct comparison is shown in Figure 7-34 with all the anomalous zones plotted on the I45 crossplot. The B75 location separates the best, followed by the other well locations. This may be indicative of the changing fluid density values in the reservoir. The L55 well is indistinguishable from the D94 wells, as seen on the Intercept versus Gradient crossplots. This is most likely due to the reservoir depth and the reservoir conditions compared to the shallower Ben Nevis zones.

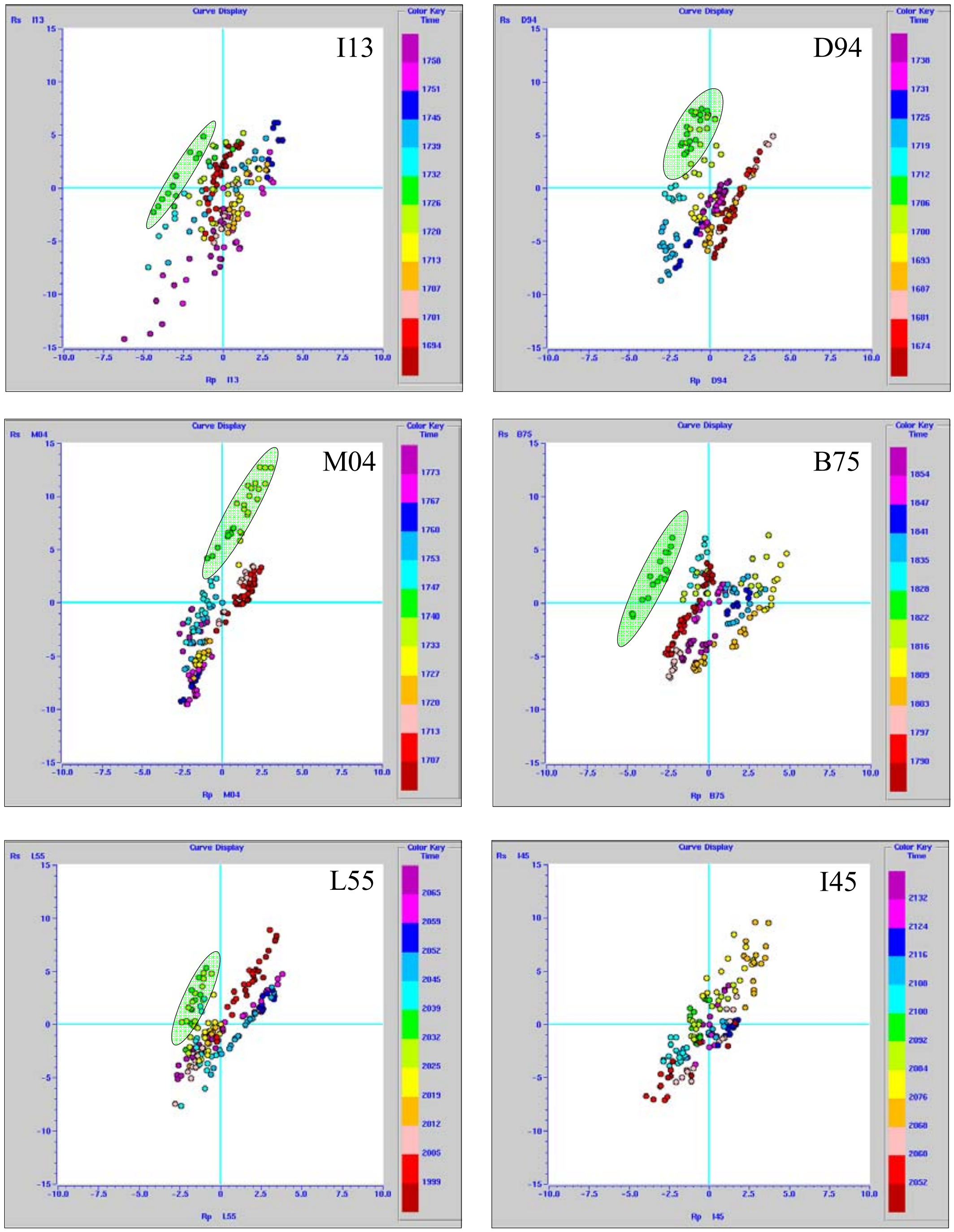


Figure 7-33: P-reflectivity versus S-reflectivity (Fluid factor) crossplots at well locations on the Hebron asset.

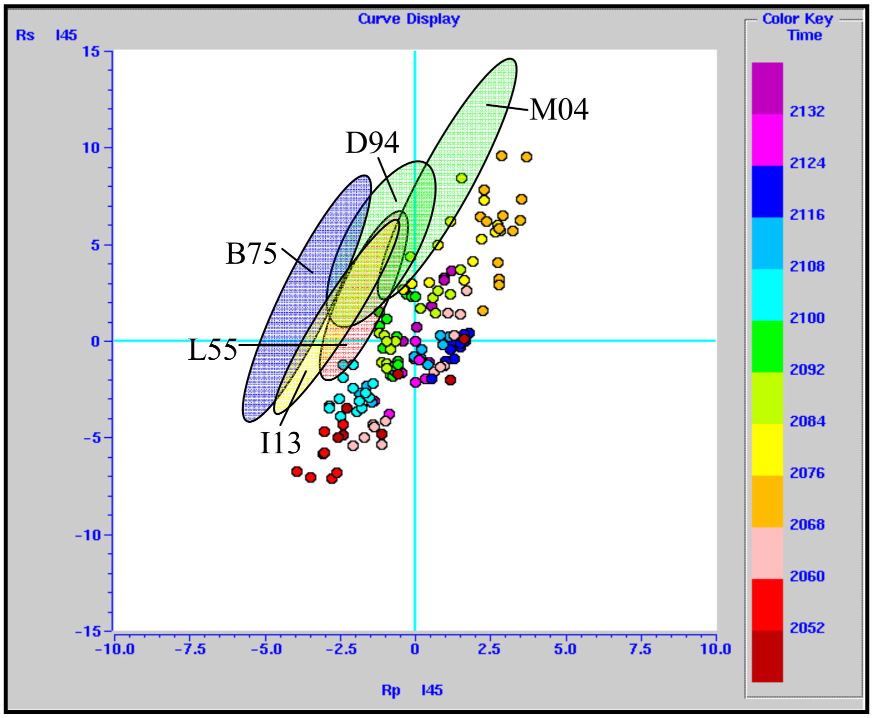


Figure 7-34: P-reflectivity versus S-reflectivity crossplot showing anomalous zones.

### *7.5.3 Three-term AVO analysis*

A three-parameter AVO extraction was utilized in an attempt to detect density variations for the six volumes. Intercept (A), gradient (B), and curvature (C) are the outputs of this extraction. The intercept and gradient terms should be similar to those extracted from the two-term AVO equation. Once A, B, and C attributes are acquired, they are arranged to get P-wave velocity reflectivity ($\Delta V_P/V_P$), S-wave velocity reflectivity ($\Delta V_S/V_S$), and density reflectivity ($\Delta\rho/\rho$). The time slice at the top of the Ben Nevis reservoir of the density reflectivity volume is shown in Figure 7-35.

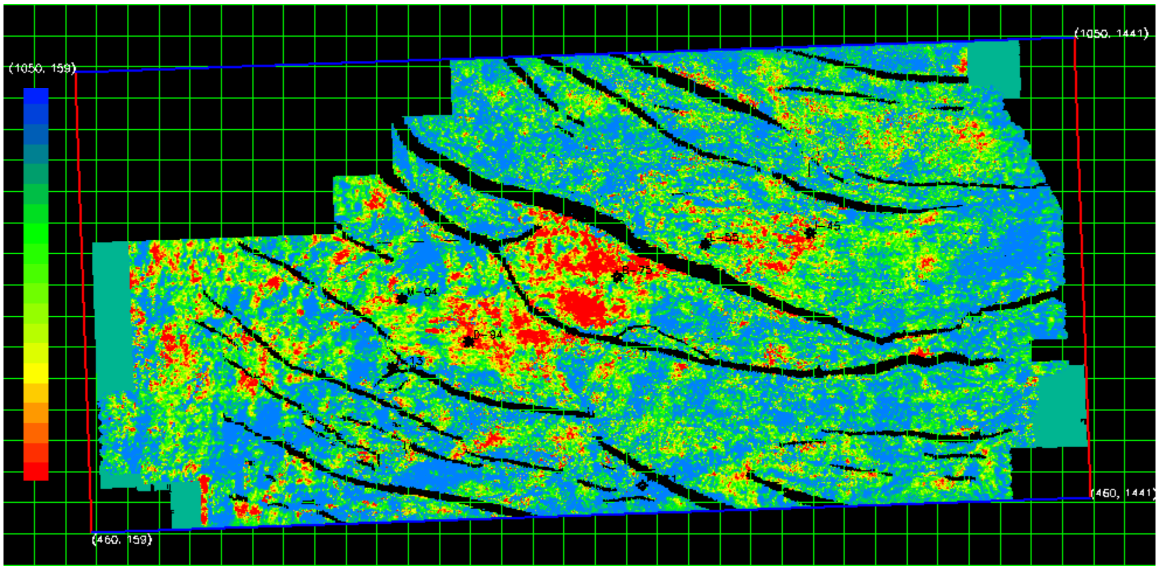

Figure 7-35: Density reflectivity time slice at the top Ben Nevis horizon.

The density reflectivity volume shows variations across the asset. The extreme “darks” represents positive variations and the “hots” represent negative variations. The strongest density contrasts are associated with the D94 and B75 blocks. The L55 block shows weak values in comparison. The values in the B75 block are the strongest and again may indicated the presence of lighter gravity oil in comparison to the D94 block.

### *7.6 Inversion Analysis*

The *Jason Rocktrace* method is used to simultaneously invert for density, S-wave, and P-wave impedances as described in chapter 5. The inputs for Jason inversion procedure are the P-impedance, S-impedance, and density logs in time, range limited stacks, and interpreted horizons. The input horizons and logs are used to create an ‘earth model’, which constrains the inversion process. The input earth models are shown in Figure 7-36. Three range-limited volumes were input for this analysis: near (10 - 20 degrees), mid (20 - 30 degrees), and far (30 - 40 degrees). These are used to extract the reflectivities used for the inversion.

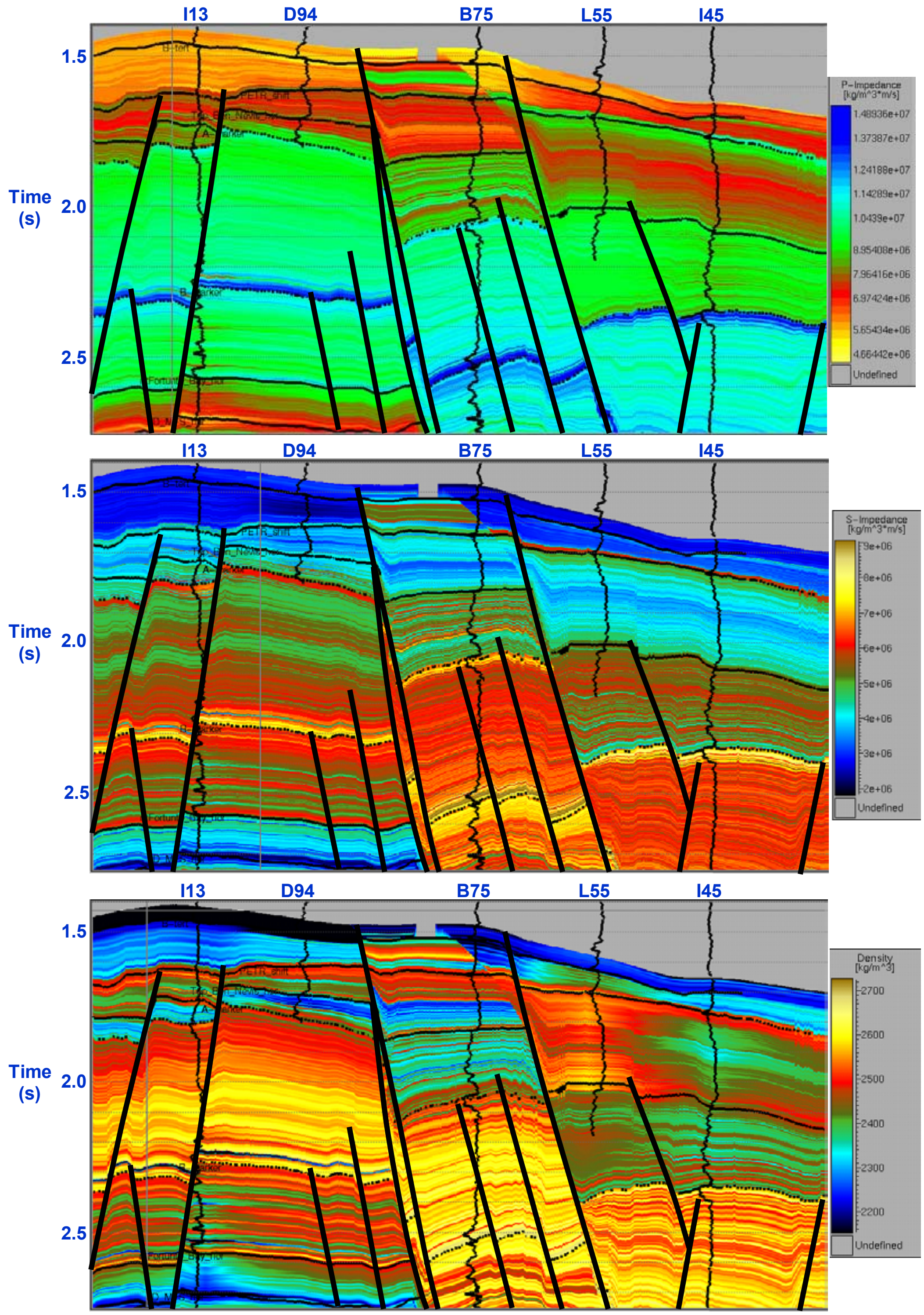


Figure 7-36: P-wave, S-wave, and density impedance earth models.

An important part of the inversion procedure is the extraction of wavelets at the well locations prior to inversion. For the simultaneous inversion approach, wavelets must be extracted for the near, mid, and far volumes. Wavelets are extracted at each well location for the three volumes. The best wavelets are then averaged for each volume. Figure 7-37 shows the extracted wavelets for all the wells and the final wavelets used in the inversion process.

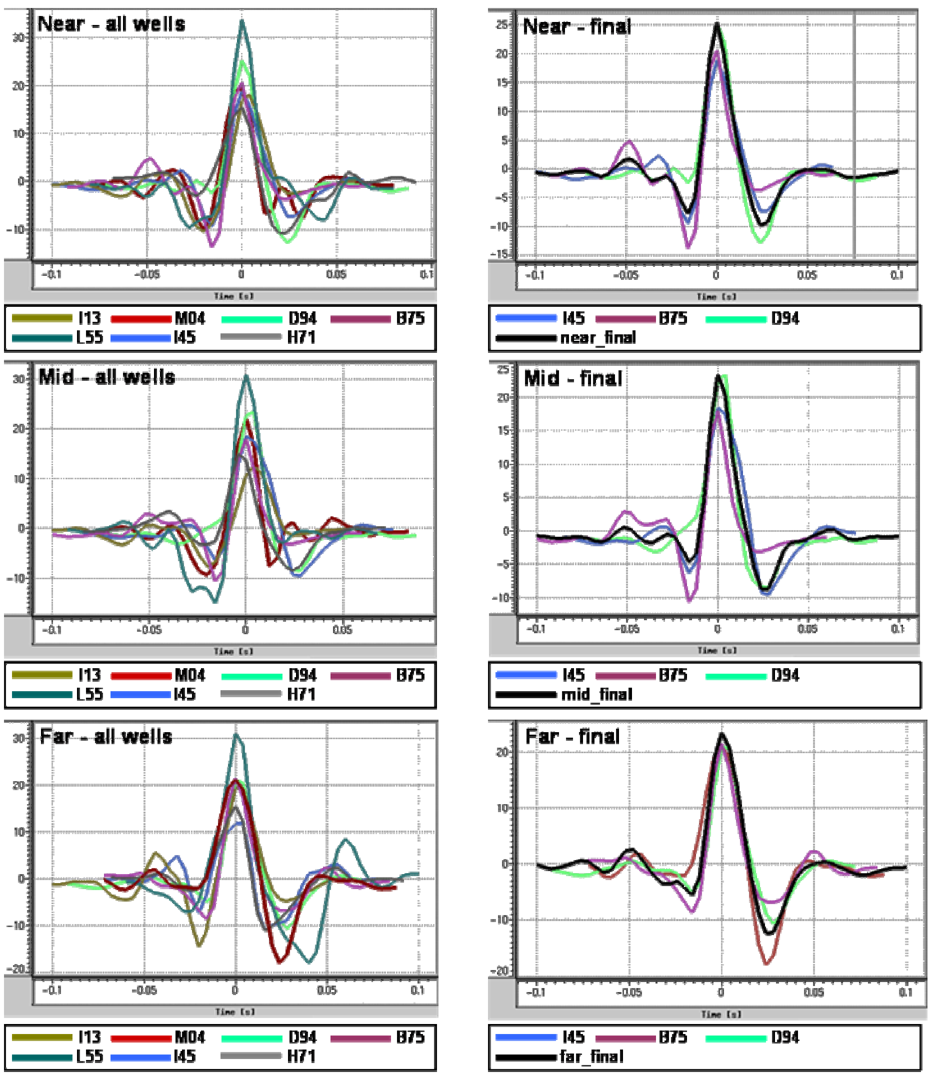


Figure 7-37: Near, mid, and far wavelets used for inversion.

Before inversion performed an appropriate lambda value must be chosen. The lambda factor is used to control the balancing of the misfit norms. A low lambda factor results in an acoustic impedance trace, which has few sharp contrasts and little detail. High lambda results in detailed acoustic impedance trace values. Figure 7-38 varies the lambda factor with certain properties helping the user choose the appropriate value.

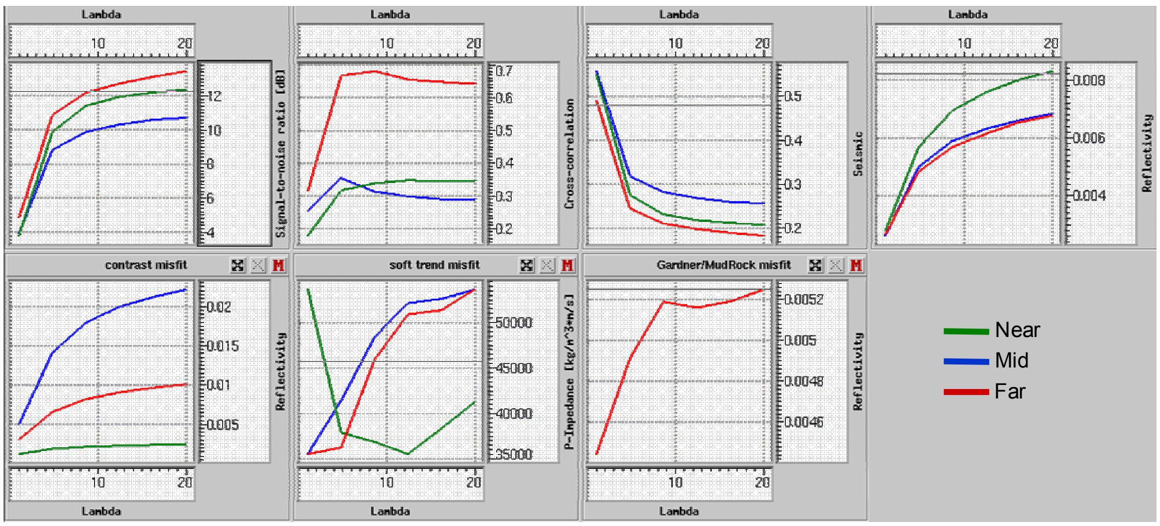


Figure 7-38: Lambda factor quality control plot.

From the lambda factor quality control plot a value of 10 was identified to be optimal for the inversion. Soft constraints were also used to guide the inversion process. The main one used was the Gardner relationship as a constraint on the density inversion. These constraints were set to impose a range of physically meaningful values on the inversion output. Once all the required inputs and parameters were set the Constrained sparse spike inversion was run. Figure 7-39 shows the output P-wave, S-wave, and density impedance volumes.

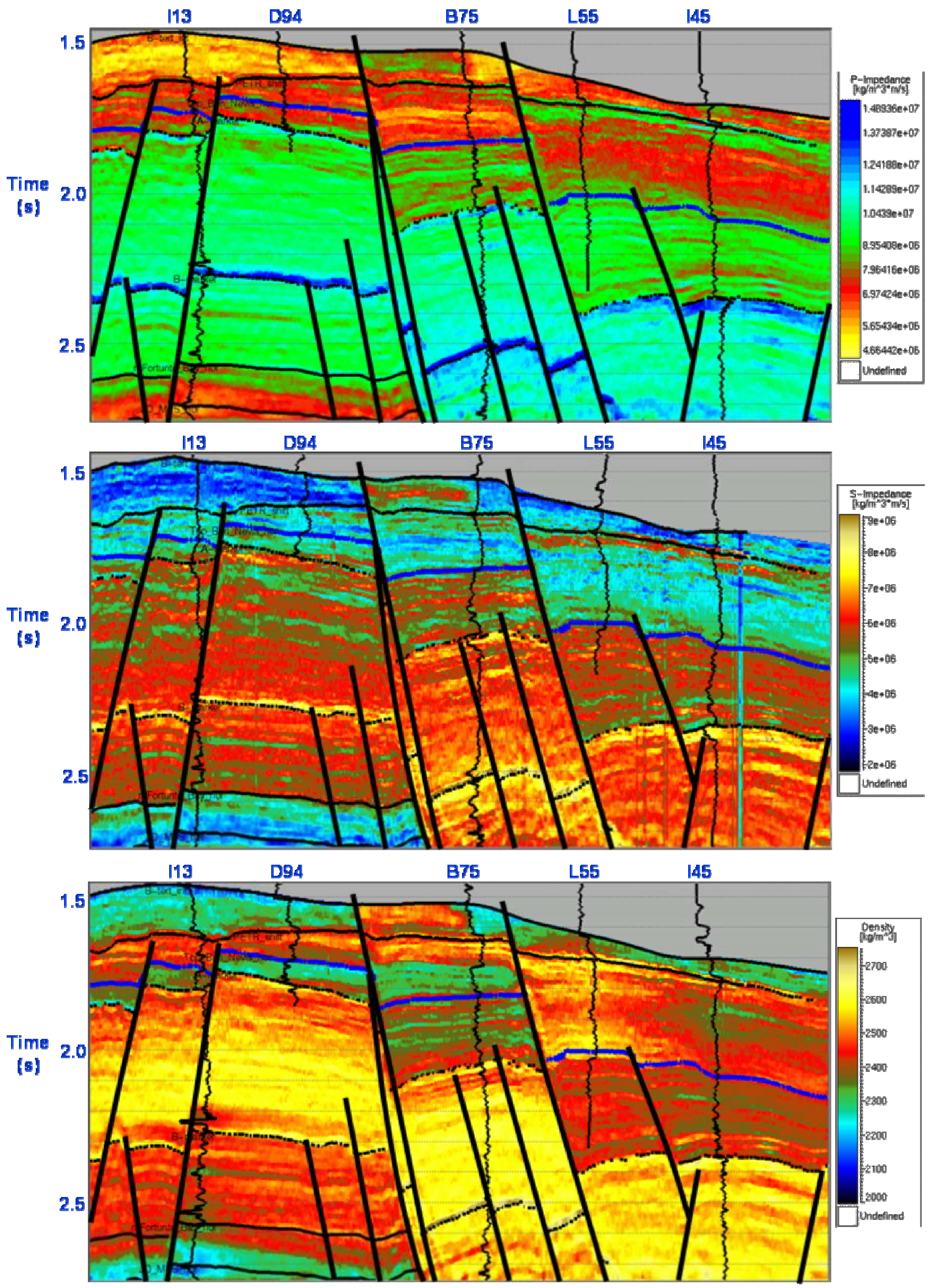


Figure 7-39: P-wave, S-wave, and density impedance sections through wells.

The top of the Ben Nevis zone is denoted by the blue horizon. On each impedance section the respective logs are overlaid for direct comparison. The

Jason CSSI inversion does not force the inversion to match the wells. It only requires the result to lie within the defined constraints. Event slices are created from the top of the Ben Nevis horizon with an average window of 12 ms below. The P-impedance slice is shown in figure 7-40, S-impedance in Figure 7-41, and density in Figure 7-42.

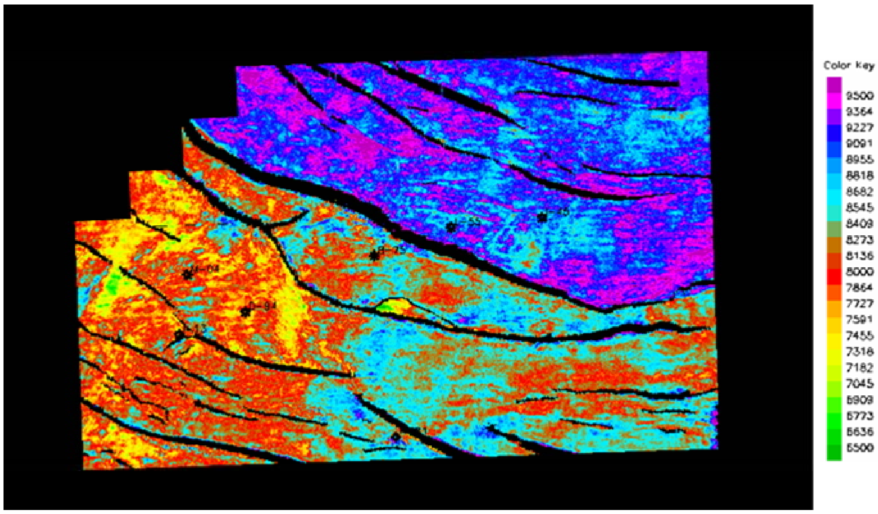


Figure 7-40: P-impedance slice at Ben Nevis zone.

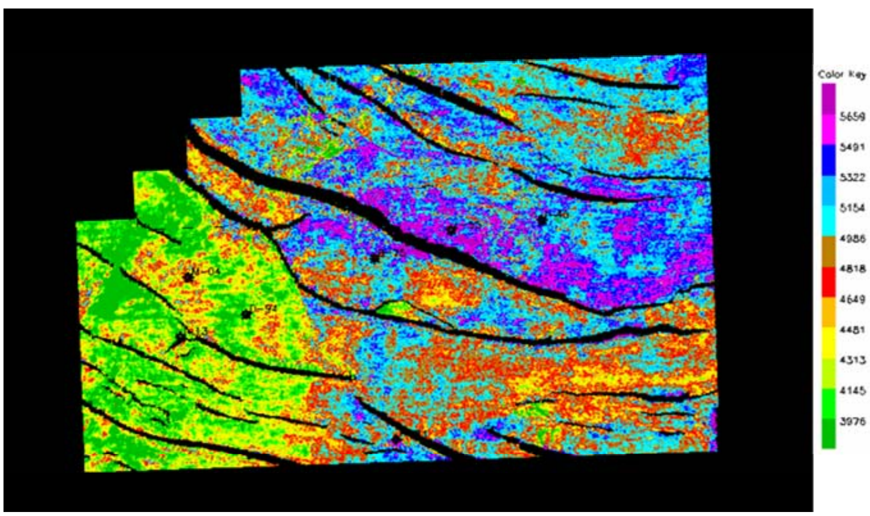


Figure 7-41: S-impedance slice at Ben Nevis zone.

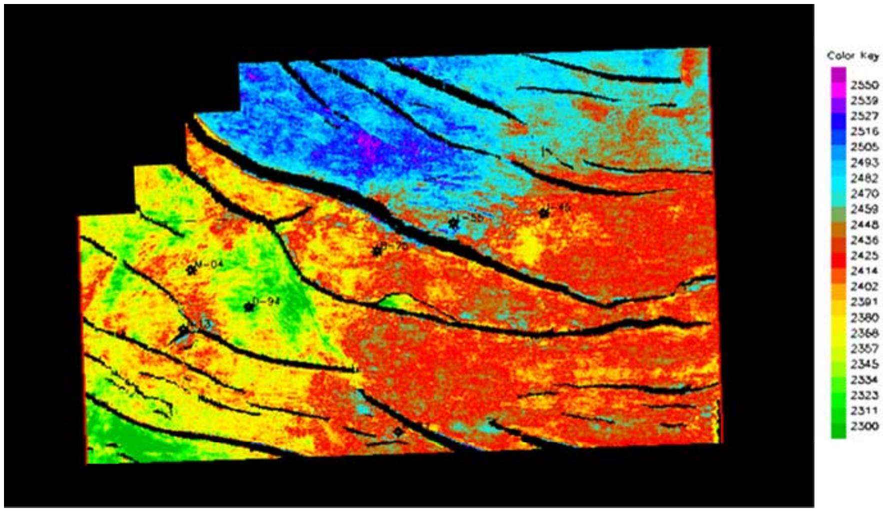


Figure 7-42: Density slice at top of Ben Nevis zone.

The P-impedance slice shows low impedance values in the Hebron fault block, moderate values in the West Ben Nevis block, and higher values in the Ben Nevis block. This is expected due the depth differences across the asset. The S-impedance slice shows an interesting trend between the Hebron fault block and the rest of the asset. This can represent the edge of the depositional shoreface deposits. The best Ben Nevis zones with the best net-to-gross values are in the Hebron fault block. The density slice has lowest values in the Hebron block with similar values in the Ben Nevis and West Ben Nevis blocks. As seen in Figure 7-12, the density has a good relationship with porosity.

The P-impedance and S-impedance volumes are divided to give a $V_P/V_S$ volume. As seen in figure 7-15, the $V_P/V_S$ values may aid in discriminating the different oil density values across the Hebron asset in the Ben Nevis reservoir. A $V_P/V_S$ event slice for the Ben Nevis reservoir zone is shown in Figure 7-43.

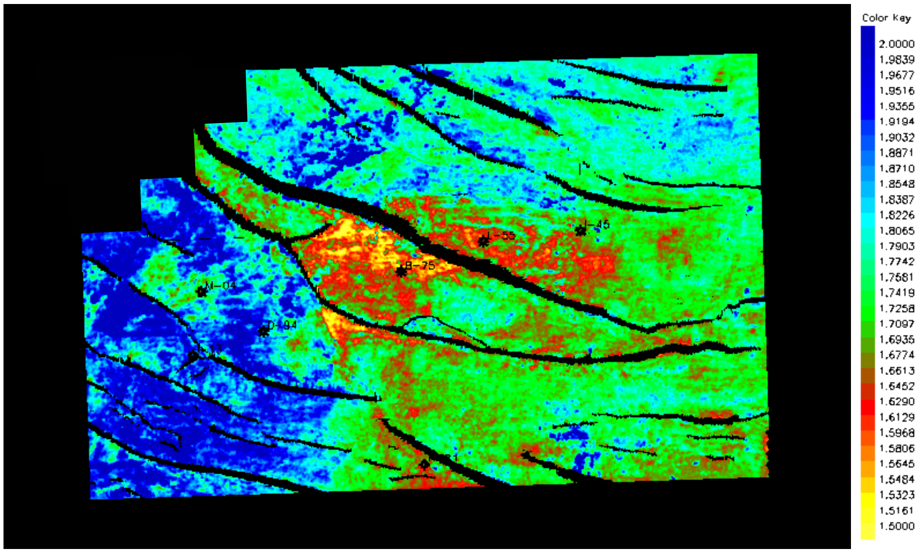


Figure 7-43: $V_P/V_S$ event slice for the Ben Nevis reservoir zone.

This map may show the GOR variations across the asset. The Hebron fault block does not show a distinct anomaly, the oil in this block has a GOR of 50 $m^3/m^3$ and is almost classified as dead oil. The West Ben Nevis block shows a good anomaly in the up-dip portion possibly indicating the presence of a gas cap. The oil in this block has a GOR of 90 $m^3/m^3$ and shows lower $V_P/V_S$ values to that of the Hebron Block. The Ben Nevis block also shows a good anomaly and maybe showing the gas cap as seen in the L55 well. The values are not as low as those in the West Ben Nevis zone but the reservoir quality is degraded in comparison.

### *7.7 NEURAL NETWORK ANALYSIS*

#### *7.7.1 Porosity prediction*

Porosity mapping is an important part of reservoir analysis. With 3D data and good well control neural networks are useful for predicting volumes from log attributes. All seven of the wells on the pre-stack migrated 3D volume are used in the neural network analysis. Figure 7-44 shows the measured porosity log, the seismic trace, and the input attribute data for the B-75 well. In input attributes include: stacked seismic data, intercept, gradient, fluid factor, P-impedance, S-impedance, and density.

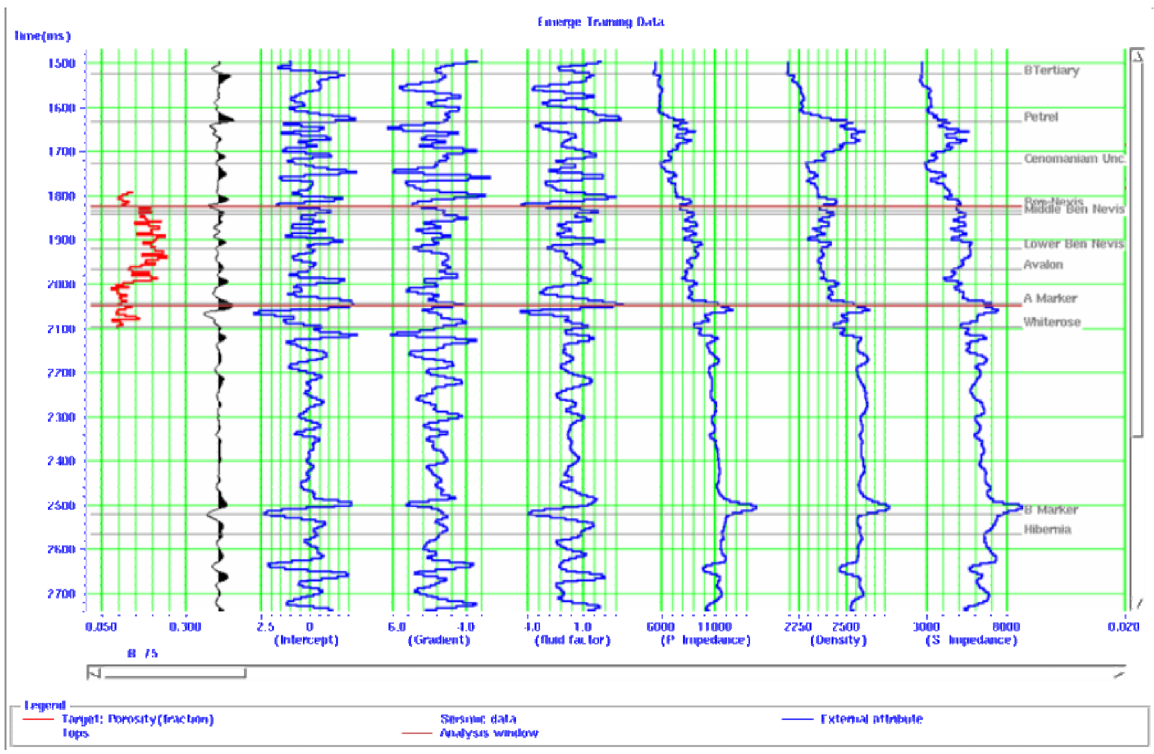

Figure 7-44: Input data at B-75 well

Table 7-2 shows the outcome of the step-wise regression attained using a 5-point convolution operator. It can be seen that the validation error increases between the fourth and fifth attributes indicating that four attributes is most favorable. Table 7-2 can be represented in a graphical representation as shown in figure 7-45. The black line is the training error using all wells in the calculation and the red line represents the validation error. The validation error line at five attributes increases showing that the error slightly increases.

| Attribute | Training error % | Validation error % |
|---|---|---|
| *(Density)$^2$* | *0.037495* | *0.041228* |
| *Quadrature trace (density)* | *0.033420* | *0.037224* |
| *Cosine Instantaneous Phase (S-impedance)* | *0.031216* | *0.036100* |
| *Integrate (Fluid Factor)* | *0.028833* | *0.034559* |
| Quadrature Trace | 0.027333 | 0.034989 |
| 1/(P-impedance) | 0.025923 | 0.032522 |
| Filter 5/10-15/20 | 0.024469 | 0.031858 |
| Instantaneous Frequency (Fluid Factor) | 0.023706 | 0.031628 |
| (Gradient)$^2$ | 0.022986 | 0.031568 |
| Apparent Polarity (Fluid Factor) | 0.022447 | 0.032073 |

Table 7-2: Step-wise regression results.

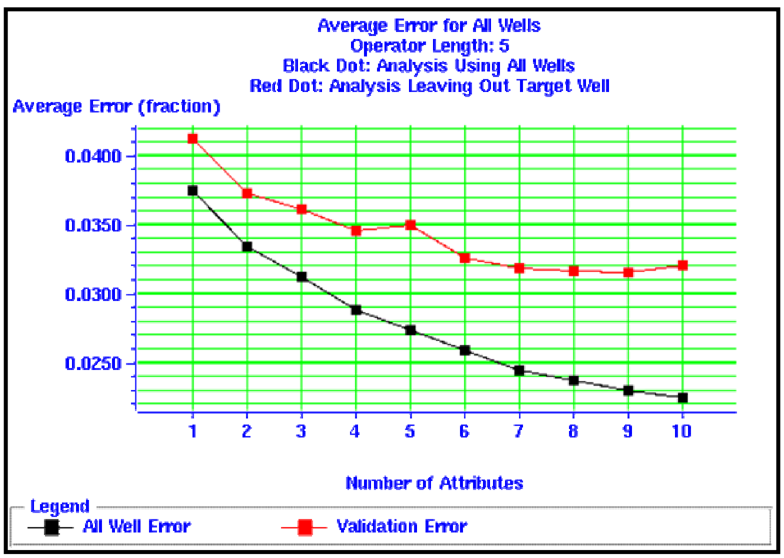


Figure 7-45: Average error as a function of the number of attributes.

The PNN neural network is trained using the same four attributes defined from table 7-2 with a 5-point convolutional operator. The PNN shows good results, with a prediction error of 2.95% and validation error of 3.45%. Figures 7-46 show the measured (in black) and the predicted (in red) porosity logs for all the well locations. The PNN neural network predicted the porosity logs with a correlation of 0.83. Figure 7-47 shows the results from the validation analysis that has a correlation of 0.76.

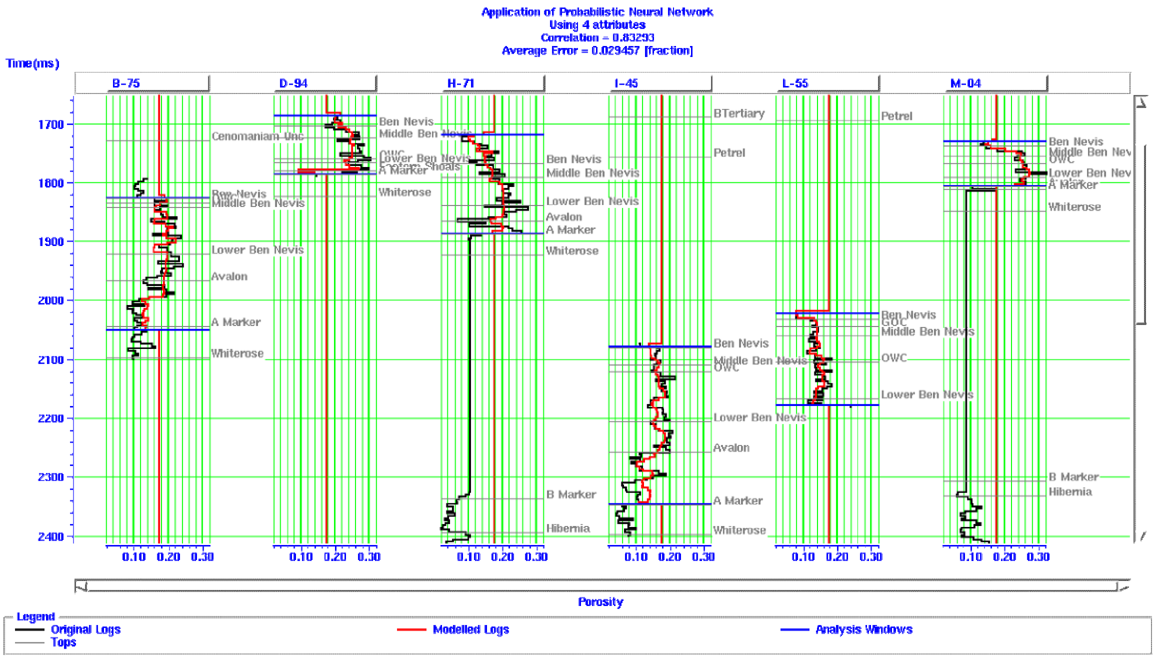


Figure 7-46: Measured porosity logs (in black) and the predicted ones (in red) using PNN neural network.

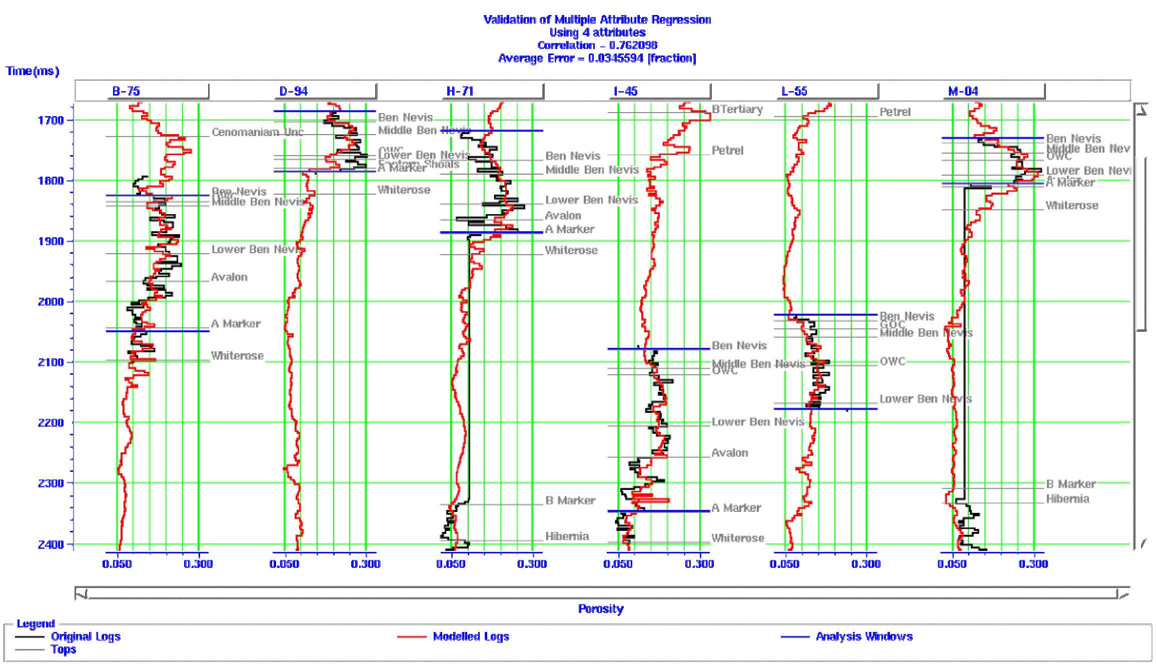


Figure 7-47: Validation of PNN neural network result.

Once the relationship between the porosity logs and the seismic attributes has been determined it is applied to the data to predict the porosity volume. Figure 7-48 shows an arbitrary line through the wells from the predicted porosity volume.

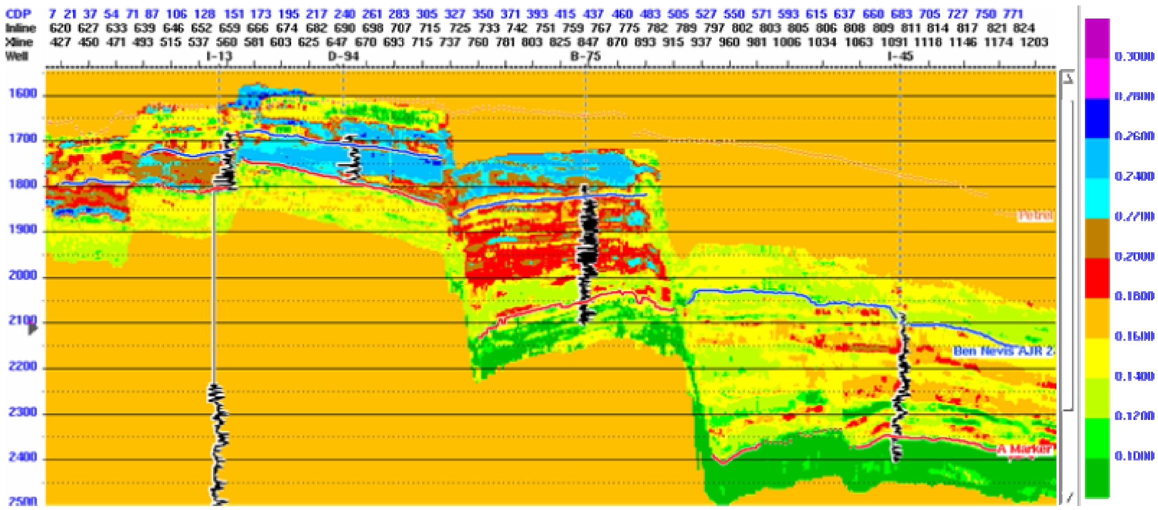


Figure 7-48: Arbitrary line from the predicted porosity volume.

Figure 7-49 is a porosity data slice at the Ben Nevis horizon with a 20 ms window below.

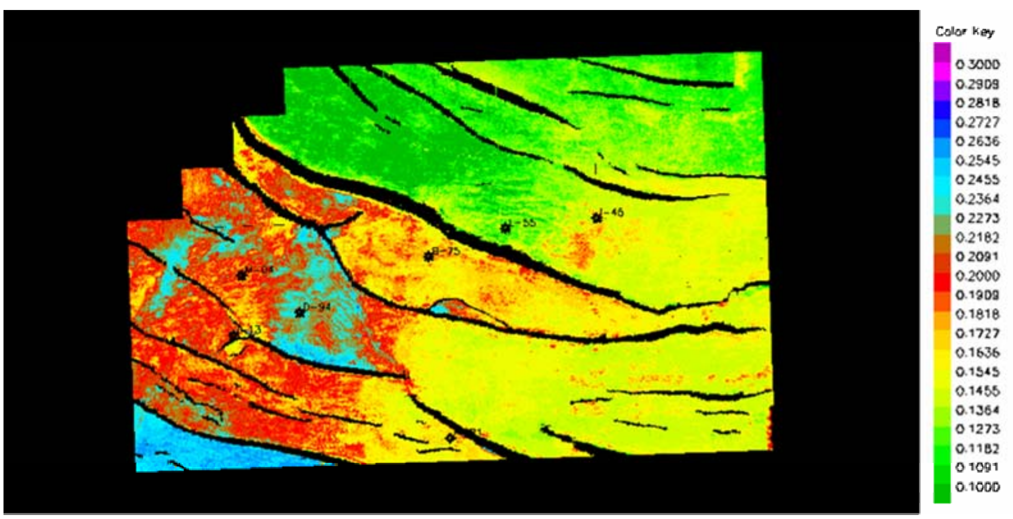


Figure 7-49: Porosity slice at Ben Nevis zone.

The porosity correlates with the well control and as shown in figure 7-10 decreases with depth. The Hebron block shows the best porosity around 20-24%, while the West Ben Nevis block has about 16-18%, and the Ben Nevis block with 12-15%.

### *7.7.1 Fluid density prediction*

Fluid density logs were created at each of the well locations using the water saturation log and known values for the oil and brine densities in each of the Ben Nevis reservoir zones. Again all seven wells were input for the fluid density prediction. The input attributes included: P-impedance, S-impedance, density, $V_P/V_S$, fluid factor, intercept, gradient, and stacked seismic volumes. Table 7-3 shows the outcome of the step-wise regression attained using a 5-point convolution operator.

| Attribute | Training error % | Validation error % |
|---|---|---|
| *Integrate($V_P/V_S$)* | *51.997153* | *54.881422* |
| *Amplitude weighted cosine phase (density)* | *48.675192* | *52.577648* |
| *Dominant frequency (fluid factor)* | *44.998833* | *49.903719* |
| *Integrate (Density)* | *42.631809* | *48.085687* |
| *Derivative instantaneous amplitude (fluid factor)* | *41.549915* | *47.348651* |
| *Instantaneous phase* | *41.114389* | *47.122864* |
| *(fluid factor)$^2$* | *40.500840* | *46.944486* |
| *Filter 45/50-55/60 (porosity)* | *40.183590* | *46.798737* |
| *Filter 45/50-55/60 (density)* | *40.069618* | *46.638812* |
| *Dominant frequency (P-Impedance)* | *40.000525* | *46.587616* |

Table 7-3: Step-wise regression results.

Table 7-3 shows that the validation error decreases to the tenth attribute; so all ten attributes are used. Figure 7-50 shows the graphical representation of table 7.3.

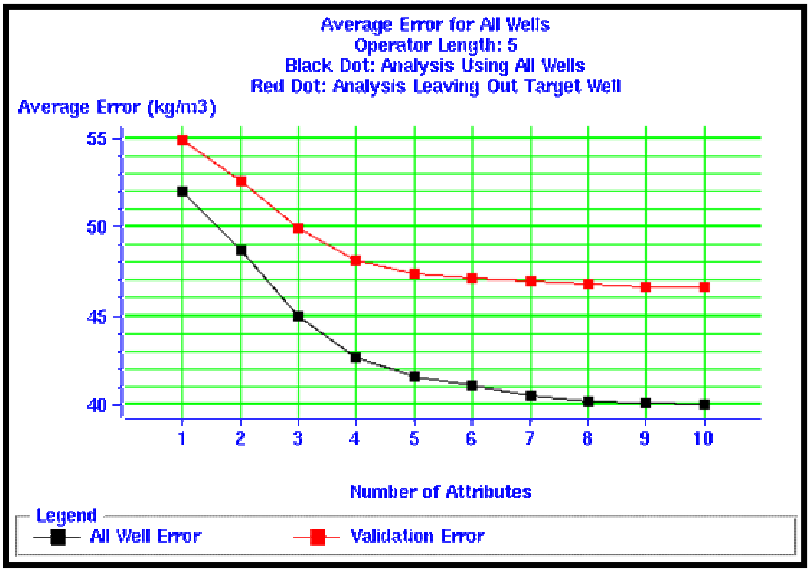


Figure 7-50: Average error as a function of the number of attributes.

The PNN neural network is trained using the attributes defined from table 7-3 with a 5-point convolutional operator. The PNN shows good results, with a prediction error of 26.18 kg/m$^3$ and validation error of 49.98 kg/m$^3$. Figure 7-51 shows the measured (in black) and the predicted (in red) fluid density logs for all the well locations. The PNN neural network predicted the fluid density logs with a correlation of 0.896. Figure 7-52 shows the results from the validation analysis that has a correlation of 0.513.

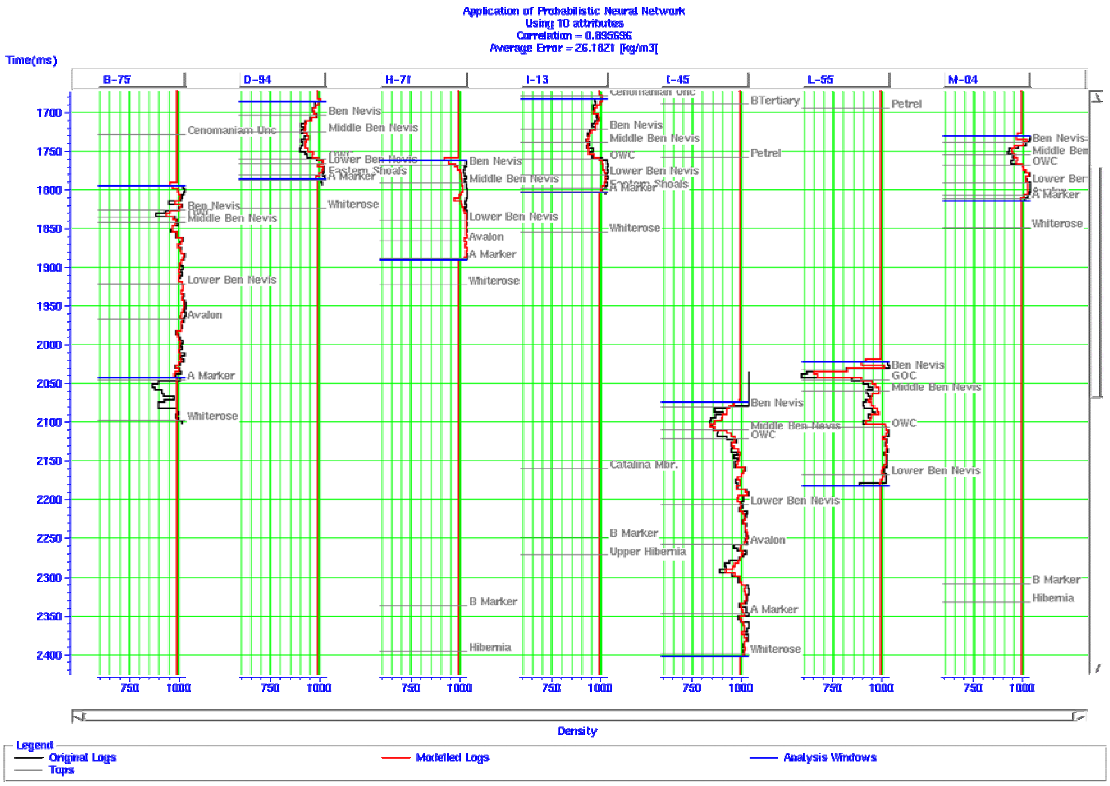


Figure 7-51: Measured fluid density logs (in black) and the predicted ones (in red) using PNN neural network.

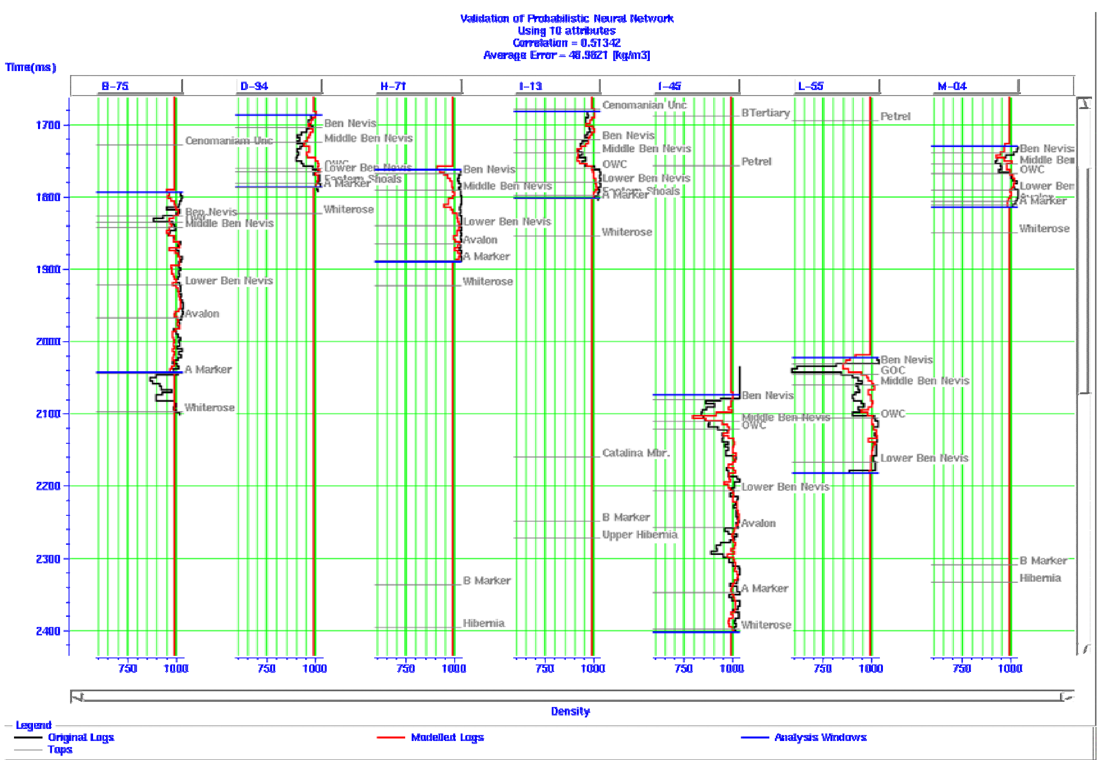


Figure 7-52: Validation of PNN neural network result.

Now that the relationship between the fluid density logs and the seismic attributes has been determined it is applied to the data to predict the fluid density volume. Figure 7-53 shows an arbitrary line through the wells from the predicted fluid density volume.

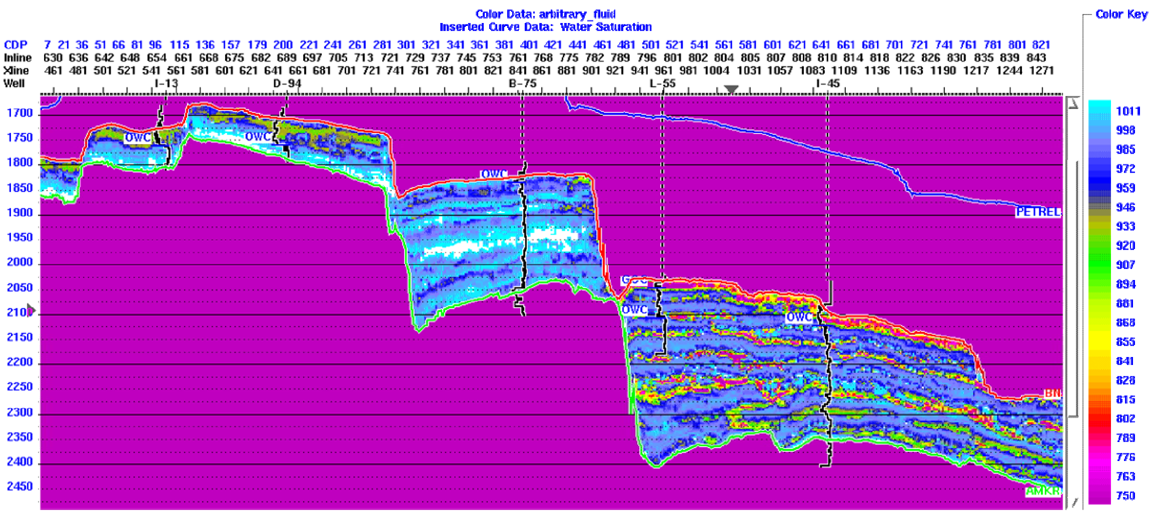


Figure 7-53: Arbitrary line from the predicted fluid density volume.

The fluid density volume shows good correlation with the oil-water-contact in all the wells. In the Hebron block an oil density of approximately 930 kg/m$^3$ can be seen. In the West Ben Nevis block the oil density is around 915 kg/m3 at the B75 well location. These values are dictated by the higher water saturation. The oil density values in the Ben Nevis block are approximately 750 kg/m$^3$, which represent the lower density oil. The water saturation is also high in the Ben Nevis block in comparison with the Hebron block. Figure 7-54 is a fluid density event slice at the Ben Nevis horizon with a 20 ms window below.

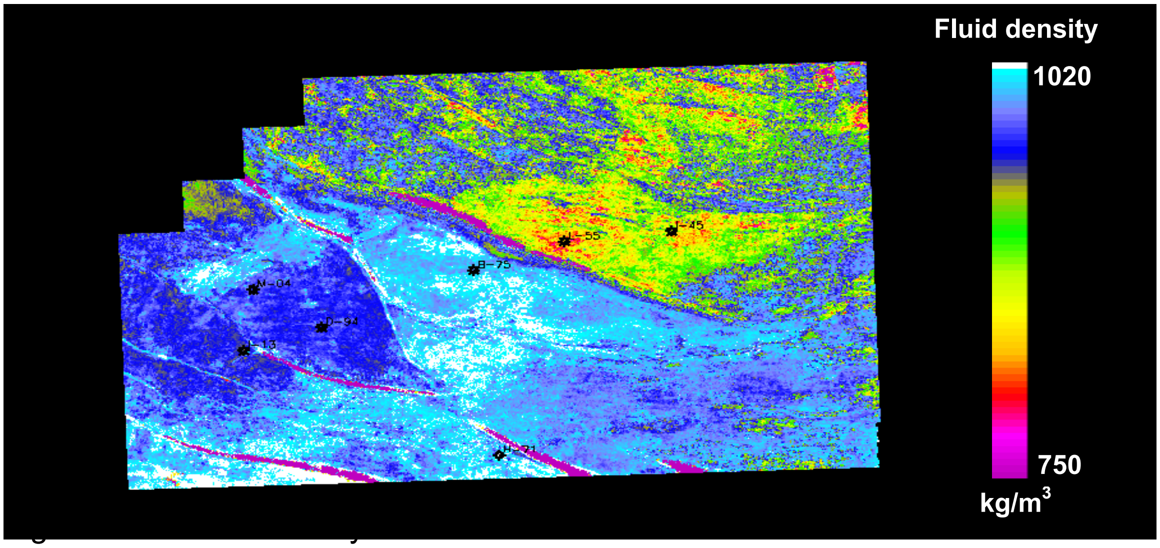


The fluid density values in the Hebron block show good correlation with the oil-water-contact and also may provide insight on the oil contact in the western graben. The West Ben Nevis block does not show anomalous values, this is because the Ben Nevis zone is much thinner than the Hebron block and the water saturation is around 50%. The lower density oil in the Ben Nevis block is quite apparent. The gas cap at the L55 well location maybe represented by the red color on the oil density map.

## 8.0 CONCLUSIONS

### 8.1 Conclusions

In this paper AVO methods were used in an attempt to distinguish oil density variations at the Ben Nevis oil reservoir. The AVO attribute time slices at the top of the Ben Nevis show the variations across to Hebron asset. The crossplots allow isolation and comparison of the AVO responses at the top of the Ben Nevis zone. The inversion volumes showed good insight on the reservoir quality and pore fluid. Neural network results showed good correlation with the well control across the asset.

On the AVO synthetics, the porosity dominated the AVO response dramatically more than the oil density variations. The AVO signature changes from a class II type to class IV type anomaly. The *A*-*B* crossplots shows the strong effect of porosity, the points for the top of the oil sand move from quadrant 4 (class II) to quadrant 2 (class IV). The oil density separation with increasing API is stronger further away from the background trend.

The intercept and gradient analysis isolate the oil-bearing zones associated with the Ben Nevis. The gradient volume also shows variations in these oil-bearing zones possibly indicating the variations in oil density. The intercept versus gradient crossplots show isolated zones for all the well zones except for the I45 well. In comparison, the B75 location separates out compared to the other locations, isolating the light oil regions. The L55 region is not distinguishable from the D94 block wells.

The fluid factor volume highlights the oil-bearing zones across the Ben Nevis zone and may mimic the pool oil-water contact. The B75 block shows the strongest anomalies and also some high values located down dip in the D94 block. The P-reflectivity versus S-reflectivity again isolates all the zones except for the I45 well location. On the comparison plot, the B75 stands out from the other well locations, isolating the lighter oils. The L55 block wells are also not distinguishable compared to the D94 Block wells.

The density reflectivity volume shows anomalies at the Ben Nevis oil zones. The values are strongest at the B75 oil zone in comparison to the D94 and L55 blocks. These variations may be giving information on the varying fluid values across the pool. The L55 block again does not exhibit strong values.

On all the AVO attributes the B75 block, which has an API of ~28, shows the strongest anomalies. Next is the D94 block, which has API values, ranging from 17 to 21. The L55 block has API values of approximately 31 with a gas cap in the L55 well and shows a weaker AVO response in comparison. This is most likely due to the degraded reservoir conditions. This reservoir is also approximately 500 meters deeper than the other zones. The AVO amplitudes in the L55 block are probably showing anomalies for the gas cap since the L55 well location shows an AVO anomaly and the I45 well location does not.

The AVO anomaly down dip in the D94 block is not expected, but can be possible due to a number of factors. For instance, the lithology of the overlying layer may vary laterally creating a laterally changing impedance boundary. There may be a tuning effect down dip causing the AVO effect to increase. Another scenario is that possibly the down dip fault is not sealed, allowing lighter gravity oil to seep into the block, with the denser oil preventing migration to the up dip portions of the fault block.

The simultaneous inversion results correlated closely with the well control over the Hebron asset. The P-impedance volume should give information on the nature of the lithology and pore fluid. The P-impedance inversion result shows that the P-impedance increases with depth. The S-impedance volume gives information on the lithology because S-wave cannot pass through liquids. There is a distinct boundary between the Hebron horst block and the West Ben Nevis block. This may be a depositional boundary; the Ben Nevis sands in the Hebron block have a much greater net-to-gross values than those in the West Ben Nevis and Ben Nevis blocks. The density volume shows insight on the oil-water-contact for the Hebron and West Ben Nevis blocks. This is not so obvious in the Ben Nevis block. The $V_P/V_S$ volume shows anomalies in the West Ben Nevis and Ben Nevis blocks, this can probably be associated with the higher GOR values in these blocks.

The results from the neural network analysis were very encouraging. The predicted porosity volume showed better correlation with the wells than ones done in the past. This is probably because of the attributes used. The predictions done in the past only used the stacked seismic attributes and P-impedance. Whereas, in the analysis AVO attributes, S-impedance, and density were also included. The density proved to be the best input attribute being the first and second ranked attribute in the step-wise regression analysis. The fluid density volume also correlates closely with the well control and oil-water-contact. The Hebron Ben Nevis zone is currently the only Ben Nevis zone that is economic and will be developed. The West Ben Nevis block zone has a much thinner oil column and higher water saturation. In the Ben Nevis block the reservoir quality is too poor for development at this point in time. There are differences across the fluid density map that describes the oil density variations across the asset. The values in the Hebron block are around 930 kg/m$^3$ and describe higher density oil in comparison with the Ben Nevis block where the values are approximately 750 kg/m$^3$.

### 8.2 Future Work

There are a number of investigations that may be considered for future research on the Hebron data set.

Firstly, the processing of the 3D data set may optimized for future AVO work. The data set used for this analysis was not true amplitude processed and therefore may be not optimal for AVO analysis. At the Ben Nevis level there was some residual move-out present especially around M04 well location. Trim statics helped this problem but did not solve it. More angles may have been incorporated into this analysis if an anisotropic or higher order velocity analysis was used.

Next, an investigation into the impedance contrast between the Ben Nevis and the Nautilus shale zones. It is not certain if there is a tuning issue related to the tough denoting the top of the Ben Nevis zone. This maybe more of an issue in the West Ben Nevis block where the Ben Nevis zone is thinner.

There is still uncertainty with the top Ben Nevis horizon pick on certain areas of the 3D volume. This may cause some error in the AVO and inversion analysis. A more detailed look at this pick would be helpful.

Estimation of a matrix density volume would be useful in predicting another version of fluid density. This volume could be used in conjunction with the porosity and density volumes using the Gassmann density equation.

## REFERENCES


Aki, K., and Richards, P. G., 1980, Quantitative seismology: W. H. Freeman and Co.

Allen, J. L. and Peddy C. P., 1993, ‘Amplitude Variation with Offset: Gulf Coast Case Studies’, SEG, Tulsa, Oklahoma.

Batzle, M. and Wang, Z., 1992, Seismic properties of pore fluids: Geophysics, **57**, 1396-1408.

Biot, M. A., 1956a, Theory of propagation of elastic waves in a fluid-saturated porous solid. I. Low-frequency range: J. Acoust. Sot. Am., 28, 168-178.

Biot, M. A., 1956b, Theory of propagation of elastic waves in a fluid-saturated porous solid. II. Higher frequency range: J. Acoust. Sot. Am., 28, 179-191.

Biot, M. A., 1962, Mechanics of deformation and acoustic propagation in porous media: J. Appl. Phys., 33, 1482-1498.

Castagna, J.P., Batzle, M.L. and Eastwood, R.L., 1985, Relationships between compressional-wave and shear-wave velocities in clastic silicate rocks: Geophysics, **50**, 571-581.

Castagna, J.P., and Backus, M.M., Ed., 1993, 'Offset-dependent reflectivity -theory and practice of AVO analysis', SEG publication.

Castagna, John, Swan, Herbert, and Foster, Douglas, 1998, Framework for AVO gradient and intercept interpretation: Geophysics, **63**, 948-956.

Chacko, S, 1989, Porosity identification using amplitude variations with offset: Examples from South Sumatra: Geophysics, **54**, 942-951.

Downton, J. E., and Lines, L., 2001, Constrained three-parameter AVO inversion and uncertainty analysis, CSEG 2001 expanded abstracts.

Driscoll, N. W., and Hogg, J. R., 1995, Stratigraphic response to basin formation: Jeanne d’Arc Basin, offshore Newfoundland. From: Lambiase, J. J. (ed.), 1995, Hydrocarbon Habitat in Rift Basins, Geological Society Special Publication No. 80, pp. 145-163.

Enachescu, M. E., 1987, The tectonic and structural framework of the northeast Newfoundland continental margin. In: Beaumont, C. and Tankard, A.J. (Eds.) Sedimentary Basins and Basin-forming Mechanisms. Canadian Society of Geologists, Memoir 12, 117-146.

Fatti, J.L., Smith, G.C., Vail, P.J., Strauss, P.J., Levitt, P.R., 1994 Detection of gas in sandstone reservoirs using AVO analysis: Geophysics, **59**, 1362-1376

Gardner, G. H. F., Gardner, L. W. and Gregory, A. R., 1974, Formation velocity and density - The diagnostic basics for stratigraphic traps: GEOPHYSICS, **39**, 770-780.

Gassmann, F., 1951, Elastic waves through a packing of spheres: GEOPHYSICS, Soc. of Expl. Geophys., **16,** 673-685. (* Errata in GEO-17-2-0399; Errata in GEO-18-1-0269)

Goodway, B., Chen, T., and Downton, J., 1997, Improved AVO fluid detection and lithology discrimination using Lamé petrophysical parameters: “$\lambda\rho$”, “$\mu\rho$”, and “$\lambda/\mu$ fluid stack”, from *P*- and *S*- inversions: CSEG Recorder, 3-5.

Hampson, D.P., Schuelke, J.S. and Quirein, J.A., 2001, Use of multiattribute transforms to predict log properties from seismic data: GEOPHYSICS, Soc. of Expl. Geophys., **66**, 220-236.

Helgeson, H. C., and Kirkham, D. H., 1974, Theoretical prediction of the thermodynamic behavior of aqueous electrolytes: Am. J. Sci., 274, 1089~1198.

Hilterman, F. J., 1989, Is AVO the seismic signature of rock properties?, 59th Ann. Internat. Mtg: Soc. of Expl. Geophys., 559.

Hilterman, F.J., 1990, Is AVO the seismic signature of lithology? A case history of the Ship Shoal-South addition: The Leading Edge, 9, no. 6, 15-22.

Kelly, M. J., Skidmore, C. and Ford, D., 2001, AVO inversion, Part 1: Isolating rock property contrasts: THE LEADING EDGE, 20, no. 03, 320-323.

Skidmore, C., Kelly, M. and Cotton, R., 2001, AVO inversion, Part 2: Isolating rock property contrasts: THE LEADING EDGE, 20, no. 4, 425-428.

Kuster, G. T. and Toksöz, M. N., 1974, Velocity and attenuation of seismic waves in two-phase media - Part I: Theoretical formulations: GEOPHYSICS, **39**, 587-606.

Kuster, G. T. and Toksöz, M. N., 1974, Velocity and attenuation of seismic waves in two-phase media - Part II: Experimental results: GEOPHYSICS, **39**, 607-618.

Lines, L., 1999, AVO and Density: Canadian Journal of Exploration Geophysics, **35**, no. 1/2, 32-35.

Mavko, G. and Jizba, D., 1991, Estimating grain-scale fluid effects on velocity dispersion in rocks: GEOPHYSICS, **56**, 1940-1949.

O'Connell, R. J., and Budiansky, B., 1974, Seismic velocities in dry and saturated cracked solids: J. Geophys. Res., 79, 5412-5426.

Provais, D. A., 2000, Hebron Asset Appraisal – East Coast of Canada Case History, GeoCanada expanded abstracts.

Ostrander, W.J., 1984, Plane wave reflection coefficients for gas sands at nonnormal angles of incidence: Geophysics, **49**, 1637-1648.

Pendrel, J., 2001, Seismic inversion - The best tool for reservoir characterization: Recorder, 26, no. 1, 16-24.

Pendrel, J., and Dickson, T., 2003, Simultaneous AVO inversion to P-Impedance and $V_P/V_S$, CSEG 2003 annual convention expanded abstracts.

Potter, R. W., II, and Brown, D. L., 1977, The volumetric properties of sodium chloride solutions from 0 to 500 C at pressures up to 2000 bars based on a regression of available data in the literature: U.S. Geol. Surv. Bull 1421-C.

Rees, M., 2001, Integrated fault seal analysis of the Hebron/Ben Nevis and Terra Nova oilfields, Jeanne d'Arc basin, offshore Newfoundland: M.Sc. thesis, Univ. of Calgary, Dept. of Geology and Geophysics.

Rowe, A. M., and Chou, J. C. S., 1970, Pressure-volume-temperature-concentration relation of aqueous NaCl solutions: J. Chem. Eng. Data, 15, 61-66.

Russell, B. H., Lines, L. R., Hirsche, K. W., and Peron, J., 2000, The AVO modelling volume: CREWES Research Report, 12.

Rutherford, S.R., and Williams, R.H., 1989, Amplitude-versus-offset variations in gas sands: Geophysics, 54, 680-688.

Sinclair, I., 1988, Evolution of Mesozoic-Cenozoic sedimentary basins in the Grand Banks area of Newfoundland and comparison with Falvey's (1974) rift model, Bulletin of Canadian petroleum geology, 36, 255-273.

Sheriff, Robert E., 1991, Encyclopedic Dictionary of Exploration Geophysics, SEG.

Shuey, R.T., 1985, A simplification of the Zoeppritz equations: Geophysics, **50**, 609-614.

Smith, T. M., Sondergeld, C. H., and Rai, C. S., 2003, Gassmann fluid substitutions: A tutorial: Geophysics, **68**, 430.

Smith, G. C., and Gidlow, P. M., 1987, Weighted stacking for rock property estimation in gas sands: Geophysical Prospecting, **35**, 993-1014

Smith, G. C. and Sutherland, R. A., 1996, The fluid factor as an AVO indicator: Geophysics, **61,** 1425-1428.

Thomas, L. K., Hankinson, R. W., and Phillips, K. A., 1970, Determination of acoustic velocities for natural gas: J. Petr. Tech., 22, 889-892.

Todorov, T., 2000, Integration of 3C-3D seismic data and well logs for rock property estimation: M.Sc. thesis, Univ. of Calgary, Dept. of Geology and Geophysics.

Wang, Z., 1988, Wave velocities in hydrocarbons and hydrocarbon saturated rocks-with applications to EOR monitoring: Ph.D. thesis, Stanford Univ.

Wang, Z., Nur, A. M. and Batzle, M. L., 1988, Effect of different pore fluids on velocities in rocks, 58th Ann. Internat. Mtg: Soc. of Expl. Geophys., Session:S10.4.

Wang, Z., 2001, Fundamentals of seismic rock physics, Geophysics, **66**, 398.

Wyllie. M. R. J., Gregory, A. R., and Gardner. L. W., 1956, Elastic wave velocities in heterogenious and porous media, Geophysics, **21**, 41-70.

Young, G. B., and Braile, L. W., 1976, A computer program for the application of Zoeppritz's amplitude equations and Knott's energy equations: Bull. Seis. Soc. Amer., **66**, 1881-1885.

Zarembo, V. I., and Fedorov, M. K., 1975, Density of sodium chloride solutions in the temperature range 25-350°C at pressures up to 1000 kg/cm*: J. Appl. Chem. USSR, 48,1949-1953, (English trans).

**Appendix A: *Detailed explanation of Aki and Richards approximation of the Zoeppritz equations***

Aki and Richards (1980) expressed to the Zoeppritz equations in a convenient matrix arrangement. For an interface between two elastic half spaces, there are sixteen reflection and transmission coefficients (Castagna and Backus, 1993). Aki and Richards use a special notation to denote the type of incident wave and the type of derived wave. Figure A-1 explains their notation.

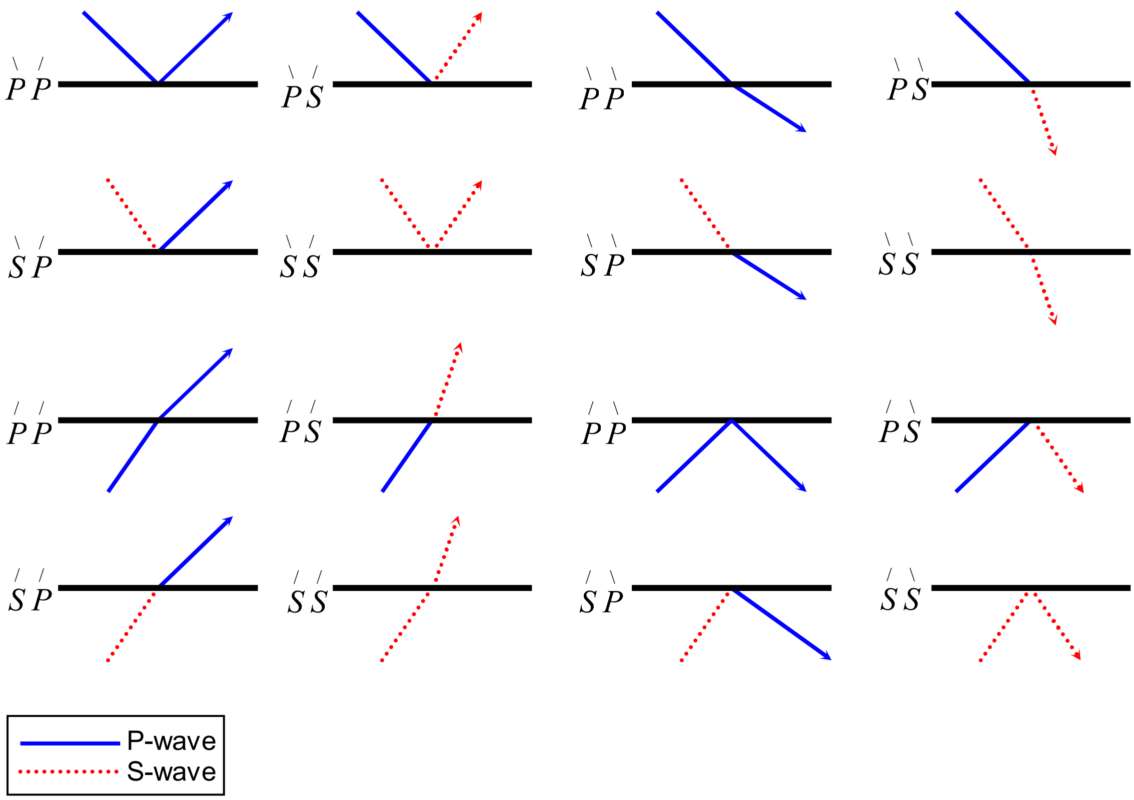


Figure A-1. Notation for the sixteen different possible reflection / transmission coefficients

From this notation the scattering matrix is given by:

$$
Q = \begin{bmatrix}
\overset{\backslash}{P}\overset{/}{P} & \overset{\backslash}{P}\overset{/}{S} & \overset{\backslash}{P}\overset{\backslash}{P} & \overset{\backslash}{P}\overset{\backslash}{S} \\
\overset{\backslash}{S}\overset{/}{P} & \overset{\backslash}{S}\overset{/}{S} & \overset{\backslash}{S}\overset{\backslash}{P} & \overset{\backslash}{S}\overset{\backslash}{S} \\
\overset{/}{P}\overset{/}{P} & \overset{/}{P}\overset{/}{S} & \overset{/}{P}\overset{\backslash}{P} & \overset{/}{P}\overset{\backslash}{S} \\
\overset{/}{S}\overset{/}{P} & \overset{/}{S}\overset{/}{S} & \overset{/}{S}\overset{\backslash}{P} & \overset{/}{S}\overset{\backslash}{S}
\end{bmatrix} = \underset{\sim}{P}^{-1}\,\underset{\sim}{R}
$$

where:

$$
\underset{\sim}{P} = \begin{bmatrix}
-\sin\theta_1 & -\cos\phi_1 & \sin\theta_2 & \cos\phi_2 \\
\cos\theta_1 & -\sin\phi_1 & \cos\theta_2 & -\sin\phi_2 \\
2\rho_1 V_{S1}\sin\phi_1\cos\theta_1 & \rho_1 V_{S1}\left(1-2\sin^2\phi_1\right) & 2\rho_2 V_{S2}\sin\phi_2\cos\theta_2 & \rho_2 V_{S2}\left(1-2\sin^2\phi_2\right) \\
-\rho_1 V_{P1}\left(1-2\sin^2\phi_1\right) & \rho_1 V_{S1}\sin 2\phi_1 & \rho_2 V_{P2}\left(1-2\sin^2\phi_2\right) & -\rho_2 V_{S2}\sin 2\phi_2
\end{bmatrix}
$$

and

$$
\underset{\sim}{R} = \begin{bmatrix}
\sin\theta_1 & \cos\phi_1 & -\sin\theta_2 & -\cos\phi_2 \\
\cos\theta_1 & -\sin\phi_1 & \cos\theta_2 & -\sin\phi_2 \\
2\rho_1 V_{S1}\sin\phi_1\cos\theta_1 & \rho_1 V_{S1}\left(1-2\sin^2\phi_1\right) & 2\rho_2 V_{S2}\sin\phi_2\cos\theta_2 & \rho_2 V_{S2}\left(1-2\sin^2\phi_2\right) \\
\rho_1 V_{P1}\left(1-2\sin^2\phi_1\right) & -\rho_1 V_{S1}\sin 2\phi_1 & -\rho_2 V_{P2}\left(1-2\sin^2\phi_2\right) & \rho_2 V_{S2}\sin 2\phi_2
\end{bmatrix}
$$